Synthesis and Optoelectronic Properties of Azine- and Azinium-Based Functional Dyes (アジンおよびアジニウム系機能性色素の合成と光電子特性)

March, 2019

Toshiaki Enoki

Hiroshima University

Contents

General introduction

Dye chemistry is one of the important research domains that has been developing from the late 19th century. The first artificial dye which names mauveine has been synthesized by Perkin in 1878,[1] and indigo was also synthesized in 1878 by von Baeyer. Stimulated by these sensational discoveries, synthesis and identification of various chromophore and the auxochromic effects were well investigated. On the other hand, the term "functional dye" was originated from Japan in late 1970s (Figure 1). Different from the traditional dyes, functional dyes express new function in response to the external stimuli (light, heat and electronic- and magnetic-field). Therefore, this concept gave innovative interest and activity to dye chemistry, leading to the high technology applications in various fields such as optelectronics,[2] chemosensors,[3] biochemistry[4] etc.

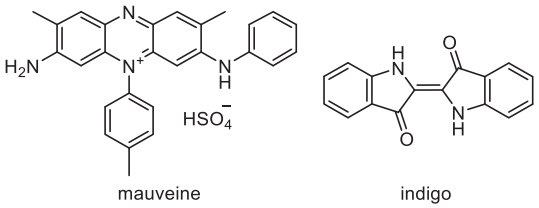

Figure 1. Chemical structures of mauveine and indigo

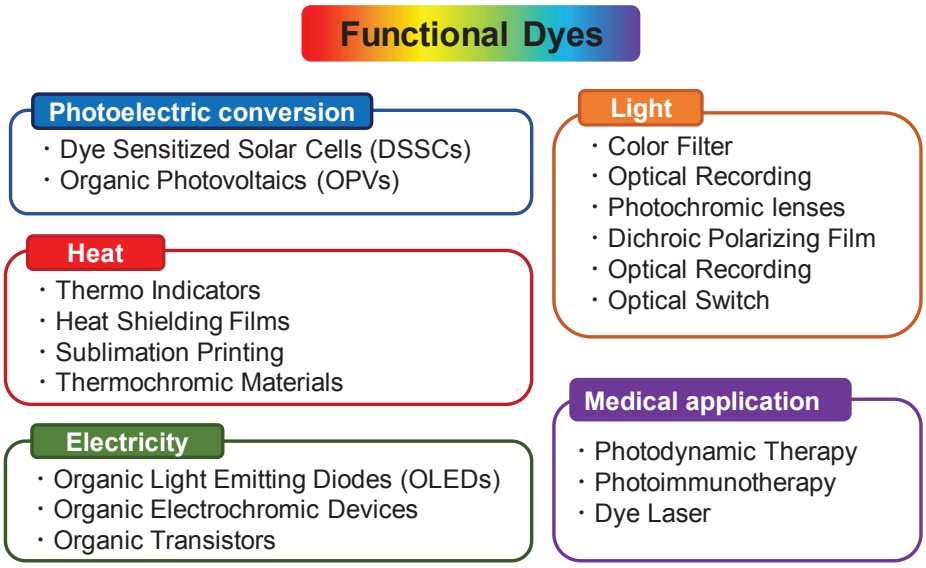

Figure 2. Use of the functional dyes.

In order to apply the dyes to high technology applications described above, it is required to control the photophysical (photoabsorption and fluorescence properties, intersystem crossing (ISC) efficiency), electrochemical (redox potentials and HOMO and LUMO energy level) properties of the dyes. The aromatic rings containing heteroatom are key building blocks for the functional dyes because introducing of heteroatoms on the aromatic hydrocarbons can modify not only the photophysical and electrochemical properties but also the stability of the dyes. Thus, various kinds of heterocyclic systems have been developed.[5] In particular, nitrogen containing aromatic rings such as pyridine, pyrazine and triazine are prominent and important heterocycles. They are often used as an electron-withdrawing component in donor-π-acceptor (D-π-A) dyes due to their relatively strong electron-withdrawing ability (Figure 2a).[6] In addition, nitrogen atoms on the pyridine and pyrazine ring possess strong basicity so that they can form strong interaction with Bronsted- and Lewis- acids and metal ions. Thus, pyridine and pyrazine derivatives have been utilized as not only the optical sensors for acids and metal ions[7] but also the ligands for the metal complexes[8] and anchoring unit of the photosensitizers for dye sensitized solar cells (DSSCs) (Figure 2b).[9]

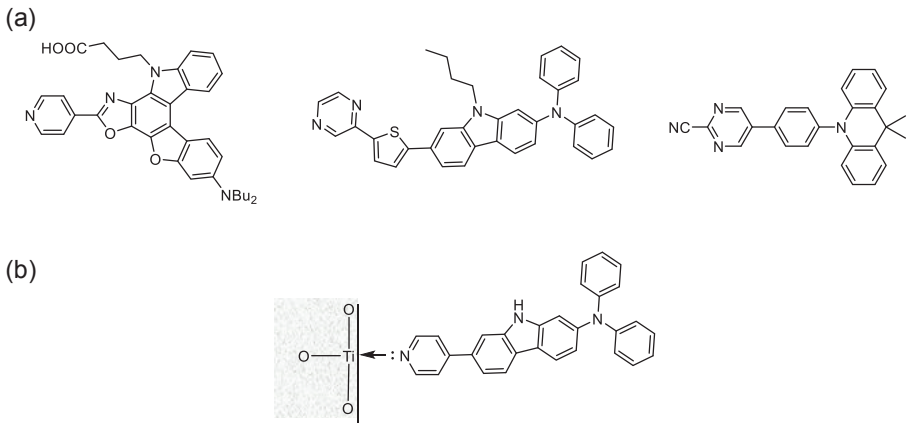

Figure 3. (a) Chemical structures of azine-based D-π-A dyes. (b) Adsorption mechanisms of pyridine-based photosensitizers on TiO_2 surface.

Nitrogen-containing fused aromatic systems such as phenazines, quinoxalines, phenanthrolines and *β*-carbolines are also interesting π-building block for the functional dyes. These compounds were applied in organic field effect transistors (OFETs), analytical reagents as well as the fluorescence probes because they show high carrier mobility and good fluorescence properties originating from their rigid structures and high planarity (Figure 4a, 4b).[10-12] Among them, *β*-carboline is one of the important heterocyclic scaffold for medicinal and biological applications due to its various biological and pharmacological activities (Figure 4c).[13] In addition, *β*-carboline can form strong intermolecular interaction with hydrogen-bond donating species such as Brønsted acids, alcohols and water. Thus, the photophysical properties of *β*-carboline derivatives in the presence of hydrogen-bond donating species have been studied (Figure 4d).[14]

On the other hand, the azine dyes can be converted into the azinium dyes by treating with alkyl halide or cyclic sulfonate, and some of the D-π-A pyridinium dyes have received considerable attention in fundamental study due to their specific solvatochromic properties (i.e. negative solvatochromisms and specific bathochromic shifts in halogenated solvent).[15] Moreover, azinium dyes generally shows strong electron-withdrawing characteristics leading to the good electrophilicity over the neighboring unit,so that the azinium dyes are used as sensing materials for anions (Figure 5).[16]

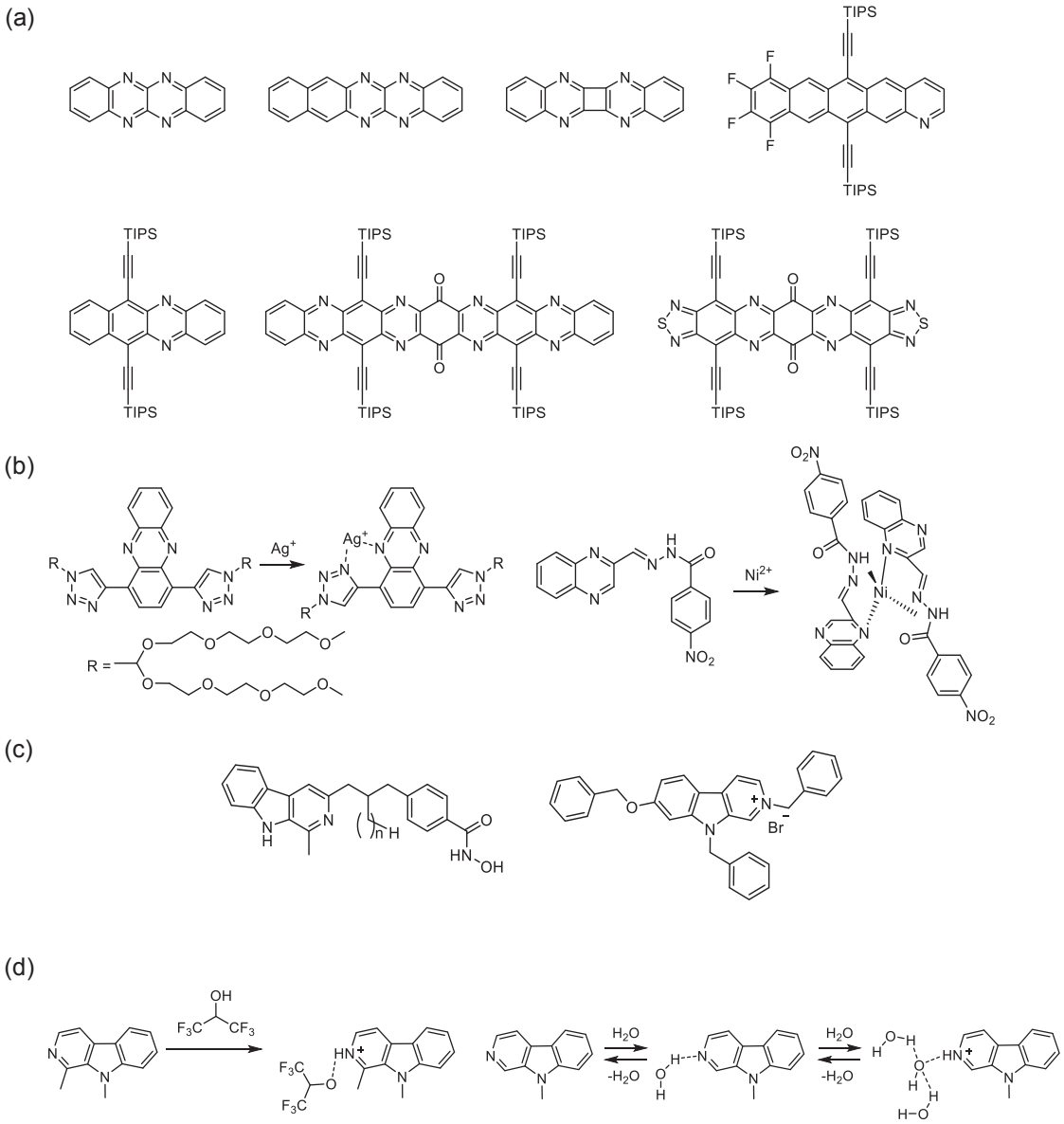

Figure 4. (a) Chemical structures of N-heteroacenes. (b) Azine-based optical sensors for metal ions. (c) Antiproliferative agent based on the *β*-carboline skeleton. (d) Optical sensors of *β*-carboline derivatives for hydrogen-donating species.

As described above, azine and azinium dyes have been energetically studied in various research fields. However, there is still room for further investigation into the azine and azinium dye chemistry. In this thesis, the author reports the preparation and photophysical and electrochemical properties of new azine and azinium dyes, and some specific

photopysical properties of the dyes including singlet oxygen generation and water sensing ability were investigated.

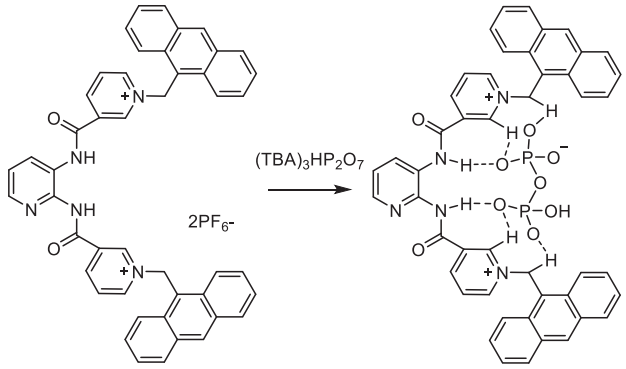

Figure 5. Azine-based colorimetric sensor for hydrogen pyrophosphate

In Chapter 1, the structural isomers of D-π-A-π-D pyrazine dyes **2,5-PD** and **2,6-PD** which are substituted with two diphenylamine-thienylcarbazole moieties (electron-donating and π-conjugated unit) on 2,5- and 2,6-position of a pyrazine ring (electron-withdrawing unit) have been developed (Figure 6). It was found that the structural isomers **2,5-PD** and **2,6-PD** show a significant solvatofluorochromism, and the photophysical and electrochemical measurements, and density functional theory calculations reveals that 2,5-substituted pyrazine dye **2,5-PD** possesses stronger photoabsorption and fluorescence properties in longer wavelength region and lower LUMO energy level, compared to the 2,6-substituted structural isomer **2,6-PD**.

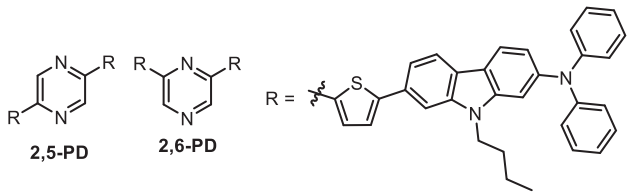

Figure 6. Chemical structures of **2,5-PD** and **2,6-PD**.

In Chapter 2, the D-π-A-π-D pyrazinium dyes **PD-Br** and **PD-I** bearing different counter anion (X^- = Br^- and I^- for **PD-Br** and **PD-I**, respectively) have been developed as the photosensitisers possessing the ability for singlet oxygen ($^1O_2$) generation

(Figure 7). The effect of the counter anion on the efficiency for $^1O_2$ generation such as quantum yields ($\Phi_\triangle$) and late constant (k_s) have been investigated in various solvents. It was found that two pyrazinium dyes pyrazinium dyes possess the ability to generate $^1O_2$ under visible light irradiation, and the $\Phi_\triangle$ values of **PD-I** bearing I^- anion is higher than that of **PD-Br** bearing Br^- due to the effective intersystem crossing (ISC) from the singlet excited state of the photosensitizer ($^1S^*$) to the triplet excited state ($^3S^*$) by the greater heavy-atom effect of I^- ion as the counter anion. Moreover, it was found that THF and dichloromethane are favorable solvents for the D-π-A-π-D pyrazinium dyes to generate $^1O_2$ compared with the polar solvents such as acetonitrile and DMSO. On the basis of the estimation of the $\Phi_\triangle$ and k_s, the HOMO and LUMO energy levels of **PD-Br** and **PD-I**, and density functional theory (DFT) calculation, the photoabsorption and $^1O_2$ generation properties of the D-π-A pyrazinium dyes are discussed.

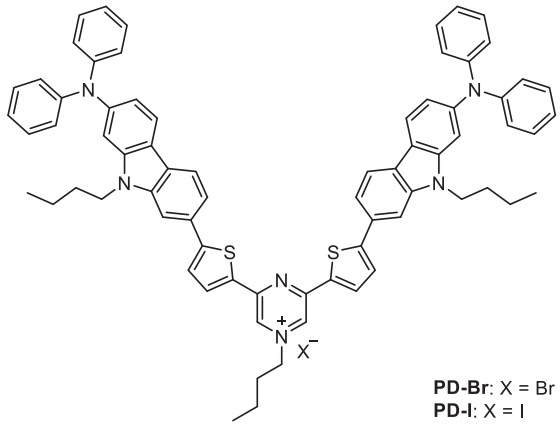

Figure 7. Chemical structures of **PD-Br** and **PD-I**

In Chapter 3, the author has evaluated the ability for $^1O_2$ generation of the pyridine-substituted porphyrin dimer (**CPD**) linked by butadiyne and its inclusion comlex (**C_{60}⊂CPD**) with C_{60} (Figure 8). The photoabsorption spectral measurements and ESR spectral measurements demonstrated that **CPD** and **C_{60}⊂CPD** possess the ability for $^1O_2$ generation under visible light irradiation. Additionally, it was found that the $\Phi_\triangle$ value of

CPD is higher than that of **C$_{60}$⊂CPD**. The difference in $\Phi_{\triangle}$ value between the two compounds have been discussed based on the kinetic and thermodynamic consideration concerning the electron transfer processes between the porphyrin dimer and C_{60}.

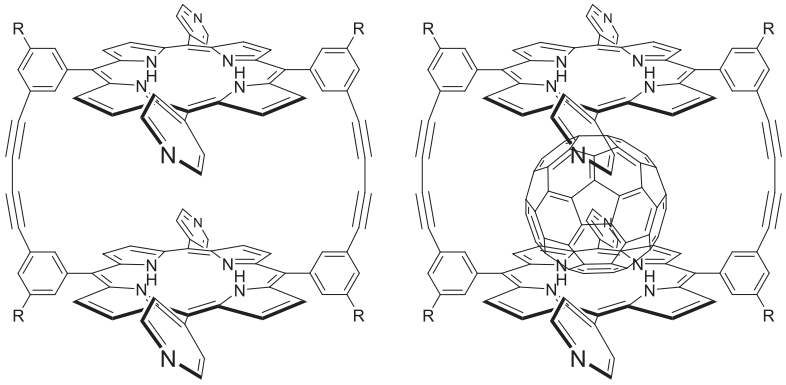

Figure 8. Chemical structures of **CPD** and **C$_{60}$⊂CPD**

In chapter 4, the julolidine-structured pyrido[3,4-*b*]indole dye **ET-1** has been newly designed and developed as a small D-A fluorescent dye (Figure 9). **ET-1** showed bathochromic shifts of the fluorescence band upon changing from aprotic solvents to protic solvents, as well as positive fluorescence solvatochromism. Moreover, it was found that **ET-1** can form a 1 : 1 Py(N)-B complex with boron trifluoride and a hydrogen-bonded proton transfer (Py(N)-H) complex with trifluoroacetic acid, which exhibit photoabsorption and fluorescence bands at a longer wavelength region than the pristine **ET-1**. Based on optical (photoabsorption and fluorescence spectroscopy) and electrochemical (cyclic voltammetry) measurements, Lippert-Mataga plots, ^{1}H NMR spectral measurement and density functional theory (DFT) calculation, this work indicated that the Py(N)-B complex or the Py(N)–H complex is effectively formed in solution. This is due to the strong pyridine-boron or pyridine–H^{+} interaction, which can

be attributed to the enhanced basicity or the accumulated electron density on the nitrogen atom of the pyridine ring caused by the introduction of a julolidine moiety as a strong electron-donating group. This fact suggests that D-A-type dye **ET-1** based on the julolidine-structured *β*-carboline possesses the ability to act as a colorimetric and fluorescent sensor for Brønsted and Lewis acids.

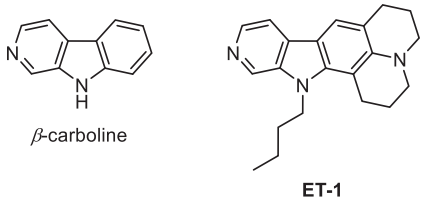

Figure 9. Chemical structures of *β*-carboline and **ET-1**

In Chapter 5, the *β*-carboline-boron trifluoride complexes **9-MP** and **ET-1-BF_3** were developed. The optical sensing ability of the two complexes for water was estimated. It was found that **9-MP-BF_3** and **ET-1-BF_3** can detect water by changing its photoabsorption and fluorescence properties based on change in the intramolecular charge transfer (ICT) characteristics through the dissociation of the complex into the corresponding *β*-carboline dyes (**9-MP** and **ET-1**) by water molecule, formation of the hydrogen-bonded complex (**9-MP-H_2O** and **ET-1-H_2O**) and formation of the hydrogen-bonded proton transfer complex (**9-MP-H+** and **ET-1-H+**) in low, moderate and high water content region, respectively. Thus, ICT-type sensors based on pyridine-boron trifluoride complex are promising candidates for colorimetric and fluorescence sensor for water in solution (Figure 10).

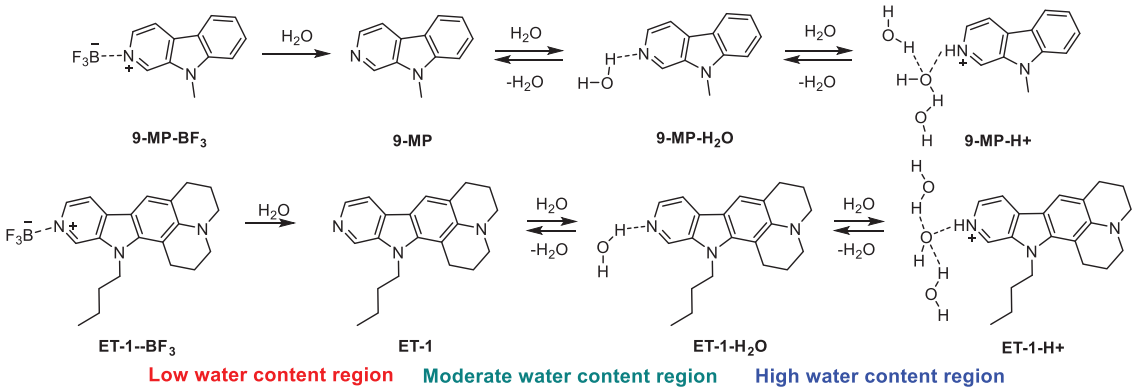

Figure 10. Sensing mechanisms of **9-MP-BF3** and **ET-1-BF3** for the detection of water in solvents.

Reference

1. (*a*) W. H. Perkin, *J. Chem. Soc., Trans.*, **1879**, *35*, 717–732; (*b*) O. Meth-Cohn. and M. Smith, *J. Chem. Soc., Perkin Trans.* **1994,** *1*, 5.

2. (*a*) A. M. Breul, M. D. Hager and U. S. Schubert, *Chem. Soc. Rev.*, **2013**, *42*, 5366; (*b*) X. -C. Li, C. -Y. Wang, W. -Y. Lai and W. Huang, *J. Mater. Chem. C*, **2016**, *4*, 10574; (*c*) A. Mahmood, J. -Y. Hu, B. Xiao, A. Tang, X. Wang and E. Zhou, *J. Mater. Chem. A*, **2018**, *6*, 16769.

3. (*a*) A. Wild, A. Winter, F. Schlütter and U. S. Schubert, *Chem. Soc. Rev.*, **2011**, *40*, 1459; (*b*) S. Ishihara, J. Labuta, W. V. Rossom, D. Ishikawa, K. Minam, J. P. Hill and K. Ariga, *Phys. Chem. Chem. Phys.*, **2014**, *16*, 9713; (*c*) G. Fang, H. Wang, Z. Bian, J. Sun, A. Liu, H. Fang, B. Liu, Q. Yao and Zhongyu Wu, *RSC Adv.*, **2018**, *8*, 29400; (*d*) M. Saleem, M. Rafiq, M. Hanif, M. A. Shaheen and S. -Y. Seo, *J. Fluoresc.* **2018**, *28*, 97.

4. (*a*) M. Schäferling, *Angew. Chem. Int. Ed*. **2012**, *51*, 3532; (*b*) L. Levi and T. J. J. Müller, *Chem. Soc. Rev.*, **2016**, *45*, 2825; (*c*) D. Wu, A. C. Sedgwick, T. Gunnlaugsson, E. U. Akkaya, J. Yoon and T. D. James, *Chem. Soc. Rev.*, **2017**, *46*, 7105; (*d*) D. Wu, A. C. Sedgwick, T. Gunnlaugsson, E. U. Akkaya, J. Yoon and T. D. James, *Chem. Soc. Rev.*, **2017**, *46*, 7105.

5. (*a*) W. Delaunay,a R. Szűcs, S. Pascal, A. Mocanu, P.-A. Bouit, L. Nyulászi and M. Hissler, *Dalton Trans*., **2016**, *45*, 1896; (*b*) Marcin Stępień, Elżbieta Gońka, Marika Żyła, and Natasza Sprutta, *Chem. Rev*. **2017**, *117*, 3479; (*c*) M. Stolar and T. Baumgartner, *Chem. Commun.*, **2018**, *54*, 3311.

6. (*a*) A. Abbotto, L. Beverina, R. Bozio, A. Facchett, C. Ferrante, G. A. Pagan, D. Pedron and R. Signorini, *Org. Lett.*, **2002**, *4*, 1495; (*b*) Filip Bureš, *RSC Adv.*, **2014**, *4*, 58826; (*c*) Z. -B. Cai, H. -M. Shen, M. Zhou, S. -L. Li and Y. -P. Tian, *RSC Adv.*, **2016**, *6*, 46853.

7. (*a*) J. Yuasa and S. Fukuzumi, *J. Am. Chem. Soc.*, **2006**, *128*, 15976; (*b*) M. C. Aragoni, M. Arca, A. Bencini, A. J. Blake, C. Caltagirone, G. D. Filippo, F. A. Devillanova, A. Garau, T. Gelbrich, M. B. Hursthouse, F. Isaia, V. Lippolis, M. Mameli, P. Mariani, B. Valtancoli and C. Wilson, *Inorg. Chem*., **2007**, *46*, 4548; (*c*) X. J. Feng, P. Z. Tian, Z. Xu, S. F. Chen and M. S. Wong, *J. Org. Chem*. **2013**, *78*, 11318; (*d*) K. P. Carter, A. M. Young and Amy E. Palmer, *Chem. Rev*. **2014**, *114*, 4564; (*e*) A. J. Beneto, V. Thiagarajan and A. Siva, *RSC Adv.*, **2015**, *5*, 67849.

8. (*a*) Y. -Z. Hu, C. Chamchoumis, J. S. Grebowicz and R. P. Thummel, *Inorg. Chem.*, **2002**, *41*, 2296; (*b*) K. R. Grüunwald, M. Volpe, P. Cias, G. Gescheidt and N. C. Müosch-Zanetti, *Inorg. Chem.*, **2011**, *50*, 7478; (*c*) K. S. Bejoymohandas, A. Kumar, S. Varughese,a E. Varathan, V. Subramaniand and M. L. P. Reddy, *J. Mater. Chem. C*, **2015**, *3*, 7405; (*d*) K. T. Chan, G. S. M. Tong, W. -P. To, C. Yang, L. Du, D. L. Phillips and C. -M. Che, *Chem. Sci.*, **2017**, *8*, 2352.

9. (*a*) Y. Ooyama, S. Inoue, R. Asada, G. Ito, Kohei, K. Kenji, Komaguchi Ichiro Imae Yutaka Harima *Eur. J. Org. Chem*.**2010**, 92; (*b*) Y. Ooyama, S. Inoue, T. Nagano, K. Kushimoto, J. Ohshita, I. Imae, K. Komaguchi, and Y. Harima, *Angew. Chem. Int. Ed.* **2011**, *50*, 7429; (*c*) D. Daphnomili, G. Landrou, S. P. Singh, A. Thomas, K. Yesudas, Bhanuprakash K., G. D. Sharma and A. G. Coutsolelo, *RSC Adv*., **2012**, *2*, 12899; (*d*) N. Shibayama, H. Ozawa, M. Abe, Y. Ooyama, and H. Arakawa, *Chem*. *Commun*., **2014**, *50*, 6398; (*e*) C. -L. Mai, T. Moehl, C. -H. Hsieh, J. -D. Décoppet, S. M. Zakeeruddin, M. Grätzel, and C. -Y. Yeh, *ACS Appl. Mater. Interfaces*, **2015**, *7*, 14975.

10. (*a*) J. Nishida, Naraso, S. Murai, E. Fujiwara, H. Tada, M. Tomura and Y. Yamashita, *Org. Lett.*, **2004**, *6*, 2007; (*b*) U. H. F. Bunz, J. U. Engelhart, B. D. Lindner and M. Schaffroth, *Angew. Chem. Int. Ed*. **2013**, *52*, 3810; (*c*) Q. Miao, *Adv. Mater.* **2014**, *26*,

5541; (*d*) S. Yang, B. Shan, X. Xu and Q. Miao, *Chem. Eur. J.* **2016**, *22*, 6637.

11. (*a*) N. J. Singh, E. J. Jun, K. Chellappan, D. Thangadurai, R. P. Chandran, I. -C. Hwang, J. Yoon and K. S. Kim, *Org. Lett.*, **2007**, *9*, 485; (*b*) J. J. Bryant, Y. Zhang, B. D. Lindner, E. A. Davey, A. L. Appleton, X. Qian and U. H. F. Bunz, *J. Org. Chem*. **2012**, *77*, 7479; (*c*) S. Goswami, S. Chakraborty, S. Paul, S. Halder and A. C. Maity, *Tetrahedron Lett*., **2013**, *54*, 5075.

12. (*a*) D. J. Hurley, S. E. Seaman, J. C. Mazura and Y. Tor, *Org. Lett.*, **2002**, *4*, 2305; (*b*) N. Sharma, S. I. Reja, N. Gupta, V. Bhalla, D. Kaur, S. Arorab and M. Kumar, *Org. Biomol. Chem*., **2017**, *15*, 1006-1012; (*c*) G. Balamurugan, S. Velmathi, N. Thirumalaivasan and S. P. Wu, *Analyst*, **2017**, *142*, 4721.

13. (*a*) T. Kawasaki and K. Higuchi, *Nat. Prod. Rep*., **2005**, *22*, 761; (*b*) T. A. Mansoor, C. Ramalhete, J. Molna´r, S. Mulhovo and M. J. U. Ferreira, *J. Nat. Prod*., **2009**, *72*, 1147.

14. (*a*) T. J. Hagen, P. Skolnick and J. M. Cook, *J. Med. Chem*., **1978**, *30*, 750; (*b*) X. Yu, W. Lin, R. Pang and Ming Yang, *Eur. J. Med. Chem*., **2005**, *40*, 831; (*c*) I. X. Garcia-Zubiri, H. D. Burrows, J. S. Seixas de Melo, J. Pina, M. Monte-serin and M. J. Tapia, *Photochem. Photobiol*. **2007**, *83*, 1455; (*d*) R. Ikeda, T. Kimura, T. Tsutsumi, S. Tamura, N. Sakai and T. Konakahara, *Bioorg. Med. Chem. Lett.*, **2012**, *22*, 3506.

15. (*a*) A. Botrel and A. L. Beuze, *J. Chem. SOC., Faraday Trans. 2,* **1984**, *80*, 1235; (*b*) Z. -S. Wang, F. -Y. Li, C. -H. Huang, L. Wang, M. Wei, L. -P. Jin and N. -Q. Li, *J. Phys. Chem. B*, **2000**, *104*, 9676; (*c*) Y. Ooyama, R. Asada, S. Inoue, K. Komaguchi, I. Imae and Y. Harima, *New J. Chem*., **2009**, *33*, 2311; (*d*) M. Cheng, X. Yang, J. Li, C. Chen, J. Zhao, Y. Wang and Licheng Sun, *Chem. Eur. J.* **2012**, *18*, 16196; (*e*) Y. Ooyama, Y. Oda, T. Mizumo, Y. Harima and J. Ohshita, *Eur. J. Org. Chem*. **2013**, 4533.

16. (*a*) K. Ghosh, G. Masanta and A. P. Chattopadhyay, *Eur. J. Org. Chem*. **2009**, 4515;

(*b*) K. Ghosh, A. R. Sarkar, A. Samadder and A. R. Khuda-Bukhsh, *Org. Lett*., **2012**, *14*, 4314; (*c*) K. Ghosh, A. R. Sarkar, A. Ghorai, U. Ghosh, *New J. Chem*. **2012**, *36*, 1231.

Chapter 1

Synthesis and photophysical and electrochemical properties of structural isomers of pyrazine-based D-π-A-π-D fluorescent dyes

Introduction

As described in general introduction, the functional dyes are used in various high-technology application including organic light emitting diodes (OLEDs), dye sensitized solar cells (DSSCs) and biological imaging. In particular, D-π-A dyes have attracted much attention because the D-π-A dyes show strong photoabsorption and emission properties based on intramolecular charge transfer (ICT) excitation from the electron-donating unit to the electron-withdrawing unit.[1-3] In order to apply the D-π-A dyes to such optoelectronic devices, much effort has been devoted to improve their photophysical and electrochemical properties by modulating donor and acceptor moiety as well as π-conjugated systems.[4]

The fluorescence properties of the D-π-A dyes are dependent on the environmental polarity. When the dipole moment of the dye in the excited state (μ_e) is larger than that in the ground state (μ_g), red-shift of fluorescence band with an increase in solvent polarity (positive solvatofluorochromism) is normally observed ($\mu_g < \mu_e$). On the other hand, when the dipole moment of the dye decreased upon photoexcitation, blue-shift of fluorescence band with an increase in solvent polarity (negative solvatofluorochromism) generally occurs ($\mu_g > \mu_e$). Thus, solvatofluorochromic materials are widely used as a polarity sensor[5] and polarity-sensitive fluorescence probes[6] because they can detect polarity change by changing the fluorescence wavelength and intensity. The fluorescence solvatochromic

property is affected not only by the electron-donating and electron-withdrawing abilities of the substituents but also the position of the substituents on the fluorophore. Niko et al. have reported the asymmetric-substituted pyrene dyes, and they demonstrated that the solvatochromic behavior of these pyrene dyes are dependent on the position of the electron-donating and electron-withdrawing substituents on a pyrene skeleton.[7]

As described in General Introduction, azine rings such as pyridine, pyrazine and triazine ring can work as an electron-withdrawing unit in the D-π-A system.[8] In the previous work, a series of D-π-A dyes with azine rings as an electron-withdrawing and anchoring unit have been developed for the photosensitizer for DSSCs.[9] It was found that the D-π-A pyrazine dye **2,6-PD** bearing two electron-donating and π-conjugated units on the 2,6-position of a pyrazine ring possesses intense photoabsorption and moderate fluorescence properties in visible light region.[10] In this chapter, in order to gain insight into the influence of the position of the D-π unit on the photophysical properties, electrochemical properties and HOMO and LUMO energy level of pyrazine-based D-π-A dye, the author have newly synthesized pyrazine-based fluorescent D-π-A-π-D dye **2,5-PD** which is substituted with two diphenylamine-thienylcarbazole moieties on 2,5-position of a pyrazine ring. Since **2,5-PD** has two D-π components at 2- and 5-positions on a pyrazine ring as the electron-withdrawing group, it is expected that **2,5-PD** possesses strong photoabsorption and emission properties originating from the ICT excitation. Based on the photoabsorption and fluorescence spectroscopy, cyclic voltammetry (CV) and density functional theory (DFT) calculations, it was found that **2,5-PD** possesses intense photoabsorption and fluorescence properties and low LUMO energy level, compared to the 2,6-substituted structural isomer **2,6-PD (**Figure 1).

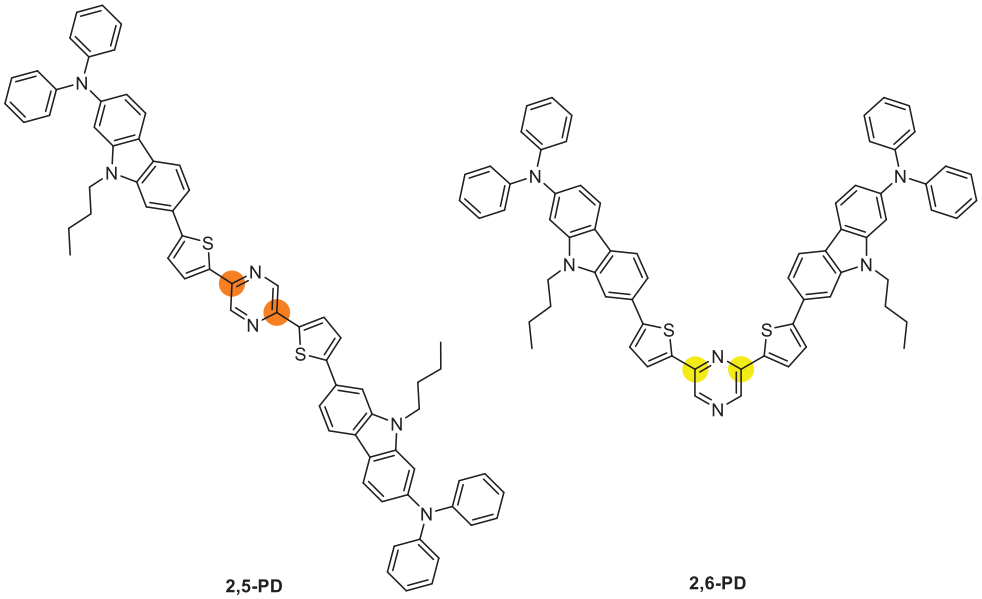

Figure 1. Chemical structures of **2,5-PD** and **2,6-PD**

Experimental

General

Melting points were measured using a Yanaco micro melting point apparatus MP model. IR spectra were recorded on a SHIMADZU IRAffinity-1 spectrometer using the ATR method. High-resolution mass spectral data were acquired using a Thermo Fisher Scientific LTQ Orbitrap XL. ^{1}H NMR and 13C NMR spectra were recorded using a Varian-400 (400 MHz) FT NMR spectrometer. Absorption spectra were recorded using a Shimadzu UV-3150 spectrophotometer and fluorescence spectra were recorded using a HORIBA FluoroMax-4 spectrofluorometer. The fluorescence quantum yields in solution were determined using a HORIBA FluoroMax-4 spectrofluorometer with a calibrated integrating sphere system. Fluorescence decay measurements were performed on a HORIBA DeltaFlex modular fluorescence lifetime system, using a Nano LED pulsed diode excitation source (318 nm). Cyclic voltammetry (CV) curves were recorded in DMF/Bu_4NClO_4 (0.1 M) solution with a three-electrode system consisting of Ag/Ag^+ as the reference electrode, Pt plate as the working electrode, and a Pt wire as the counter electrode using an Electrochemical Measurement System HZ-7000 (HOKUTO DENKO).

Syntthesis

7,7'-(pyrazine-2,5-diylbis(thiophene-5,2-diyl))bis(9-butyl-N,N-diphenyl-9H-carbazol-2-amine) (2,5-PD): A solution of **1** (0.20 g, 0.31 mmol), 2,5-dibromopyrazine (38 mg, 0.16 mmol) and $Pd(PPh_3)_4$ (3 mg, 7.9 μmol) in 2.5 ml of toluene was stirred at 110°C for 10 h. The resulting residue was dissolved in dichloromethane and washed with water three times. The organic layer was concentrated and the residue was purified by chromatography on silica (hexane-ethyl acetate = 7 : 1 as eluent) to give **2,5-PD** (0.11 g, 70%) as an orange solid; mp. >300°C; IR(ATR) $\tilde{\nu}$ = 1591, 1491, 1458 cm^{-1}; ^{1}H NMR

(400 MHz, CD_2Cl_2) δ = 0.89 (t, J = 7.4 Hz, 6H), 1.27-1.37 (m, 4H), 1.74-1.81 (m, 4H), 4.20 (t, J = 7.2 Hz, 4H), 6.95 (dd, J = 2.0 and 8.4 Hz, 2H), 7.03 (t, J = 7.2 Hz, 4H), 7.13-7.16 (m, 10H), 7.25-7.30 (m,8H), 7.51 (d, J = 3.6 Hz, 2H), 7.57 (dd, J = 1.6 and 8.4 Hz, 2H), 7.67 (d, J = 0.8 Hz, 2H), 7.73 (d, J = 4.0 Hz, 2H), 7.94 (d, J = 8.4 Hz, 2H), 8.02 (d, J = 8.0 Hz, 2H), 8.93 (s, 2H) ppm; ^{13}C NMR (100 MHz, CD_2Cl_2); δ = 14.04, 20.86, 31.46, 43.09, 105.30, 106.22, 117.53, 117.67, 118.64, 120.49, 121.26, 123.01, 123.41, 124.43, 124.56, 126.74, 129.57, 130.98, 139.67, 140.56, 141,63, 142.84, 146.13, 147.10, 148.60, 149.09 ppm; HRMS (ESI): m/z (%): [M + H^+] calcd for $C_{68}H_{57}N_6S_2$, 1021.40806; found 1021.40906.

7,7'-(pyrazine-2,6-diylbis(thiophene-5,2-diyl))bis(9-butyl-N,N-diphenyl-9H-carbazol-2-amine) (2,6-PD): A solution of **1** (0.10 g, 0.16 mmol), 2,6-diiodopyrazine (25 mg, 0.08 mmol) and $Pd(PPh_3)_4$ (1.5 mg, 1.3 μmol) in 1.3 ml of toluene was stirred at 110°C for 10 h. The resulting residue was dissolved in dichloromethane and washed with water three times. The organic layer was concentrated and the residue was purified by chromatography on silica (dichloromethane-hexane = 3 : 1 as eluent) to give **2,6-PD** (58 mg, 72%) as a yellow solid; mp. 273-275°C; IR(ATR) $\tilde{\nu}$ = 1595, 1493, 1449 cm^{-1}; ^{1}H NMR (400 MHz, CD_2Cl_2) δ = 0.89 (t, J = 7.4 Hz, 6H), 1.29-1.35 (m, 4H), 1.76-1.83 (m, 4H), 4.23 (t, J = 7.2 Hz, 4H), 6.96 (dd, J = 1.6 and 8.4 Hz, 2H), 7.02-7.06 (m, 4H), 7.14-7.16 (m, 10H), 7.25-7.30 (m,8H), 7.53 (d, J = 3.8 Hz, 2H), 7.60 (dd, J = 1.5 and 8.1 Hz, 2H), 7.71 (d, J = 1.2 Hz, 2H), 7.79 (d, J = 3.8 Hz, 2H), 7.95 (d, J = 8.4 Hz, 2H), 8.03 (d, J = 8.4 Hz, 2H), 8.81 (s, 2H) ppm; ^{13}C NMR (100 MHz, CD_2Cl_2); δ = 14.06, 20.86, 31.46, 43.07, 105.32, 106.28, 117.54, 117.82, 118.64, 120.49, 121.27, 123.01, 123.45, 124.43, 124.51, 127.57, 129.57, 131.03, 137.88, 140.28, 141,65, 142.85, 147.10, 147.72, 148.60, 149.68 ppm; HRMS (APCI): m/z (%): [M + H^+] calcd for $C_{68}H_{57}N_6S_2$, 1021.40806; found

1021.40930. (The melting point of **2,6-PD** is higher than that of our previous work (ref. 10) because of the improvement of the purification by chromatography.)

Results and Discussion

The D-π-A-π-D dyes **2,5-PD** and **2,6-PD** have been prepared by Stille coupling of halogenated pyrazines (2,5-dibromopyrazine and 2,6-diiodopyrazine) with stannylated D-π component (diphenylamino-thienylcarbazole) using $Pd(PPh_3)_4$ as a catalyst (Scheme 1). The photoabsorption and fluorescence spectra of **2,5-PD** and **2,6-PD** in various organic solvents (toluene, 1,4-dioxane, ethyl acetate, THF and DMF) ware shown in Figure 2, and their optical properties ware summarized in Table 1. In all the solvents, **2,5-PD** and **2,6-PD** exhibit an absorption maxima at around 450 and 400 nm, respectively, which is originating from ICT transition from two diphenylamino-carbazole moiety to pyrazine ring. Thus, photoabsorption band of **2,5-PD** showed red-shift compared to **2,6-PD**. Interestingly, for **2,6-PD**, the shoulder band was observed at around 430 nm. Molar extinct coefficients (ε) values of **2,5-PD** (81800-87300 M^{-1} cm^{-1}) are higher than those of **2,6-PD** (73300-78300 M^{-1} cm^{-1}) in all the solvents. In contrast to the photoabsorption properties, the two dyes showed positive fluorescence solvatochromism by changing solvents from non-polar (λ_{em} = 513 and 480 nm for **2,5-PD** and **2,6-PD** in toluene, respectively) to polar (λ_{em} = 614 and 588 nm for **2,5-PD** and **2,6-PD** in DMF, respectively) solvents. Thus, the Stokes shift (SS) values of the two dyes increased with increase in the solvent polarity. However, SS values of **2,6-PD** (4104-8055 cm^{-1}) are larger than those of **2,5-PD** (2533-5643 cm^{-1}) in all the solvents. In addition, the fluorescence quantum yields (Φ_f) of **2,5-PD** (0.31-0.75) are higher than those of **2,6-PD** (0.14-0.65). The time-resolved spectroscopy of the two dyes revealed that the decay profile can fit with a single exponential function in all the solvents. The radiative (k_r) and non-radiative rate constant (k_{nr}) of the dyes were estimated from the fluorescence lifetime (τ) and Φ_f. The k_s of **2,5-PD** (1.68-7.56×10^8 s^{-1}) is about twice as high as **2,6-PD** (0.83-

3.60×10^8 s^{-1}). On the other hand, k_{nr} of **2,5-PD** ($2.12\text{-}3.86\times10^8$ s^{-1}) are almost the same values to **2,6-PD** ($1.55\text{-}5.09\times10^8$ s^{-1}). The ratio of radiative to non-radiative rate constant (k_r / k_{nr}) of **2,5-PD** is larger than that of **2,6-PD**. Therefore, the high Φ_f of **2,5-PD** is attributed to the high k_r value of **2,5-PD** relative to **2,6-PD**.

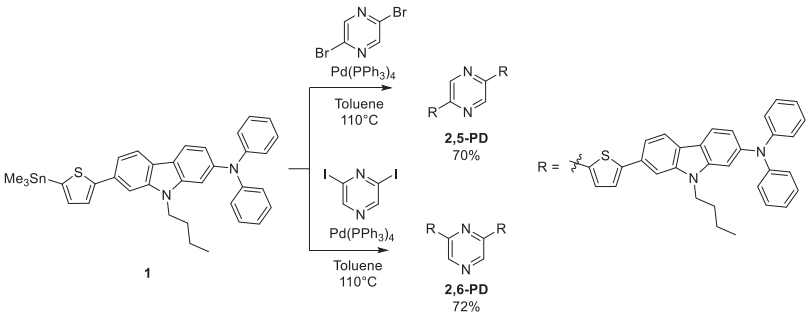

Scheme 1. Synthesis of pyrazine-based fluorescent D-π-A-π-D dyes **2,5-PD** and **2,6-PD**.

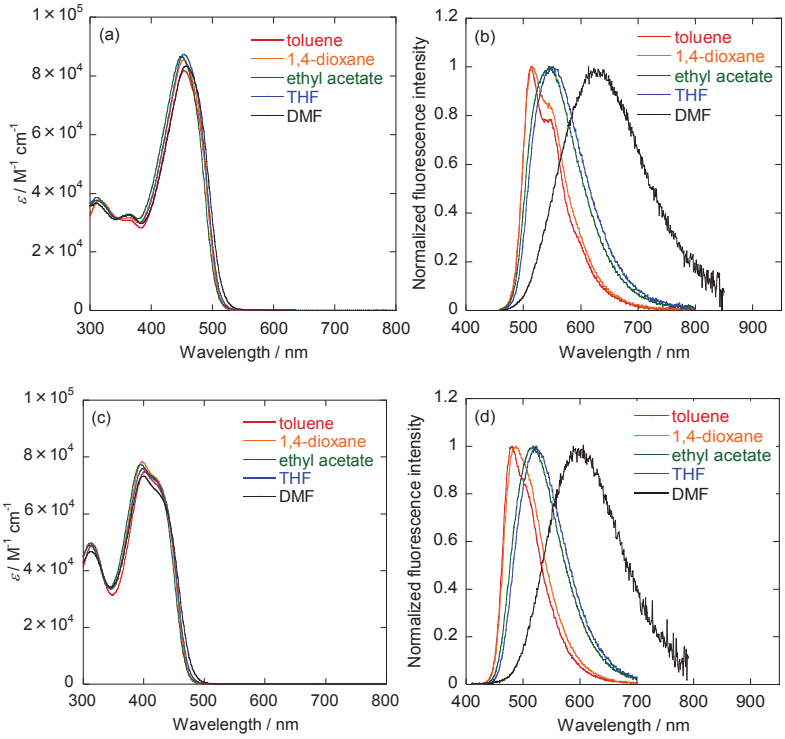

Figure 2. (a) UV/vis absorption (c = 1.0 × 10^{-5} M) and (b) fluorescence spectra (c = 5.0 × 10^{-6} M, λ_{ex} = 450 nm) of **2,5-PD** in various solvents. (c) UV/vis absorption (c = 1.0 × 10^{-5}) and (d) fluorescence spectra (c = 5.0 × 10^{-6} M, λ_{ex} = 400 nm) of **2,6-PD** in toluene, 1,4-dioxane, ethyl acetate, THF and DMF.

Table 1. Optical data of **2,5-PD** and **2,6-PD** in various solvents

Dye	Solvent	λ_{abs} / nm (ε / M^{-1} cm^{-1})	λ_{em} / nm (Φ_f) [a]	SS / cm^{-1} [b]	τ / ns [c]	k_r / s^{-1} [d]	k_{nr} / s^{-1} [e]	k_r / k_{nr}
2,5-PD	Toluene	454 (81800)	513 (0.66)	2533	0.88	7.50×10^8	3.86×10^8	1.94
	1,4-Dioxane	453 (85500)	517 (0.75)	2732	0.99	7.56×10^8	2.52×10^8	3.00
	Ethyl acetate	454 (87300)	550 (0.62)	3844	1.25	4.96×10^8	3.04×10^8	1.63
	THF	450 (86600)	553 (0.72)	4139	1.32	5.45×10^8	2.12×10^8	2.57
	DMF	456 (83300)	614 (0.31)	5643	1.84	1.68×10^8	3.75×10^8	0.45
2,6-PD	Toluene	401 (74800)	480 (0.48)	4104	1.41	3.40×10^8	3.69×10^8	0.92
	1,4-Dioxane	397 (78300) [f]	486 (0.62) [f]	4655	1.72	3.60×10^8	2.21×10^8	1.63
	Ethyl acetate	398 (75800)	518 (0.55)	5820	2.05	2.68×10^8	2.20×10^8	1.22
	THF	394 (77400)	524 (0.65)	6296	2.26	2.88×10^8	1.55×10^8	1.86
	DMF	399 (73300)	588 (0.14)	8055	1.69	0.83×10^8	5.09×10^8	0.16

[a] Fluorescence quantum yields (Φ_f) were determined by using a calibrated integrating sphere system (λ_{ex} = 450 nm and 400 nm for **2,5-PD** and **2,6-PD**, respectively). [b] Stokes shift. [c] Fluorescence lifetime. [d] Radiative rate constant ($k_r = \Phi_f/\tau_f$). [e] Nonradiative rate constant ($k_{nr} = (1 - \Phi_f)/\tau_f$). [f] The ε and Φ_f of the **2,6-PD** in 1,4-dioxane showed a relatively high value compared to that in our previous work (ref. 10) because of the improvement of the purification by chromatography.

To gain insight into the fluorescence solvatochromisms of the two dyes, the difference in the dipole moment ($\Delta\mu$) between the ground and excited state were estimated by using following Lippert-Mataga equation (eq. 1)[11]

$$\Delta\nu = \frac{1}{4\pi\varepsilon_0} \cdot \frac{2\Delta\mu^2}{hca^3} \Delta f \qquad (1)$$

where $\Delta\nu$ is the SS value in wavenumber, ε_0 is vacuum permittivity, h is Planck's constant, c is velocity of light, a is the Onsager radius of the dye molecule estimated by DFT calculation (5.68 Å and 4.82 Å for **ET-1** and **9-MP**, respectively) and $\Delta\mu$ is the difference in the dipole moment of the dyes between the ground (μ_g) and the excited (μ_e) state, respectively. Δf is the orientation polarizability defined by following equation (eq 2)

$$\Delta f = \frac{\varepsilon - 1}{2\varepsilon + 1} - \frac{n^2 - 1}{2n^2 + 1} \qquad (2)$$

where ε and n are the static dielectronic constant and the refractive index of the solvent,

respectively. According to the eq 1, $\Delta\mu$ is estimated as slope of the Lippert-Mataga plots (Figure 3). The plots of the two dyes showed reasonably linear relationship, and the slope of the **2,6-PD** is slightly steeper compared to **2,5-PD**. The $\Delta\mu$ for **2,5-PD** and **2,6-PD** were 23.40 D and 24.86 D, respectively. Consequently, high $\Delta\mu$ value of **2,6-PD** relative to **2,5-PD** is responsible for the large SS value of **2,6-PD** than that of **2,5-PD**, leading to a large solvatofluorochromism of **2,6-PD** (λ_{em} = 513-614 and 480-588 nm for **2,5-PD** and **2,6-PD**, respectively). However, the difference in $\Delta\mu$ values between **2,5-PD** and **2,6-PD** is small, although the orientation of the two D-π moieties is different between the two dyes. In fact, the μ_g values of **2,5-PD** (1.87 D) and **2,6-PD** (0.42D) based on the DFT calculation at the B3LYP/6-31G(d,p) level demonstrated that the difference in the μ_g values between the two dyes is also small.

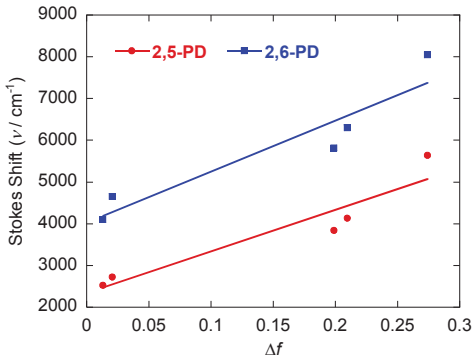

Figure 3. Plots of the Stokes shift *vs.* Lippert-Mataga solvent polarity (Δf); solvent (ε, n, Δf)[12] : toluene (2.38, 1.4969, 0.0132), 1,4-dioxane (2.21, 1.4224, 0.0205), ethyl acetate (6.02, 1.3724, 0.199), THF (7.58, 1.4072, 0.2096) and DMF (36.71, 1.4305, 0.274).

The electrochemical properties of **2,5-PD** and **2,6-PD** were investigated by cyclic voltammetry in DMF containing 0.1 M of tetrabutylammonium perchlorate (Bu_4NClO_4) (Figure 4), and the electrochemical parameters are summarized in Table 2. It was found that the two dyes showed a reversible oxidation wave at the same potential (E_{pa} = 0.40 V, E_{pc} = 0.35 V vs. Fc/Fc^+) in this potential window from –0.1 to 0.6 V vs. Fc/Fc^+, and the

peak-to-peak separation ($\Delta E_p = E_{pa} - E_{pc}$) is 50 mV. Thus, the fact suggested that this reversible oxidation process might proceed as one-electron oxidation. The HOMO energy level vs. the vacuum level ($E_{HOMO} = -[E^{ox}_{1/2} + 4.8]$ eV) for the two dyes were estimated to −5.18 eV from their half-wave potential ($E^{ox}_{1/2}$ = 0.38 V vs. Fc/Fc^+). The LUMO energy levels of **2,5-PD** and **2,6-PD** vs. the vacuum level were estimated from eq. [$E_{HOMO} + E_{0\text{-}0}$] eV, where $E_{0\text{-}0}$ is transition energy estimated from intersection of photosbsorption and fluorescence spectra in DMF ($E_{0\text{-}0}$; 512 nm, 2.42 eV for **2,5-PD** and 481 nm, 2.58 eV for **2,6-PD**) which is corresponded to the optical energy gap between the HOMO and the LUMO. Thus, the LUMO energy level of **2,5-PD** (−2.76 eV) is lower than that of **2,6-PD** (− 2.60 eV). Consequently, it was found that the bathochromic shift in photoabsorption band of **2,5-PD** relative to **2,6-PD** is mainly attributed to the low-lying LUMO energy level of **2,5-PD**.

Table 2. Electrochemical data, and HOMO and LUMO energy level of **2,5-PD** and **2,6-PD**

Dye	$E^{ox}_{1/2}$ / V [a]	HOMO / eV [b]	LUMO / eV [b]	$E_{0\text{-}0}$ / eV [c]
2,5-PD	0.38	−5.18	−2.76	2.42
2,6-PD	0.38	−5.18	−2.60	2.58

[a] half wave potential *vs.* Fc/Fc^+. [b] *vs.* the vacuum level. [c] $E_{0\text{-}0}$ were estimated from intersection of UV-Vis absorption and fluorescence spectra in DMF.

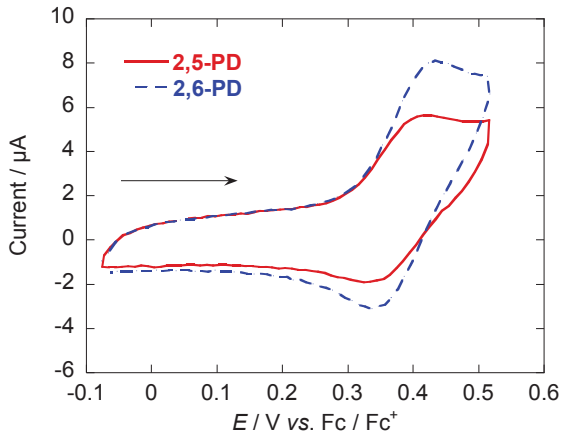

Figure 4. Cyclic voltammograms of **2,5-PD** and **2,6-PD** in DMF containing 0.1 M Bu_4NClO_4 at a scan rate of 0.1 V s^{-1}. The arrow denotes the direction of the potential scan.

To examine the electric structures of **2,5-PD** and **2,6-PD**, the molecular orbitals were calculated using DFT at the B3LYP/6-31G(d,p) level (Figure 5). The DFT calculation indicated that for **2,5-PD** the HOMO is delocalized over the whole of the molecule (Figure 5b) and the LUMO is mainly localized on the thienylpyrazine moiety (Figure 4d). For **2,6-PD** the HOMO is mostly localized on the two diphenylamino-carbazole moieties containing the thiophene ring (Figure 5c) and the LUMO is localized the thienylpyradine moiety (Figure 5e). Accordingly, the DFT calculations demonstrate that the photoexcitation of **2,5-PD** and **2,6-PD** will induce the ICT from the two diphenylaminocarbazole moieties to the thienylpyrazine moiety. For **2,6-PD** the distributions of HOMO and LUMO are well separated. Thus, the charge separation of **2,6-PD** in the exited state is presumed to be larger than that of **2,5-PD**, which may lead to the large $\Delta\mu$ resulting in large SS value of **2,6-PD**. The HOMO energy level of the two dyes are similar to each other (–4.74 and –4.78 eV for **2,5-PD** and **2,6-PD**, respectively), but the LUMO energy level of **2,5-PD** (–2.01 eV) is lower than that of **2,6-PD** (–1.76 eV), which is in good agreement with the experimental results from the photoabsorption and fluorescence spectral analyses (Figure 2) and the cyclic voltammetry measurements (Figure 4). Thus, the bathochromic shift of the absorption band of **2,5-PD** compared to **2,6-PD** is mainly attributed to the more stable LUMO energy level of the **2,5-PD** than that of **2,6-PD**. Furthemore, in order to understand the photoabsorption spectral features of the two dyes, time-dependent density functional theory (TD-DFT) calculations were performed. The calculated λ_{abs}^{max} for **2,5-PD** and **2,6-PD** is 512 and 465 nm, respectively. For both of the λ_{abs}^{max} of the two dyes, $S_0 \rightarrow S_1$ transition is mainly attributed to the transitions from the HOMO to the LUMO (69% and 65% contribution for **2,5-PD** and **2,6-PD**, respectively). Interestingly, $S_0 \rightarrow S_2$ transition is allowed with sufficient

oscillator strength value (f = 0.26) for **2,6-PD**, which is mainly attributed to the transition from the HOMO−1 (located on two diphenylamino-carbazole moieties) to the LUMO (located on thienylpyrazine moiety). The calculated absorption maxima corresponding to $S_0 \rightarrow S_2$ transition is 441 nm for **2,6-PD** that is close to $S_0 \rightarrow S_1$ transition (466 nm). On the other hand, $S_0 \rightarrow S_2$ transition is forbidden for **2,5-PD** (λ_{abs} = 476 nm, f = 0.003). This result revealed that the photoabsorption band of **2,6-PD** at around 400 nm is composed of $S_0 \rightarrow S_1$ and $S_0 \rightarrow S_2$ transitions, leading to the expression of shoulder band at around 430 nm.

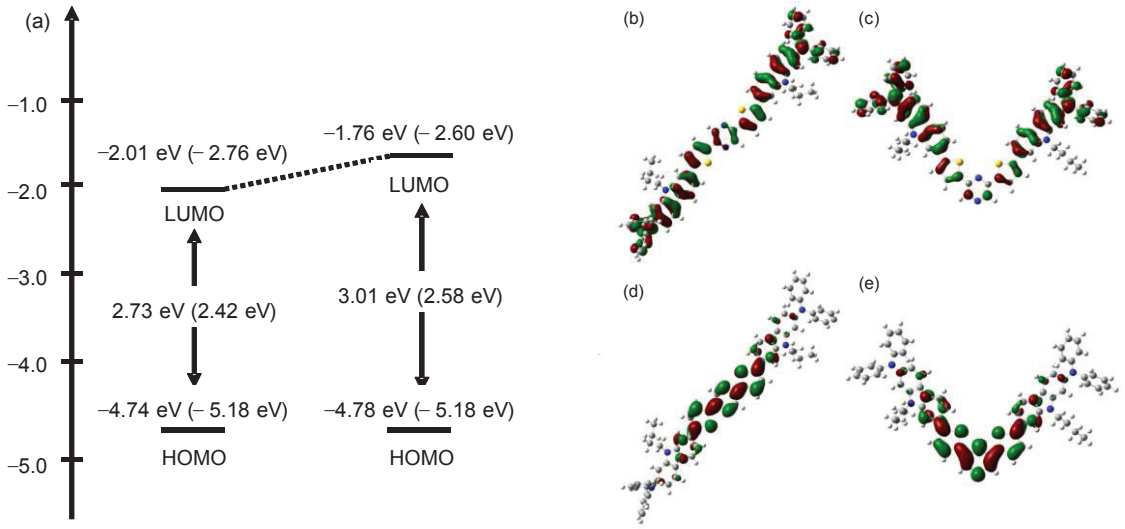

Figure 5. (a) Energy level diagram, HOMO and LUMO of **2,5-PD** and **2,6-PD** derived from DFT calculations. The numbers in parentheses are the experimental values. HOMO of (b) **2,5-PD** and (c) **2,6-PD**. LUMO of (d) **2,5-PD** and (e) **2,6-PD**

Conclusion

The pyrazine-based D-π-A-π-D fluorescent dyes **2,5-PD** and **2,6-PD** which are substituted with two diphenylamine-thienylcarbazole moieties on 2,5- and 2,6-position of a pyrazine ring, respectively, have been developed. Based on the photophysical and electrochemical measurements and DFT calculations, the photoabsorption band of **2,5-PD** showed bathochromic shift compared to **2,6-PD** due to the low-lying LUMO energy level of **2,5-PD**. For both **2,5-PD** and **2,6-PD**, $S_0 \rightarrow S_1$ transition is mainly attributed to the transitions from the HOMO to the LUMO. The Lippert-Mataga plots for **2,5-PD** and **2,6-PD** revealed that the difference in the dipole moments between the excited and ground states for **2,6-PD** is higher than that in **2,5-PD**, resulting in significant fluorescence solvatochromism of **2,6-PD** with large stokes shifts, compared to **2,5-PD**. Thus, it was found that, the introduction of two D-π components on the 2,5-position of the pyrazine ring leads to the bathochromic shift of photoabsorption band due to the stabilization of the LUMO energy level of the dye. Moreover, the introduction of two D-π components on the 2,6-position of the pyrazine ring leads to the expression of the strong solvatofluorochromic properties because of the large $\Delta\mu$ value of the dye. In this chapter, it is demonstrated that pyrazine-based D-π-A-π-D dyes are useful fluorophore for functional fluorescence materials because their optical and electrochemical properties can be tuned by changing the position of the D-π component on the pyrazine ring.

Reference

1. (*a*) S. -L. Lin, L. -H. Chan, R. -H. Lee, M. -Y. Yen, W. -J. Kue, C. -T. Chen and R. -J. Jeng, *Adv. Mater.* **2008**, *20*, 3947; (*b*) A. D'Aléo, M. H. Sazzad, D. H. Kim, E. Y. Choi, J. W. Wu, G. Canard, F. Fages, J. -C. Ribierre and C. Adachi, *Chem. Commun.* **2017**, *53*, 7003.

2. (*a*) N. Zhou, K. Prabakaran, B. Lee, S. H. Chang, B. Harutyunyan, P. Guo, M. R. Butler, A. Timalsina, M. J. Bedzyk, M. A. Ratner, S. Vegiraju, S. Yau, C. -G. Wu, R. P. T. Chang, A. Facchetti, M. -C. Chem and T. J. Marks, *J. Am. Chem. Soc*. **2015**, *137*, 4414; (*b*) Y. Gao, X. Li, Y. Hu, Y. Fan, J. Yuan, N. Robertson, J. Hua and S. R. Marder, *J. Mater. Chem. A*, **2016**, *4*, 12865; (*c*) T. Horiuchi, T. Yashiro, R. Kawamura, S. Uchida and H. Segawa, *Chem. Lett.* **2016**, *45*, 517; (*d*) Y. Adachi, Y. Ooyama, N. Shibayama and J. Ohshita, *Chem. Lett*. **2017**, *46*, 310; (*e*) H. Shimogawa, M. Endo, Y. Nakaike, Y. Murata and A. Wakamiya, *Chem. Lett.* **2017**, *46*, 715.

3. (*a*) A. Goel, S. Umar, P. Nag, A. Sharma, L. Kumar, Shamsuzzama, Z. Hossain, J. R. Gayen and A. Nazir, *Chem. Commun.* **2015**, *51*, 5001; (*b*) Y. Niko, P. Didier, Y. Mely, G. Konishi and A. S. Klymchenko, *Sci. Rep.* **2016**, *6*, 18870; (*c*) Y. J. Wang, Y. Shi, Z. Wang, Z. Zhu, X. Zhao, H. Nie, J. Qian, A. Qin, J. Z. Sun and B. Z. Tang, *Chem. Eur. J.* **2016**, *22*, 9784; (*d*) E. Yamaguchi, C. Wang, A. Fukazawa, M. Taki, Y. Sato, T. Sasaki, M. Ueda, N. Sasaki, T. Higashiyama and S. Yamaguchi, *Angew. Chem. Int. Ed.* **2015**, *54*, 4539.

4. (*a*) E. Deniz, G. C. Isbasar, Ö. A. Bozdemir, L. T. Yildirim, A. Siemiarczuc and E. U. Akkaya, *Org. Lett.* **2008**, *10*, 3401; (*b*) X. Lu, S. Fan, J. Wu, X. Jia, Z. –S. Wang and G. Zhou, *J. Org. Chem.* **2014**, *79*, 6480; (*c*) M. Urban, K. Durka, P. Jankowski and S. Luliński, *J. Org. Chem.* **2017**, *82*, 8234.

5. H. Sunahara, Y. Urano, H. Kojima and T. Nagano *J. Am. Chem. Soc.* **2007**, *129*, 5597.

6. (*a*) D. Signore, R. Nifosi, L. Albertazzi, B. Storti and R. Bizzarri, *J. Am. Chem. Soc.* **2010**, *132*, 1276. (*b*) S. Sasaki, G. P. C. Drummen and G. Konishi, *J. Mater. Chem. C*, **2016**, *4*, 2731.

7. Y. Niko, S. Sasaki, K. Narushima, D. Kumar, M. Vacha and G. Konishi, *J. Org. Chem.* **2015**, *80*, 10794.

8. (*a*) H. Meier, E. Karpuk and H. C. Holst, *Eur. J. Org. Chem*. **2006**, *11*, 2609; (*b*) Z. Yang, W. Qin, J. W. Y. Lam, S. Chen, H. H. Y. Sung, L. D. Williams and B. Z. Tang, *Chem. Sci*. **2013**, *4*, 3725; (*c*) G. Sathiyan and P. Sakthival, *RSC. Adv*. **2016**, *6*, 106705 (*d*) N. A. Nemkovich, H. Detert and V. Schmitt, *J. Photochem. Photobiol. A: Chem.* **2018**, *354*, 139.

9. (*a*) Y. Ooyama, S. Inoue, T. Nagano, K. Kushimoto, J. Ohshita, I. Imae, K. Komaguchi and Y. Harima, *Angew. Chem. Int. Ed.* **2011**, *50*, 7429; (*b*) Y. Ooyama, K. Uenaka and J. Ohshita, *Org. Chem. Front.* **2015**, *2*, 552; (*c*) Y. Ooyama, K. Uenaka and J. Ohshita, *RSC Adv*. **2015**, *5*, 21012.

10. Y. Ooyama, K. Uenaka, Y. Harima and J. Ohshita, *RSC Adv.* **2014**, *4*, 30225.

11. (*a*) E. Z. Lippert, *Naturforsch*, **1955**, *10*, 541; (*b*) N. Mataga, Y. Kaifu and M. Koizumi, *Bull. Chem. Soc. Jpn.* **1956**, *29*, 465.

12. C. Reichardt, *Solvents and Solvent Effects in Organic Chemistry*, Vol. 3, VCH, Weinheim, **2003**.

Chapter 2

Development of a D-π-A pyrazinium photosensitizer possessing singlet oxygen generation

Introduction

Photosensitizers possessing the ability to generate singlet oxygen ($^1O_2$) upon visible-NIR light irradiation have received considerable attention in recent years from the viewpoint of not only fundamental study in photochemistry and photophysics but also their potential applications in photodynamic therapy (PDT).[1-4] $^1O_2$ was generated through the following processes: initially the photosensitizer was photoexcited (*hv*) to generate the singlet excited state of the photosensitizer ($^1S^*$), then the photoexcited dye ($^1S^*$) undergoes intersystem crossing (ISC) to generate the triplet excited state ($^3S^*$). Subsequent energy transfer from the photoexcited dye ($^3S^*$) to triplet (ground state) oxygen ($^3O_2$) produces $^1O_2$ (Figure 1). Thus, to enhance ISC efficiency is one of the most effective strategies to improve $^1O_2$ quantum yield. For this purpose, many kinds of photosensitizers possessing high $^1O_2$ generation efficiency have been developed such as methylene blue[5] and rose bengal,[6] porphyrin dyes,[7] boron dipyrromethene (BODIPY) dyes,[8] fullerene derivatives[9] and transition metal complexes,[10] and the mechanisms of $^1O_2$ generation by the photosensitizers were investigated.[1-4,11] However, there have been few efforts to develop new organic photosensitizers possessing the ability to generate $^1O_2$.[12] Thus, to gain insight into a direction in molecular design for creating new photosensitizers possessing $^1O_2$ generation, D-π-A-π-D pyrazinium dyes (**PD-Br** and **PD-I**) bearing bromide ion (Br^-) or iodide ion (I^-) as a counter anion have been developed (Figure 2). The heavy atom effect of the counter anion (Br^- and I^-) would promote the formation of the triplet excited state

of the photosensitizers by facilitating the ISC efficiency. Interestingly, it was found that the D-π-A-π-D pyrazinium dyes show specific solvatochromism, leading to a large bathochromic shift of photoabsorption band in halogenated solvents, compared to polar and non-polar solvents. Therefore, the effects of the counter anion and solvents on the $^1O_2$ generation efficiency have been investigated. Based on the evaluation of the quantum yield ($\Phi_\triangle$), rate constant (k_s) for $^1O_2$ generation, the HOMO and LUMO energy levels of **PD-Br** and **PD-I**, and density functional theory (DFT) calculation, the photoabsorption and $^1O_2$ generation properties of the D-π-A-π-D pyrazinium dyes are discussed.

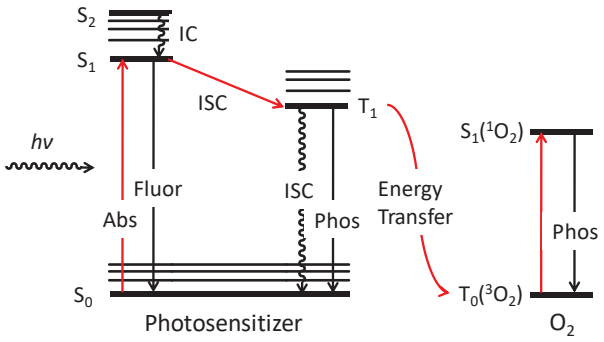

Figure 1. Mechanisms of $^1O_2$ generation through the energy transfer from photoexcited photosensitizer to ground state oxygen.

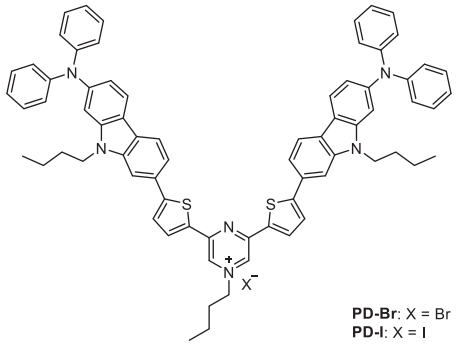

Figure 2. Chemical structures of D-π-A-π-D pyrazinium dyes **PD-Br** and **PD-I**

Experimental

General

Melting points were measured with a Yanaco micro melting point apparatus MP model. IR spectra were recorded on a SHIMADZU IRAffinity-1 spectrometer by ATR method. Highresolution mass spectral data were acquired on a Thermo Fisher Scienti LTQ Orbitrap XL. ^{1}H and ^{13}C NMR spectra were recorded on a Varian-400 (400 MHz) FT NMR spectrometer. Photoabsorption spectra were observed with a HITACHI U-2910 spectrophotometer. Cyclic voltammetry (CV) curves were recorded in and acetonitrile/Bu_4NClO_4 (0.1 M) solution with a three-electrode system consisting of Ag/Ag+ as reference electrode, Pt plate as working electrode, and Pt wire as counter

Syntthesis

1-Butyl-3,5-bis(5-(9-butyl-7-(diphenylamino)-9H-carbazol-2-yl)thiophen-2-yl)pyrazin-1-ium bromide (PD-Br). A solution of **2,6-PD** (0.15 g, 0.15 mmol) and 1-bromobutane (1.28 g, 9.4 mmol) in DMF (8 ml) was stirred at 80 °C for 5 days under an argon atmosphere. After concentrating under reduced pressure, the resulting residue was subjected to reprecipitation from dichloromethane–hexane. The reprecipitation solid was chromatographed on reverse-phase silica gel (chloroform–methanol = 1 : 3 as eluent) to give **PD-Br** (0.078 g, yield 46%) as dark red solids; mp 152–153 °C; IR (ATR): $\tilde{\nu}$ = 1624, 1591, 1526, 1487, 1445, 1427 cm^{-1} ; ^{1}H NMR (400 MHz, DMSO-d_6) δ = 0.83 (t, J = 7.4 Hz, 6H), 1.01 (t, J = 7.5 Hz, 3H), 1.19–1.26 (m, 4H), 1.46–1.52 (m, 2H), 1.65–1.73 (m, 4H), 2.07–2.14 (m, 2H), 4.35 (t, J = 7.0 Hz, 4H), 4.58 (t, J = 7.3 Hz, 2H), 6.89 (dd, J = 1.8 and 8.4 Hz, 2H), 7.04–7.09 (m, 12H), 7.18 (d, J = 1.7 Hz, 2H), 7.31–7.36 (m, 8H), 7.66 (dd, J = 1.5 and 8.3 Hz, 2H), 7.98 (d, J = 4.0 Hz, 2H), 8.06 (s, 2H), 8.10 (d, J = 8.4 Hz, 2H), 8.16 (d, J = 8.1 Hz, 2H), 8.25 (d, J = 4.0 Hz, 2H), 9.51 (s, 2H) ppm; ^{13}C NMR

(100 MHz, DMSO-d_6) δ = 13.49, 13.71, 19.06, 19.75, 30.68, 32.23, 34.40, 41.80, 104.80, 106.26, 116.73, 117.48, 117.68, 120.58, 121.62, 122.90, 123.03, 123.59, 123.71, 129.38, 129.50, 136.45, 140.89, 140.95, 142.12, 146.34, 147.57, 147.63, 151.89, 152.04 ppm; HRMS (ESI): m/z (%): calcd for $C_{72}H_{65}N_6S_2^+$ 1077.47066; found 1077.47144.

1-Butyl-3,5-bis(5-(9-butyl-7-(diphenylamino)-9H-carbazol-2-yl)thiophen-2-yl)pyrazin-1-ium iodide (PD-I). A solution of **2,6-PD** (0.045 g, 0.04 mmol) and 1-iodobutane (0.81 g, 4.4 mmol) in DMF (3 ml) was stirred at 80 °C for 3 days under an argon atmosphere. After concentrating under reduced pressure, the resulting residue was subjected to reprecipitation from dichloromethane–hexane to give **PD-I** (0.042 g, yield 77%) as dark red solids; mp 227–228 °C; IR (ATR): $\tilde{\nu}$ = 1624, 1591, 1528, 1487, 1445, 1425 cm^{-1} ; ^{1}H NMR (400 MHz, DMSO-d_6) δ = 0.83 (t, J = 7.5 Hz, 6H), 1.01 (t, J = 7.4 Hz, 3H), 1.18–1.27 (m, 4H), 1.44–1.52 (m, 2H), 1.65–1.73 (m, 4H), 2.06–2.14 (m, 2H), 4.35 (t, J = 7.0 Hz, 4H), 4.58 (t, J = 7.7 Hz, 2H), 6.89 (dd, J = 1.8 and 8.4 Hz, 2H), 7.04–7.09 (m, 12H), 7.18 (d, J = 1.7 Hz, 2H), 7.31–7.36 (m, 8H), 7.66 (dd, J = 1.4 and 8.1 Hz, 2H), 7.98 (d, J = 4.0 Hz, 2H), 8.06 (s, 2H), 8.10 (d, J = 8.4 Hz, 2H), 8.16 (d, J = 8.2 Hz, 2H), 8.25 (d, J = 4.0 Hz, 2H), 9.50 (s, 2H) ppm; ^{13}C NMR (100 MHz, DMSO-d_6) δ = 13.49, 13.71, 19.06, 19.75, 30.69, 32.22, 41.79, 104.81, 106.28, 116.75, 117.50, 117.68, 120.59, 121.61, 122.89, 123.04, 123.69, 129.31, 129.37, 129.50, 136.43, 140.89, 142.12, 146.33, 147.56, 151.90, 152.06 ppm (one aliphatic and two aromatic carbon signals were not observed owing to overlapping resonances); HRMS (ESI): m/z (%): calcd for $C_{72}H_{65}N_6S_2^+$ 1077.47066; found 1077.47131.

Evaluation of $^1O_2$ quantum yield

Quantum yields ($\Phi_\triangle$) for singlet oxygen ($^1O_2$) generation by D-π-A-π-D pyrazinium dyes (**PD-Br** and **PD-I**) in various solvents (THF, acetonitrile, DMSO and dichloromethane)

were evaluated by tracing the photoabsorption spectral change of the known $^1O_2$ scavenger 1,3-diphenylisobenzofuran (DPBF) accompanied by the reaction of DPBF with the generated $^1O_2$, that is, DPBF can trap $^1O_2$ through the photooxidation of DPBF. All the solvents were bubbled with dried air for 15 min. The absorbance of DPBF was adjusted to around 1.0 in air-saturated solvent. Concentration of **PD-Br** or **PD-I** was adjusted with an absorbance of 0.2-0.3 at the irradiation wavelength (509 nm). The air-saturated solution containing the photosensitizer (**PD-Br** or **PD-I**) and DPBF was irradiated with 509 nm (160 μW cm^{-2}) obtained by passage of xenon light through monochromator. The photoabsorption spectral change of DPBF with the photoirradiation was monitored with an interval of 5 s up to 40 s. The absorption band of DPBF at around 410 nm decreased with the increase in the photoirradiation time. The changes in optical density (ΔOD) of DPBF are plotted against the photoirradiation time, and the slope is used to estimate the $\Phi_\triangle$ of **PD-Br** and **PD-I**. The $\Phi_\triangle$ of **PD-Br** and **PD-I** was estimated by the relative method using Rose Bengal (RB) ($\Phi_\triangle$ = 0.80) in methanol as the standard. Therefore, the $\Phi_\triangle$ values were calculated according to the following eqn (1):

$$\Phi_{\Delta sam} = \Phi_{\Delta ref} \frac{m_{sam} \times F_{ref}}{m_{ref} \times F_{sam}} \qquad (1)$$

where $\Phi_{\triangle sam}$ and $\Phi_{\triangle ref}$ are quantum yields of the pyrazinium dyes (**PD-Br** and **PD-I**) and RB, respectively, m_{sam} and m_{ref} are slope of the plot for ΔOD at around 410 nm, which is originating from $^1O_2$ scavenger DPBF, against photoirradiation time respectively, F_{sam} and F_{ref} is light harvesting efficiency defined as $F = 1 - 10^{-OD}$. OD is the absorbance of the photosensitizers at photoirradiation wavelength (509 nm).

Photosensitizing ability

Photosensitizing ability of the D-π-A-π-D pyrazinium dyes (**PD-Br** and **PD-I**) in various

solvents (THF, acetonitrile, DMSO and dichloromethane) was evaluated by plotting the $\ln(C_t/C_0)$ against the photoirradiation time, where C_t is a concentration of DPBF at the reaction time (t) and C_0 is the initial concentration of DPBF before photoirradiation. All the solvents were bubbled with air for 15 min. The air-saturated solution containing the photosensitizer (1.0×10^{-5} M for **PD-Br** and **PD-I**, 1.0×10^{-6} M for RB) and DPBF (5.0×10^{-5} M) was irradiated with visible light (> 510 nm, 6 mW cm^{-2}) obtained by passage of xenon light through a 510 nm long path filter. The absorbance of DPBF was adjusted to around 1.0 in air-saturated solvent. The photooxidation of DPBF with the photoirradiation was monitored by following the decrease in the photoabsorption at around 410 nm with an interval of 20 s up to 10 min. The concentration (C_t) of DPBF at the reaction time (t) was calculated by Lambert–Beer law ($A_{DPBF} = \varepsilon cl$). The $\ln(C_t/C_0)$ decreased almost linearly with the increase in the photoirradiation time due to the photooxidation of DPBF, that is, the slope was used to estimate the rate constants (k_s).

$^1O_2$ detection by EPR spin-trapping method with 4-oxo-TEMP

The EPR spectra were recorded on a JEOL JES-RE1X spectrometer under the following experimental conditions: temperature 298 K, microwave power 1 mW, microwave frequency 9.439 GHz, field modulation 0.2 mT at 100 kHz, and scan time 4 min. The air-saturated THF solution containing **PD-I** (0.01 mM) as the photosensitizer and 4-oxo-TEMP (50 mM) as the spintrapping agent was irradiated with visible light (> 510 nm, 14 mW cm^{-2} for 30 min) obtained by passage of xenon light through a 510 nm long path filter.

Phosphorescence measurement of $^1O_2$

Phosphorescence spectrum of $^1O_2$ was recorded on a HORIBA NanoLog spectrometer equipped with a 450 W xenon lamp and a photomultiplier tube (NIR-PMT R5509-43 liquid nitrogen configurations, Hamamatsu photonics). The phosphorescence maximum of $^1O_2$ produced upon the excitation of **PD-I** (0.07 mM THF solution) at 467 nm was clearly observed at around 1270 nm.

Results and discussion

The D-π-A-π-D pyrazinium dyes (**PD-Br** and **PD-I**) were synthesized from the D-π-A-π-D fluorescent dye **2,6-PD** (Chapter 1) and the corresponding *n*-butyl halide.

The photoabsorption spectra of **PD-Br** and **PD-I** in various solvents (THF, acetonitrile, DMSO and dichloromethane) were shown in Figure 3 and the optical data were summarized in Table 1. The two pyrazinium dyes possesses broad absorption band at 500-700 nm, which is originationg from ICT transition from electron-donating (diphenylamino-carbazole) moiety to electron-withdrawing (thienylpyrazine) moiety. Interestingly, specific solvatochromism as is the case with the previous reported D-π-A pyridinium dyes. The two dyes showed strong red-shift in photoabsorption band in dichloromethane compared with that in the other solvents. In fact, the λ_{abs} for ICT bands of **PD-Br** and **PD-I** in dichloromethane occurs at a longer wavelength by ca. 30 nm and ca. 70 nm, respectively, than those in acetonitrile. It is worthy to note here that the specific solvatochromism depends on the counter anion of the D-π-A-π-D pyrazinium dyes, that is, the bathochromic shifts of ICT band for **PD-I** bearing I^- ion is larger than that of **PD-Br** bearing Br^- ion.

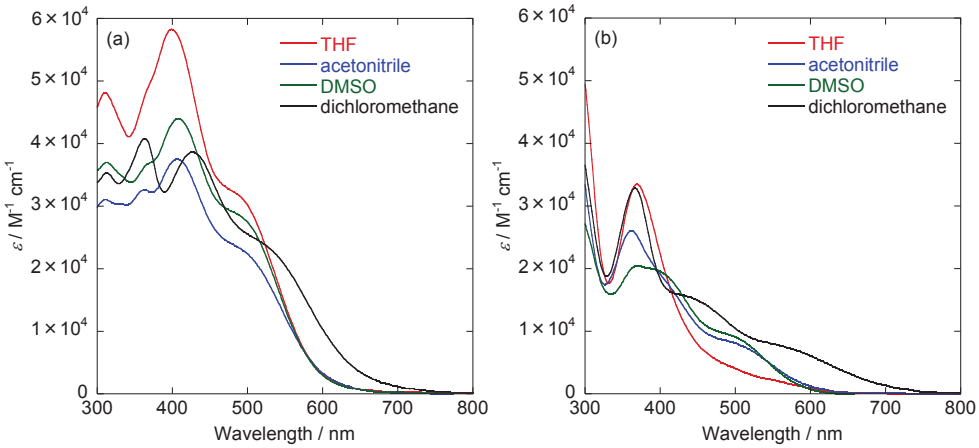

Figure 3. Photoabsorption spectra of (a) **PD-Br** and (b) **PD-I** in various solvents (THF, acetonitrile, DMSO and dichloromethane).

Table 1. Optical data of **PD-Br** and **PD-I**, and $^1O_2$ quantum yield ($\Phi_\triangle$) and first-order rate constant (k_s) for the photooxidation of DPBF using **PD-Br** and **PD-I** as photosensitizer

Dye	Solvent	λ^{abs} for ICT band / nm	ε / M^{-1} cm^{-1} (λ^{abs} = 509 nm)	$\Phi_\triangle$[a]	k_s[b] / min^{-1}
PD-Br	THF	490	28 200	0.19	0.034
	Acetonitrile	490	21200	–[c]	–
	DMSO	490	26000	–[c]	0.004
	Dichloromethane	520	24900	–[c]	0.006
PD-I	THF	500	3600	0.22	0.016
	Acetonitrile	500	7600	0.05	0.032
	DMSO	500	8500	0.03	0.006
	Dichloromethane	570	9700	0.07	0.160[d]

[a] $^1O_2$ quantum yield (relative decomposition rate of DPBF), with Rose Bengal (RB) as standard ($\Phi_\triangle$ = 0.80 in methanol[10a]) and 1,3-diphenylisobenzofuran (DPBF) as $^1O_2$ scavenger. These values were estimated under an assumption that the reactivity of $^1O_2$ is independent of the kind of solvents. [b]First-order rate constant for the reaction of DPBF with $^1O_2$ generated upon photoexcitation of **PD-Br** or **PD-I**. The k_s for RB is 0.250 min^{-1}. [c]Too low. [d]Estimated from the slope for the range of 5-10 min in Figure 11b.

The electrochemical properties of **PD-Br** and **PD-I** were determined by cyclic voltammetry (CV) in acetonitrile containing 0.1 M tetrabutylammonium perchlorate (Bu_4NClO_4). The potentials were referred to ferrocene/ferrocenium (Fc/Fc^+) as the internal reference (Figure 4). For **PD-I**, the oxidation wave for the iodide counter ion was observed at around 0.05 V. The oxidation waves were observed at 0.43 V for **PD-Br** and 0.35 V for **PD-I**, respectively, vs. Fc/Fc^+. The corresponding reduction waves appeared at 0.36 V for **PD-Br** and 0.18 V for **PD-I**, respectively. However, the oxidation and corresponding reduction waves are reversible for **PD-Br**, but irreversible for **PD-I**. The HOMO energy level vs. vacuum level is −5.20 eV for **PD-Br** and −5.07 eV for **PD-I**, respectively, which was evaluated through equation $-[E^{ox}_{1/2} + 4.8]$ eV from the half-wave potential for oxidation ($E^{ox}_{1/2}$ = 0.40 V vs. Fc/Fc^+ for **PD-Br** and 0.27 V vs. Fc/Fc^+ for **PD-I**). On the other hand, the LUMO energy level is −3.20 eV for **PD-Br** and −3.07 eV for **PD-I**, respectively, which was estimated from the HOMO and the onset of photoabsorption spectra (620 nm; 2.0 eV for both **PD-Br** and **PD-I**) in acetonitrile.

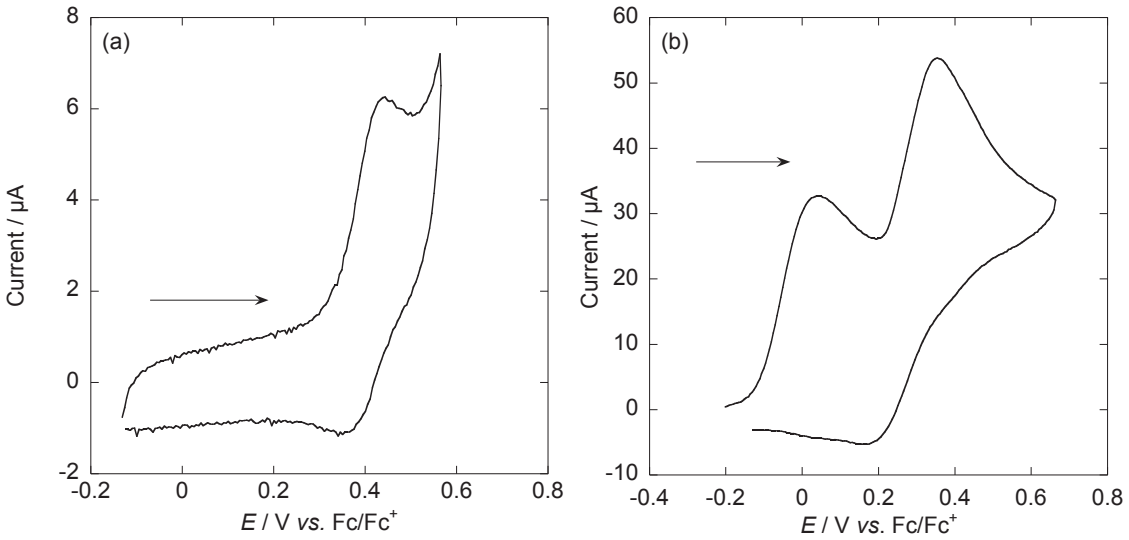

Figure 4. Cyclic voltamograms of (a) **PD-Br** and (b) **PD-I** in acetonitrile containing 0.1 M Bu_4NClO_4. The arrows denote the direction of the potential scan.

To examine the electric structures of **PD-Br** and **PD-I**, the molecular orbitals were calculated for the common cationic component (**PD**+) using DFT at the B3LYP/6-31G(d,p) level for the (Figure 5). The DFT calculation indicated that for **PD**+ the HOMO is mainly localized on the diphenylamine–carbazole moiety (Figure 5a), and the LUMO is mainly concentrated on pyrazinium moiety (Figure 5b). Accordingly, the DFT calculations reveal that excitation of the dye upon light irradiation induces a strong ICT from the diphenylamine–carbazole moiety to the pyrazinium moiety.

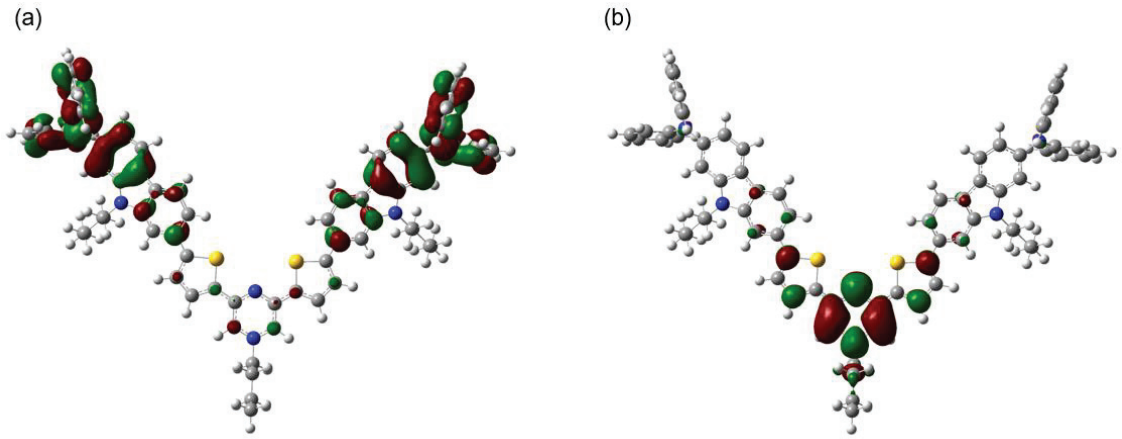

Figure 5. (a) The HOMO and the (b) LUMO of cationic component of the D-π-A-π-D pyrazinium dye (**PD**+).

$^1O_2$ generation by D-π-A-π-D pyrazinium dyes **PD-Br** and **PD-I** in various solvents (THF, acetonitrile, DMSO and dichloromethane) was evaluated by monitoring the photoabsorption spectral change of DPBF accompanied by photooxidation of DPBF by photogenerated $^1O_2$. All the solvents were bubbled with air for 15 min. The air-saturated solution containing the dye (**PD-Br** or **PD-I**) and DPBF was irradiated with 509 nm (160 μW cm^{-2}). The absorption band of DPBF at around 410 nm decreased with the increase in the photoirradiation time (Figure 6 and 7), which indicate the reaction of DPBF with $^1O_2$ generated upon the excitation of pyrazinium dyes. To gain insight into the effect of the solvent and the counter anion upon the efficiency of $^1O_2$ generation, the changes in optical density (ΔOD) of DPBF are plotted against the photoirradiation time (Figure 8), and the slope (m_s) is used to estimate the $\Phi_\triangle$ for **PD-Br** and **PD-I**. It was revealed that the m_s value for **PD-I** becomes steeper in the following order: DMSO (-0.4×10^{-3}) < acetonitrile (-0.5×10^{-3}) < dichloromethane (-0.8×10^{-3}) < THF (-2.6×10^{-3}), that is, the m_s value in THF is larger than those in the other solvents. It was also found that the m_s value of **PD-I** is larger than that of **PD-Br** (-2.0×10^{-3} in THF). Consequently, this

result indicates that THF is a favorable solvent for the D-π-A-π-D pyrazinium dyes to present a high oxidation efficiency for DPBF compared with the other solvents. In addition, this result demonstrated that **PD-I** bearing I^- ion possesses higher photooxidation ability for DPBF than **PD-Br** bearing Br^- ion. Thus, the $\Phi_\triangle$ for **PD-Br** and **PD-I** were estimated by relative method utilizing RB in methanol ($\Phi_\triangle$ = 0.80) as standard. The $\Phi_\triangle$ values of **PD-I** are 0.03, 0.05, 0.07 and 0.22 in DMSO, acetonitrile, dichloromethane and THF, respectively. A higher $\Phi_\triangle$ value in THF is ascribable to that as for the D-π-A-π-D pyrazinium dyes the ISC from $^1S^*$ to the $^3S^*$ may be facilitated in THF, although further study for the solvent effects on $^1O_2$ generation is necessary to ensure the hypothesis. It is worth mentioning here that the $\Phi_\triangle$ values of **PD-I** in all the four solvents are higher than those of **PD-Br**. Therefore, the high $\Phi_\triangle$ value of **PD-I** relative to **PD-Br** is attributed to superior heavy-atom effect of I^- ion rather than Br^- ion, resulting in the facilitation of the ISC.

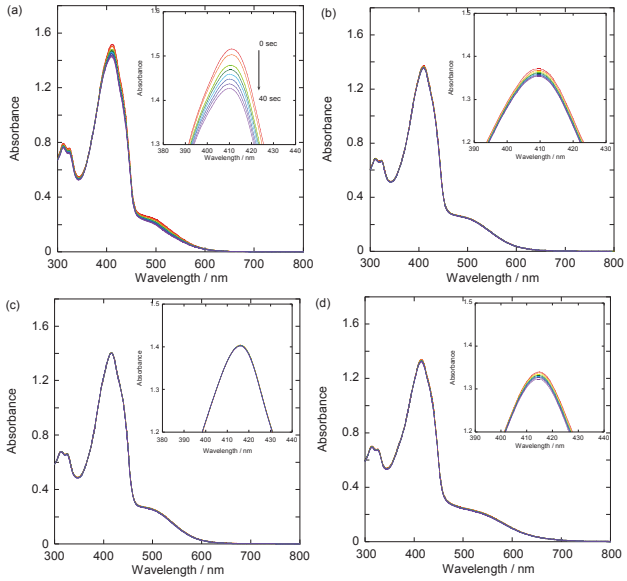

Figure 6. Photoabsorption spectral changes for the photooxidation of DPBF using **PD-I** as photosensitizer under photoirradiation with 509 nm (160 mW cm^{-2}) in (a) THF (7.2×10^{-5} M), (b) acetonitrile (3.3×10^{-5} M), (c) DMSO (3.1×10^{-5} M) and (d) dichloromethane (2.6×10^{-5} M).

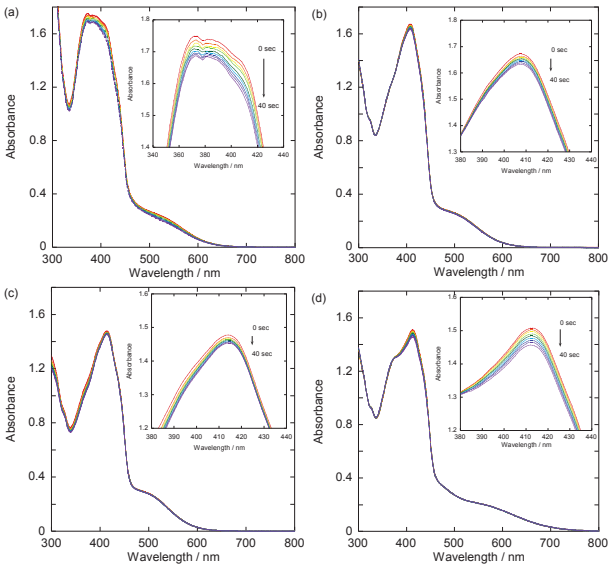

Figure 7. Photoabsorption spectral changes for the photooxidation of DPBF using **PD-I** as photosensitizer under photoirradiation with 509 nm (160 mW cm^{-2}) in (a) THF (7.2×10^{-5} M), (b) acetonitrile (3.3×10^{-5} M), (c) DMSO (3.1×10^{-5} M) and (d) dichloromethane (2.6×10^{-5} M).

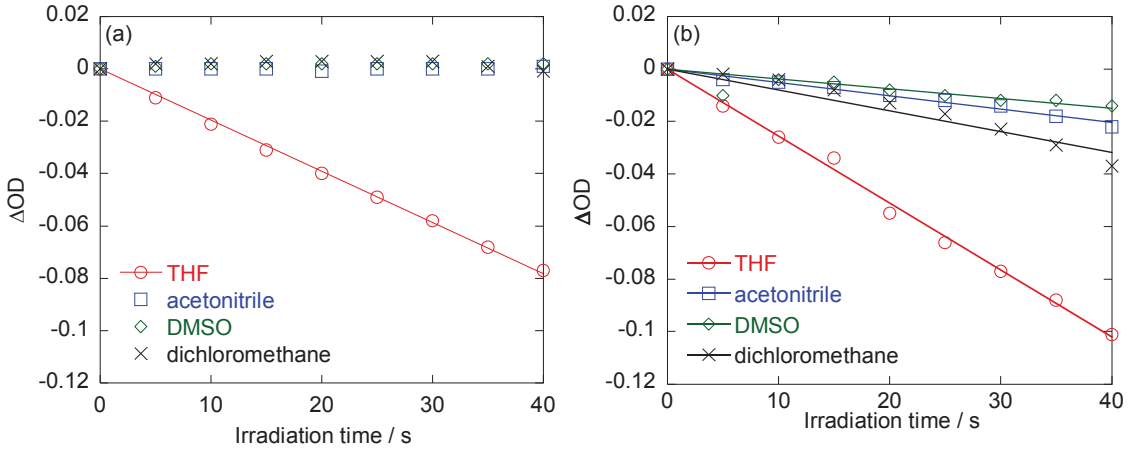

Figure 8. Plots of ΔOD for DPBF against the photoirradiation time for the photooxidation of DPBF using (a) **PD-Br** and (b) **PD-I** as photosensitizers under photoirradiation with 509 nm (160 mW cm^{-2}) in THF, acetonitrile, DMSO and dichloromethane.

In order to evaluate the photosensitizing ability of the D-π-A-π-D pyrazinium dyes, the $\ln(C_t/C_0)$ is plotted against the photoirradiation time, where C_t is a concentration of DPBF at the reaction time (t) and C_0 is the initial concentration of DPBF before photoirradiation (Figure 11). All the solvents (THF, acetonitrile, DMSO and dichloromethane) were bubbled with air for 15 min. The air-saturated solution containing the dye (**PD-Br** or **PD-I**) and DPBF was irradiated with visible light (>510 nm, 6 mW cm^{-2}) obtained by passage of xenon light through a 510 nm long path filter. The photoabsorption spectral changes, which indicate the photooxidation of DPBF, using **PD-Br** and **PD-I** as a photosensitizer are shown in Figure 9 and 10, respectively. The $\ln(C_t/C_0)$ decreased almost linearly with the increase in the photoirradiation time, although the linear relationship for the $\ln(C_t/C_0)$ for **PD-I** in dichloromethane become steeper after the photoirradiation for 5 min under this photoirradiation. Thus, this result indicates the $\ln(C_t/C_0)$ bears a linear relationship with the photoirradiation time to provide the first-order rate constants (k_s) for the photooxidation of DPBF using **PD-Br** and **PD-I** as the photosensitizer (Table 1). The k_s

values for **PD-I** are larger than those of **PD-Br** in acetonitrile, DMSO and dichloromethane, but the k_s value for **PD-I** in THF is lower than that of **PD-Br** due to the lower photoabsorption property of **PD-I** in THF. Interestingly, the plot of **PD-I** in dichloromethane show a non-linear relationship, but the slope for **PD-I** become steeper after 5 min of photoirradiation and the k_s value for **PD-I** in dichloromethane is greater than those in the other solvents. This interesting spectral change may be attributed to not only the bathochromic shift and broadening of absorption but also the enhancement of heavy-atom effect with the increase in the photoirradiation time in dichloromethane, that is, the significant specific solvatochromic behavior of the D-π-A-π-D pyrazinium dye bearing I^- ion. Therefore, this result demonstrates that **PD-I** exhibits more efficient photosensitizing ability compared to **PD-Br**, due to a superior heavy-atom effect of I^- ion.

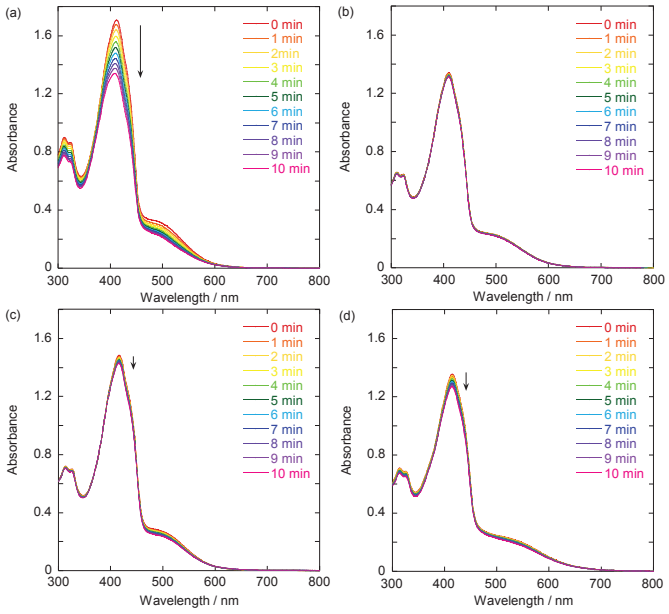

Figure 9. Photoabsorption spectral changes for the photooxidation of DPBF (5.0×10^{-5} M) using **PD-Br** (1.0×10^{-5} M) as photosensitizer under photoirradiation with visible light (>510 nm, 6 mW cm^{-2}) in (a) THF, (b) acetonitrile, (c) DMSO and (d) dichloromethane.

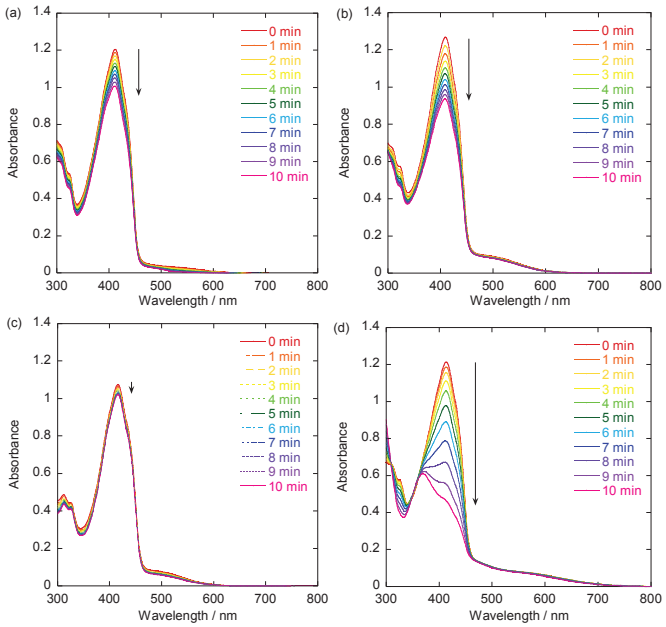

Figure 10. Photoabsorption spectral changes for the photooxidation of DPBF (5.0×10^{-5} M) using **PD-I** (1.0×10^{-5} M) as photosensitizer under photoirradiation with visible light (>510 nm, 6 mW cm^{-2}) in (a) THF, (b) acetonitrile, (c) DMSO and (d) dichloromethane.

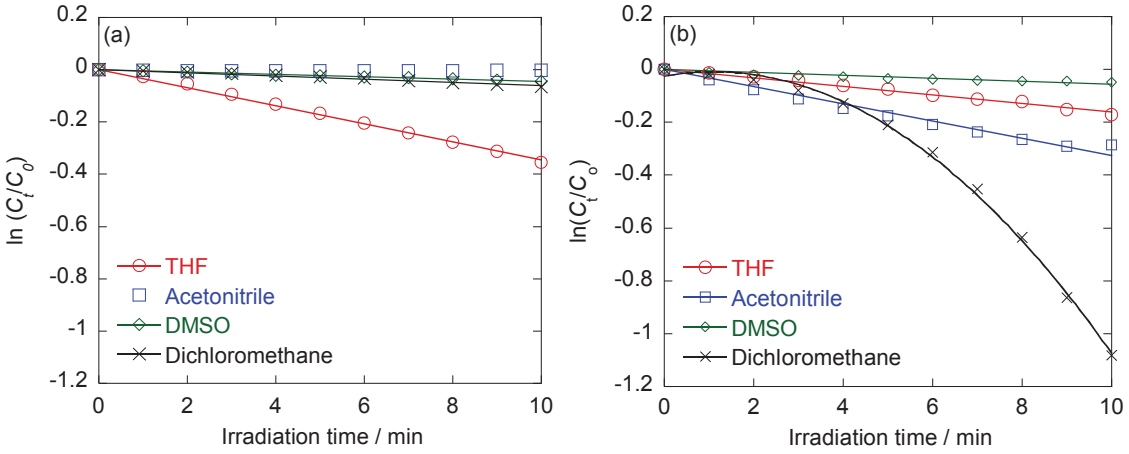

Figure 11. Plots of ln(C_t/C_0) for DPBF against the photoirradiation time for the photooxidation of DPBF using (a) **PD-Br** and (b) **PD-I** as photosensitizers under photoirradiation with visible light (>510 nm, 6 mW cm^{-2}) in THF, acetonitrile, DMSO and dichloromethane.

In addition, An electron paramagnetic resonance (EPR) measurement was paformed using 2,2,6,6-tetramethyl-4-piperidone (4-oxo-TEMP) as the spin-trapping agent, which

can react with $^1O_2$ to produce 4-oxo-TEMPO as a stable nitroxide radical.[13] When the air-saturated solution containing **PD-I** and 4-oxo-TEMP was irradiated with visible light (>510 nm, 14 mW cm^{-2}) obtained by passage of xenon light through a 510 nm long path filter, the ESR spectrum of 4-oxo-TEMPO was clearly observed as a characteristic 1:1:1 triplet (Figure 12).

Moreover, to obtain the direct evidence of $^1O_2$ generation by D-π-A-π-D pyrazinium dyes, a phosphorescence spectrum of $^1O_2$ was measured in airsaturated THF solution of **PD-I**. The phosphorescence maximum of $^1O_2$ produced upon the excitation of **PD-I** at 467 nm was clearly observed at around 1270 nm (Figure 13).[14] Consequently, this work demonstrated that D-π-A-π-D pyrazinium dyes possess the ability to generate $^1O_2$ under visible light irradiation.

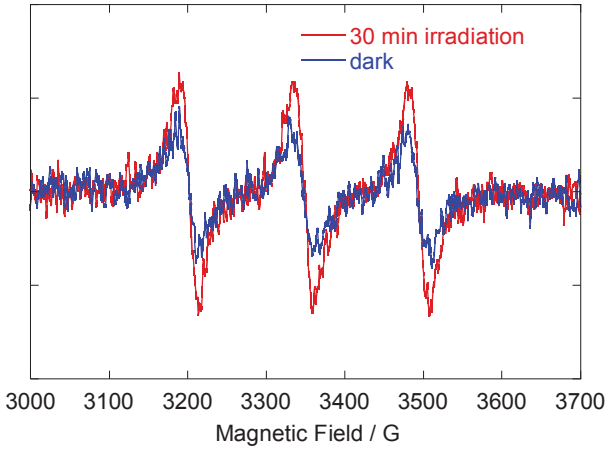

Figure 12. The ESR spectra of 4-oxo-TEMPO which is formed by the reaction of 4-oxo-TEMP with $^1O_2$ which was generated by **PD-I** under irradiation with visible light (temperature 298 K, microwave power 1 mW, microwave frequency 9.439 GHz, field modulation 0.2 mT at 100 kHz, and scan time 4 min). The air-saturated THF solution containing **PD-I** (0.01 mM) as the photosensitizer and 4-oxo-TEMP (50 mM) as the spin-trapping agent was irradiated with visible light (> 510 nm, 14 mW cm^{-2} for 30 min) obtained by passage of xenon light through a 510 nm long path filter.

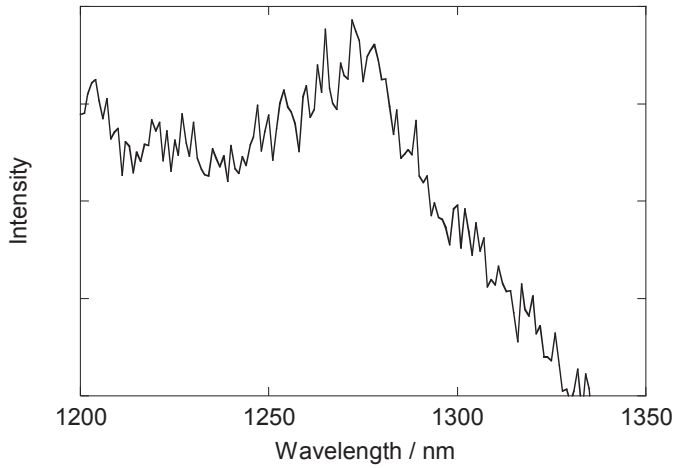

Figure 13. Phosphorescence spectrum of $^1O_2$ produced upon the excitation of **PD-I** (0.07 mM) at 467 nm in THF.

Conclusion

(D-π-)$_2$A pyrazinium dyes bearing a counter anion (X^- = Br^- or I^-) which show specific solvatochromic behavior leading to the bathochromic shift of photoabsorption band in halogenated solvents, have been designed and developed as a photosensitizer possessing singlet oxygen ($^1O_2$) generation. This work demonstrated that the (D-π-)$_2$A pyrazinium dyes possess the ability to generate $^1O_2$ under visible light irradiation, due to the effective intersystem crossing (ISC) from the singlet excited state of the photosensitizer (^{1}S*) to the triplet excited state (^{3}S*) by the heavy-atom effect of the counter anion. It was found that the $^1O_2$ quantum yield ($\Phi_\triangle$) of **PD-I** bearing I^- ion is higher than that of **PD-Br** bearing Br^- ion. Consequently, this result indicates that the high $\Phi_\triangle$ value of **PD-I** relative to **PD-Br** is attributed to the fact that I^- ion possesses superior heavy-atom effect rather than Br^- ion, resulting in the facilitation of the ISC. Moreover, it was found that THF is a favorable solvent for the (D-π-)$_2$A pyrazinium dyes to provide higher $\Phi_\triangle$ value compared with the polar solvents such as acetonitrile and DMSO. Thus, this result suggests that as for (D-π-)$_2$A pyrazinium the ISC from ^{1}S* to the ^{3}S* may be facilitated by THF, although much effort for the solvent effects on $^1O_2$ generation is necessary to ensure the hypothesis. Interestingly, the first-order rate constants (k_s) for the photooxidation of DPBF using **PD-I** in dichloromethane is greater than those in the other solvents, which is attributed to the bathochromic shift and broadening of absorption in dichloromethane, that is, the significant specific solvatochromic behavior of the (D-π-)$_2$A pyrazinium dye bearing I^- ion. Further study to gain greater insight into the effects of the molecular structure of pyrazinium dyes on the $^1O_2$ generation efficiency is now in progress by developing the (D-π-)$_2$A pyrazinium photosensitizers possessing strong photoabsorption property in body therapeutic window (650– 900 nm) and water solubility.

Acknowledgements

Chapter 2 is reproduced from "Development of a D-π-A pyrazinium photosensitizer possessing singlet oxygen generation; Y. Ooyama, T. Enoki and J. Ohshita, *RSC Adv.*, **2016**, *6*, 5428-5435." with permission from The Royal Society of Chemistry.

Reference

J. F. Lovell, T. W. B. Liu, J. Chen and G. Zheng, *Chem. Rev*., **2010**, *110*, 2839.

2 M. C. DeRosa and R. J. Crutchley, *Coord. Chem. Rev.*, **2002**, 233–234, 351.

3 M. Pawlicki, H. A. Collins, R. G. Denning and H. L. Anderson, *Angew. Chem., Int. Ed.*, **2009**, *48*, 3244.

4 K. A. Leonard, M. I. Nelen, L. T. Anderson, S. L. Gibson, R. Hilf and M. R. Detty, *J. Med. Chem*., **1999**, *42*, 3942.

5. F. Ronzani, A. Trivella, E. Arzoumanian, S. Blanc, M. Sarakha, C. Richard, E. Oliveros and S. Lecombe, *Photochem. Photobiol. Sci*., **2013**, 12, 2160.

6. (*a*) R. Schmidt and E. Afshari, *J. Phys. Chem*., **1990**, *94*, 4377; (*b*) M. Mirenda, C. A. Strassert, L. E. Dicelio and E. S. Román, *ACS Appl. Mater. Interfaces*, **2010**, *2*, 1556.

7. (*a*) R. Bonnett, *Chem. Soc. Rev.*, **1995**, *24*, 19-33; (*b*) L. Petit, A. Quartarolo, C. Adamo and Nino Russo, *J. Phys. Chem. B*, **2006**, *110*, 2398-2404; (*c*) P. C. Lo, J. D. Huang, D. Y. Y. Cheng, E. Y. M. Chan, W. P. Fong, W. H. Ko and D. K. P. Ng, *Chem. -Eur. J*., **2004**, *10*, 4831. (*d*) M. Ethirajan, Y. Chen, P. Joshi and R. K. Pandey, *Chem. Soc. Rev*., **2011**, *40*, 340.

8. (*a*) A. Kamkaew, S. H. Lim, H. B. Lee, L. V. Kiew, L. Y. Chungc and K. Burgess, *Chem. Soc. Rev*., **2013**, *42*, 77; (*b*) L. -B. Meng, W. Zhang, D. Li, Y. Li, X. -Y. Hu, L. Wang and G. Lic, *Chem. Commun.*, **2015**, *51*, 14381; (*c*) S. Erbas-Cakmak and E. U.

Akkaya, *Org. Lett*. **2014**, *16*, 2946.

9. (a) J. W. Arbogast and C. S. Foote, *J. Am. Chem. Soc*., **1991**, *113*, 8886; (*b*) A. Ikeda, T. Sato, K. Kitamura, K. Nishiguchi, Y. Sasaki, J. Kikuchi, T. Ogawa, K. Yogo and T. Takeya, *Org. Biomol. Chem.*, **2005**, 3, 2907; (*c*) J. W. Arbogast, A. P. Darmanyan, C. S. Foote, F. N. Diederich, R. L. Whetten, Y. Rubin, M. M. Alvarez and S. J. Anz, *J. Phys. Chem*., **1991**, 95, 11; (*d*) P. Mroz, G. P. Tegos, H. Gali, T. Wharton, T. Sarna and M. R. Hamblin, *Photochem. Photobiol. Sci*., **2007**, *6*, 1139.

10. (*a*) W. Wu, J. Sun, X. Cui and J. Zhao, *J. Mater. Chem. C*, **2013**, *1*, 4577; (*b*) R. Gao, D. G. Ho, B. Hernandez, M. Selke, D. Murphy, P. I. Djurovich and M. E. Thompson, *J. Am. Chem. Soc.*, **2002**, *124*, 14828; (*c*) S. Takizawa, R. Aboshi and S. Murata, *Photochem. Photobiol. Sci.*, **2011**, 10, 895; (*d*) P. I. Djurovich, D. Murphy, M. E. Thompson, B. Hernandez, R. Gao, P. L. Hunt and M. Selke, *Dalton Trans*., **2007**, 3763.

11. (*a*) J. C. Koziar and D. O. Cowan, *Acc. Chem. Res.*, **1978**, *11*, 334; (*b*) C. Schweitzer and R. Schmidt, *Chem. Rev*., **2003**, 103, 1685.

12. (*a*) F. Ronzani, E. Arzoumanian, S. Blanc, P. Bordat, T. Pigot, C. Cugnet, E. Oliveros, M. Sarakha, C. Richard and S. Lacombe, *Phys. Chem. Chem. Phys.*, **2013**, *15*, 17219; (*b*) S. Cobo, F. Lafolet, E. Saint-Aman, C. Philouze, C. Bucher, S. Silvi, A. Credi and G. Royal, *Chem. Commun.*, **2015**, 51, 13886; (*c*) J. Ohshita, Y. Hayashi, K. Murakami, T. Enoki and Y. Ooyama, *Dalton Trans*., **2016**, *45*, 15679; (*d*) J. Ohshita, Y. Hayashi, Y. Adachi, T. Enoki, K. Yamaji, and Y. Ooyama, *ChemistrySelect*, **2018**, *3*, 8604.

13. (*a*) Y. Yamakoshi, N. Umezawa, A. Ryu, K. Arakane, N. Miyata, Y. Goda, T. Masumizu and T. Nagano, *J. Am. Chem. Soc*., **2003**, *125*, 12803; (*b*) S. Oriana, S. Aroua, J. O. B. Söllner, X.-J. Ma, Y. Iwamoto and Y. Yamakoshi, *Chem. Commun*., **2013**, *49*, 9302.

14. (*a*) Y. Yamakoshi, N. Umezawa, A. Ryu, K. Arakane, N. Miyata, Y. Goda, T. Masumizu and T. Nagano, *J. Am. Chem. Soc*., **2003**, *125*, 12803; (*b*) H. Horiuchi, T. Kameya, M. Hosaka, K. Yoshimura, S. Kyushin, H. Matsumoto, T. Okutsu, T. Takeuchi and H. Hiratsuka, *J. Photochem. Photobiol. A*, **2011**, *221*, 98; (*c*) K. Hirakawa, N. Fukunaga, Y. Nishimura, T. Arai and S. Okazaki, *Bioorg. Med. Chem. Lett*., **2013**, *23*, 2704.

Chapter 3

Singlet oxygen generation properties of an inclusion complex of cyclic free-base porphyrin dimer and fullerene C_{60}

Introduction

The porphyrin dyes are well known as a photosensitizer for PDT due to their high ability for singlet oxygen ($^1O_2$) generation and high photostability. In order to further improve the quantum yields of singlet oxygen generation ($\Phi_\triangle$) value, much effort in molecular design and development of porphyrin photosensitizers have been made.[1] Recent years, porphyrin-C_{60} dyads as well as boron dipyrromethene (BODIPY)-C_{60} dyads have been reported as promising photosensitizers for PDT.[2,3] These dyes exhibit a higher $\Phi_\triangle$ value than each porphyrin or C_{60}, which is attributed to the formation of long-lived triplet excited state ($^3S^*$) by the effective ISC due to intramolecular energy transfer or electron transfer (charge separation) between porphyrin or BODIPY moiety and C_{60}.

Recently, Tani et al. have designed and developed the cyclic free-base porphyrin dimer **CPD** linked by butadiyne bearing four 4-pyridyl groups and its inclusion complex **C_{60} ⊂ CPD** with C_{60} (Figure 1).[4] It was expected that **C_{60} ⊂ CPD** has favorable photochemical and electrochemical properties for PDT through the electrochemical measurements and the transient absorption spectroscopy, based on the fact that the singlet excited state **C_{60}⊂(CPD)*** undergoes intrasupramolecular electron transfer to form a completely charge-separated state **$C_{60}^{\cdot-}$-CPD$^{\cdot+}$**. Thus, in this work, to gain insight into the $^1O_2$ generation properties of supramolecular complex of cyclic free-base porphyrin dimer with C_{60}, the author evaluated the $\Phi_\triangle$ and rate constant (k_s) of $^1O_2$ generation for

CPD and **C_{60}⊂CPD**.

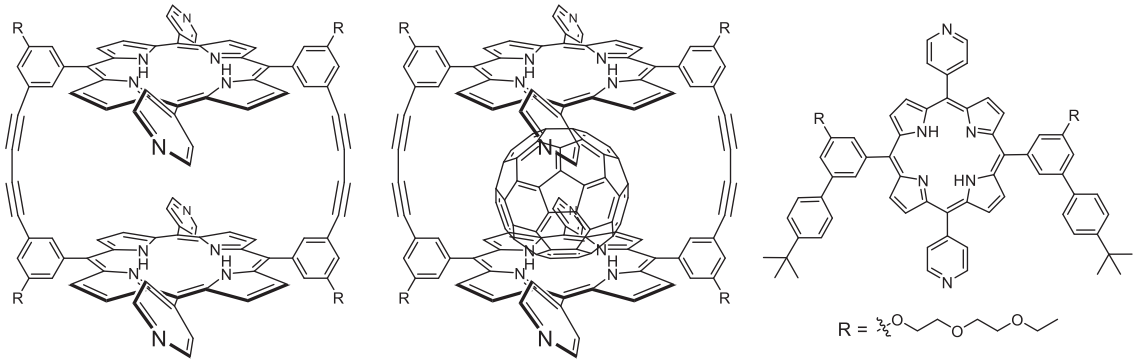

Figure 1. Chemical structures of cyclic free-base porphyrin dimer (**CPD**) linked by butadiyne bearing four 4-pyridyl groups, inclusion complex (**C_{60}⊂CPD**) and ABAB porphyrin dye **H2PyP**.

Experimental

Evaluation of $^1O_2$ quantum yield

Quantum yield ($\Phi_\triangle$) for singlet oxygen ($^1O_2$) generation by cyclic free-base porphyrin dimer CPD, its inclusion complex **C_{60} ⊂ CPD** with fullerene C_{60} and **H2PyP** in CH_2Cl_2/MeOH (=1/1, v/v) was evaluated by the same method as that in Chapter 2. Concentration of **CPD**, **C_{60}⊂CPD** or **H2PyP** was adjusted with an absorbance of ca. 0.03 at the irradiation wavelength (509 nm). The air-saturated solution containing the photosensitizer (**CPD**, **C_{60}⊂CPD** or **H2PyP**) and DPBF was irradiated with 509 nm (300 mW cm^{-2}) obtained by passage of xenon light through monochromator. The photoabsorption spectral change of DPBF with the photoirradiation was monitored with an interval of 1 min up to 10 min. The absorption band of DPBF at around 410 nm decreased with the increase in the photoirradiation time. The changes in optical density (ΔOD) of DPBF are plotted against the photoirradiation time, and the slope is used to estimate the $\Phi_\triangle$ values of **CPD**, **C_{60} ⊂ CPD** and **H2PyP**. The $\Phi_\triangle$ values of **CPD**, **C_{60}⊂CPD** and **H2PyP** were estimated by the relative method using Rose Bengal (RB) ($\Phi_\triangle$ = 0.80) in methanol as the standard.

Photosensitizing ability

Photosensitizing ability of **CPD**, **C_{60}⊂CPD** and **H2PyP** in CH_2Cl_2/MeOH was evaluated by plotting the $\ln(C_t/C_0)$ against the photoirradiation time, where C_t is a concentration of 1,5-dihydroxynaphthalene (DHN) at the reaction time (t) and C_0 is the initial concentration of DHN before photoirradiation. CH_2Cl_2/MeOH was bubbled with air for 15 min. The air saturated solution containing the photosensitizer (2.5×10^{-6} M for **CPD** and **C_{60}⊂CPD**, 5.0×10^{-6} M for **H2PyP** and 2.5×10^{-6} M for RB) and DHN (1.0×10^{-4} M) was irradiated with visible light (>385 nm, 30 mW cm^{-2}) obtained by passage of xenon

light through a 385 nm long path filter. The photooxidation of DHN with the photoirradiation was monitored by following the decrease in the photoabsorption at around 300 nm with an interval of 1 min up to 10 min and then an interval of 5 min up to 30 min. The concentration (C_t) of DHN at the reaction time (t) was calculated based on Lambert–Beer law ($A_{DHN} = \varepsilon cl$). The $\ln(C_t/C_0)$ decreased almost linearly with the increase in the photoirradiation time due to the photooxidation of DHN, that is, the slope was used to estimate the rate constants (k_s).

$^1O_2$ detection by EPR spin-trapping method with 4-oxo-TEMP

The EPR spectra were recorded on a JEOL JES-RE1X spectrometer under the following experimental conditions: temperature 298 K, microwave power 1 mW, microwave frequency 9.439 GHz, and field modulation 0.2 mT at 100 kHz. The air-saturated CH_2Cl_2 solution containing **CPD** (2.5×10^{-6} M M), **C_{60}⊂CPD** (2.5×10^{-6} M) or **H2PyP** (5.0×10^{-6} M) as the photosensitizer and 4-oxo-TEMP (50 mM) as the spin-trapping agent was irradiated with visible light (>385 nm, 30 mW cm^{-2} for 1 h) obtained by passage of xenon light through a 385 nm long path filter. The ESR spectrum of 4-oxo-TEMPO which is formed by the reaction of 4-oxo-TEMP with $^1O_2$, was clearly observed as a characteristic 1 : 1 : 1 triplet (Figure. 7).

Results and Discussion

The free-base porphyrin dimer **CPD** in CH_2Cl_2/MeOH exhibits strong Soret band at around 420 nm and relatively weak Q band in the range 500–650 nm (Figure 2, λ_{abs} / nm (ε / M^{-1} cm^{-1}) = 416 (708000), 514 (31200), 548 (7400), 587 (9000), 642 (2900)). The molar extinction coefficients (ε) of Soret and Q bands for **CPD** are higher than those of **H2PyP** (λ_{abs} / nm (ε / M^{-1} cm^{-1}) = 418 (419000), 513 (19200), 548 (6200), 588 (6000), 643 (3000)) as an ABAB porphyrin monomer with two pyridyl and two phenyl groups. For the C_{60} inclusion complex **C_{60}⊂CPD**, it is difficult to estimate the exact absorption spectra because the 1 : 1 complex of **CPD** with C_{60} is in dissociation equilibrium in solution of 10^{-5} to 10^{-6} M concentration which is suitable for the measurement of photoabsorption spectra of porphyrin dyes. However, it was demonstrated that upon addition of C_{60} to the solution of the cyclic porphyrin dimer, its Soret band showed red-shift with decrease in intensity, whereas its Q band was slightly redshifted but increased in intensity.[4]

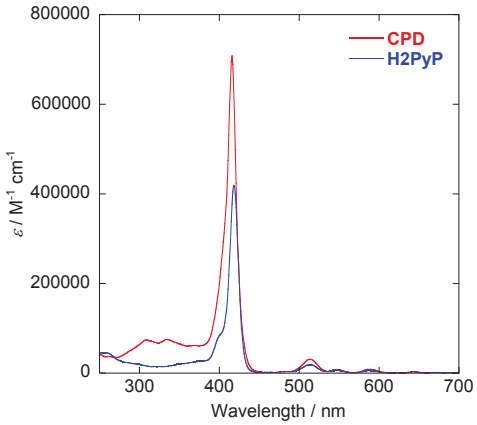

Figure 2. UV-Vis absorption spectra of **CPD** and **H2PyP**

$^1O_2$ generation by **CPD**, **C60⊂CPD** or **H2PyP** in CH_2Cl_2/MeOH (= 1/1, v/v) was evaluated by monitoring the photoabsorption spectral change of the $^1O_2$ scavenger 1,3-diphenylisobenzofuran (DPBF) accompanied by the reaction of DPBF with the generated $^1O_2$, that is, DPBF can detect and quantify $^1O_2$ through its photooxidation. CH_2Cl_2/MeOH was bubbled with air for 15 min. The air-saturated solution containing **CPD**, **C60⊂CPD** or **H2PyP** and DPBF was irradiated with 509 nm obtained by passage of xenon light through monochromator. For **CPD**, **C60⊂CPD** and **H2PyP**, the absorption band of DPBF at around 410 nm decreased with the increase in the photoirradiation time (Figure 3a-c), which indicate the reaction of DPBF with $^1O_2$ generated upon the photoexcitation of the porphyrin dyes. To gain insight into the effect of the cyclic porphyrin dimers on the efficiency of DPBF photooxidation, the changes in optical density (ΔOD) of DPBF were plotted against the photoirradiation time (Figure. 3d), and the slope (m_s) is used to estimate the Φ_Δ value for **CPD**, **C60⊂CPD** and **H2PyP**. The m_s value of **H2PyP** (-1.5×10^{-2}) is larger than those of **CPD** (-1.2×10^{-2}) and **C60⊂CPD** (-9.8×10^{-3}). Moreover, it was revealed that the m_s value of **CPD** is larger than that of **C60⊂CPD**. Thus, the Φ_Δ values of **CPD**, **C60⊂CPD** and **H2PyP** were estimated by the relative method using Rose Bengal (RB) in methanol as the standard (Table 1). The Φ_Δ value of **CPD**, **C60⊂CPD** and **H2PyP** is 0.62, 0.52 and 0.91 respectively, which is in good agreement with the m_s value.

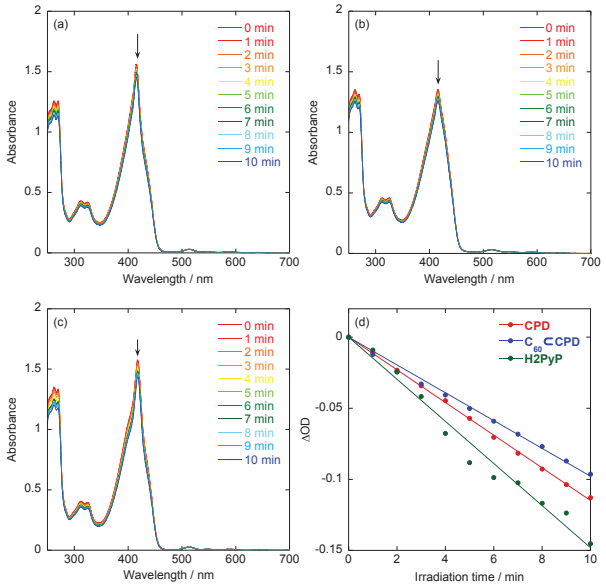

Figure 3. Photoabsorption spectral changes for the photooxidation of DPBF using (a) **CPD** (1.3×10^{-6} M), (b) **C$_{60}$⊂CPD** (1.0×10^{-6} M) and (c) **H2PyP** (1.4×10^{-6} M) as photosensitizer under photoirradiation with 509 nm (300 mW cm^{-2}) in CH_2Cl_2/MeOH (= 1/1, v/v).

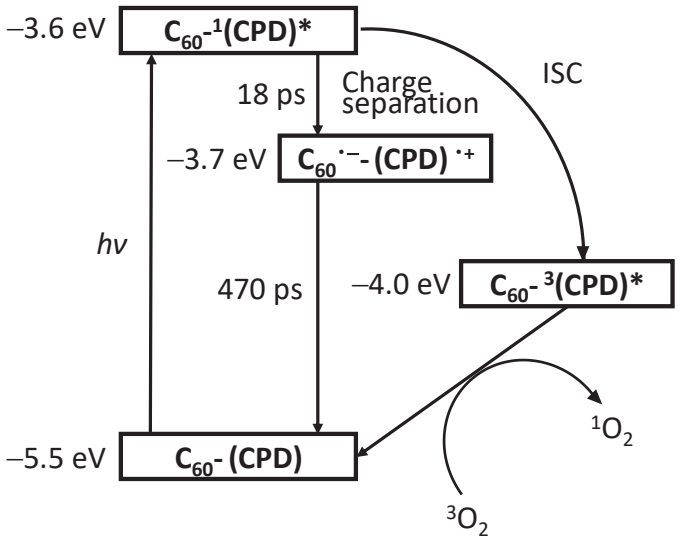

Figure 4. The photodynamics of **C$_{60}$⊂CPD** and $^1O_2$ generation.

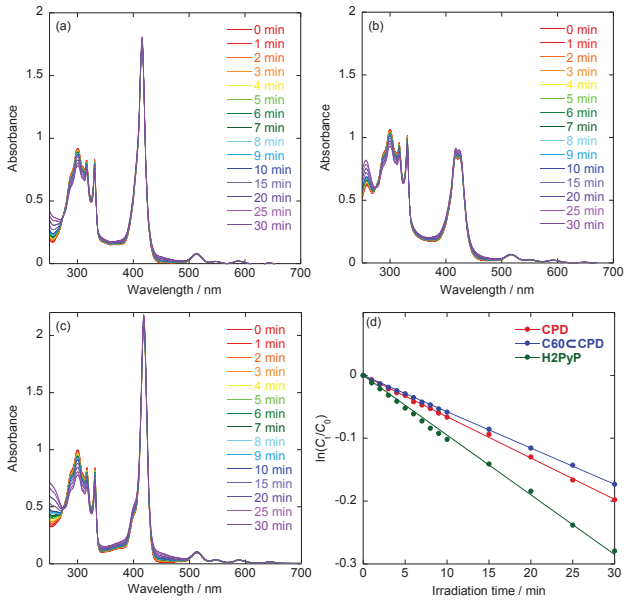

Figure 5. Photoabsorption spectral changes for the photooxidation of DHN (1.0×10^{-4} M) using (a) **CPD** (2.5×10^{-6} M), (b) **C$_{60}$⊂CPD** (2.5×10^{-6} M) and (c) **H2PyP** (5.0×10^{-6} M) as photosensitizer under photoirradiation with visible light (>385 nm, 30 mW cm^{-2}) in CH_2Cl_2/ MeOH (= 1/1, v/v). (d)

Table 1. $^1O_2$ quantum yield (Φ_Δ) and first-order rate constant (k_s) for the photooxidation of DPBF and DHN in CH_2Cl_2/MeOH (= 1/1, v/v), respectively, using **CPD**, **C$_{60}$⊂CPD** or **H$_2$PyP** as photosensitizer.

Photosensitizer	Φ_Δ [a]	k_s / min^{-1} [b]
CPD	0.62	6.6×10^{-3}
C$_{60}$⊂CPD	0.52	5.8×10^{-3}
H2PyP	0.91	9.5×10^{-3}

[a] $^1O_2$ quantum yield (relative decomposition rate of DPBF), with Rose Bengal (**RB**) as standard (Φ_Δ = 0.80 in methanol) and diphenylisobenzofuran (DPBF) as $^1O_2$ scavenger. [b] First-order rate constant for the reaction of DHN with $^1O_2$ generated upon photoexcitation of the photosensitizer.

This result suggests that the ABAB porphyrin monomer **H2PyP** would possess higher ISC efficiency from $^1S^*$ to the $^3S^*$ than in the cyclic free-base porphyrin dimer **CPD**. Moreover, it is worth mentioning that the Φ_Δ value of **C$_{60}$⊂CPD** is lower than that of **CPD**. In the previous work, it was demonstrates that the decay of photoexcited state of **C$_{60}$⊂CPD** has two steps (Figure 4): the first step has a lifetime of 18 ps, which corresponds to the disappearance of the singlet excited state of **C$_{60}$⊂CPD*** (ca. –3.6 eV),

that is, **C_{60}-^{1}(CPD)*** undergoes intrasupramolecular electron transfer to give a charge-separated state **$C_{60}^{\cdot-}$CPD$^{\cdot+}$** (ca. –3.7 eV).[4] **$C_{60}^{\cdot-}$-CPD$^{\cdot+}$** decays with a lifetime of 470 ps to the ground state. The singlet excited state **C_{60}-^{1}(CPD)*** has a slower ISC to the triplet excited state **C_{60}-^{3}(CPD)*** (ca. –4.0 eV), in addition, the **C_{60}-^{3}(CPD)*** would undergo energy transfer to C_{60}, leading to the formation of **$^3C_{60}$*-(CPD)**. Thus, on the basis of the photodynamics of the cyclic free-base porphyrin dimer and its inclusion complex with C_{60}, the inferior Φ_Δ value of the C_{60} inclusion complex would be attributed to the formation of charge-separated state. The formation of charge-separated state lead to low ISC efficiency because the ISC is in kinetically competition with the intrasupramolecular electron transfer, that is, the formation of triplet excited state **^{3}(CPD)*** is in kinetically unfavorable compared with that of the charge-separated state **$C_{60}^{\cdot-}$-CPD$^{\cdot+}$**. In order to evaluate the photosensitizing ability of the cyclic free-base porphyrin dimer and its inclusion complex with C_{60}, the $\ln(C_t/C_0)$ is plotted against the photoirradiation time, where C_t is a concentration of 1,5-dihydroxynaphthalene (DHN) at the reaction time (t) and C_0 is the initial concentration of DHN before photoirradiation. CH_2Cl_2/MeOH (= 1/1, v/v) were bubbled with air for 15 min. The air-saturated solution containing **CPD** or **C_{60} ⊂CPD** and DHN was irradiated with visible light (>385 nm, 30 mW cm^{-2}) obtained by passage of xenon light through a 385 nm long path filter. The photoabsorption spectral changes for the photooxidation of DHN using **CPD**, **C_{60} ⊂ CPD** or **H2PyP** under photoirradiation with the visible light in CH_2Cl_2/MeOH (= 1/1, v/v) are shown in Figure 5. The absorption band of DHN at around 300 nm decreased with the increase in the photoirradiation time. For **CPD**, **C_{60}⊂CPD** and **H2PyP**, the plots of $\ln(C_t/C_0)$ against the photoirradiation time indicate that the $\ln(C_t/C_0)$ linearly decreased with the increase in the photoirradiation time (Figure 5d). Thus, this result indicates the $\ln(C_t/C_0)$ bears a linear

relationship with the photoirradiation time to provide the first-order rate constants (k_s) for the photooxidation of DHN using the cyclic free-base porphyrin dimer or its inclusion complex with C_{60} as the photosensitizer (Table 1). Obviously, the higher k_s values of the cyclic free-base porphyrin dimer and its inclusion complex with C_{60} relative to RB are due to the contribution of the strong Soret band of the cyclic free-base porphyrin skeleton, although the k_s values of **CPD** and **C_{60}⊂CPD** are lower than that of **H2PyP** (9.5×10^{-3} min^{-1}). It is worth noting here that the k_s value (6.6×10^{-3} min^{-1}) of **CPD** is greater than that (5.8×10^{-3} min^{-1}) of **C_{60}⊂CPD**. Therefore, this result demonstrates that **CPD** exhibits more efficient photosensitizing ability due to the effective ISC compared to **C_{60}⊂CPD**.

In addition, we performed an electron paramagnetic resonance (EPR) method with 2,2,6,6-tetramethyl-4-piperidone (4-oxo-TEMP) as the spin-trapping agent, which can react with $^1O_2$ to produce 4-oxo-TEMPO as a stable nitroxide radical. When the air-saturated solution containing **CPD**, **C_{60} ⊂ CPD** or **H2PyP** and 4-oxo-TEMP was irradiated with visible light (>385 nm, 30 $mWcm^{-2}$) obtained by passage of xenon light through a 385 nm long path filter, for both the free-base porphyrin dimer and its inclusion complex with C_{60} as well as **H2PyP** the ESR spectra of 4-oxo-TEMPO were clearly observed as a characteristic 1 : 1 : 1 triplet (Figure 7). Consequently, this work demonstrated that the cyclic free-base porphyrin dimer and its inclusion complex with C_{60} possess the ability to generate $^1O_2$ under visible light irradiation.

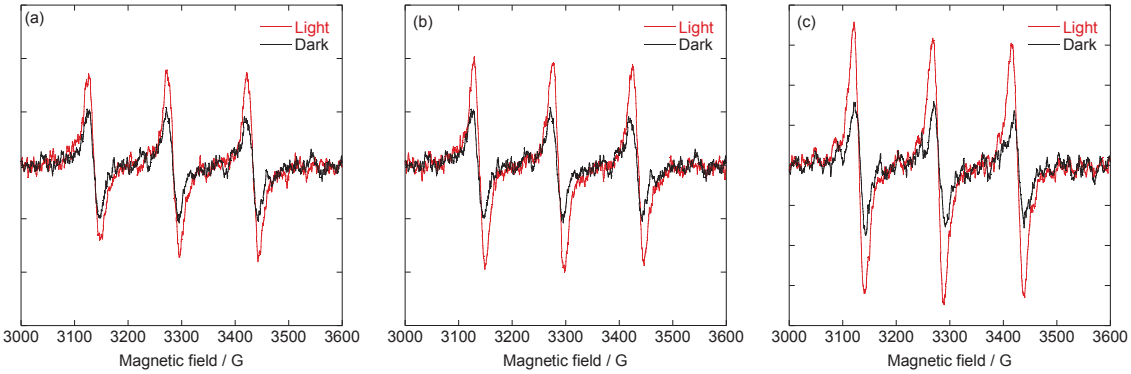

Figure 7. The ESR spectra of 4-oxo-TEMPO which is produced by the reaction of 4-oxo-TEMP with $^1O_2$ which was generated by (a) **CPD**, (b) **C_{60}⊂CPD** and (c) **H2PyP** under irradiation with visible light (temperature 298 K, microwave power 1 mW, microwave frequency 9.439 GHz, and field modulation 0.2 mT at 100 kHz). The air-saturated CH_2Cl_2 solution containing **CPD** (2.5×10^{-6} M), **C_{60}⊂CPD** (2.5×10^{-6} M) or **H2PyP** (5.0×10^{-6} M) as the photosensitizer and 4-oxo-TEMP (50 mM) was irradiated with visible light (>385 nm, 30 mW cm^{-2} for 1 h) obtained by passage of xenon light through a 385 nm long path filter.

Conclusion

To investigate singlet oxygen ($^1O_2$) generation properties of cyclic porphyrin dimer and its inclusion complex with fullerene C_{60}, the $^1O_2$ quantum yield ($\Phi_\triangle$) and rate constant (k_s) of $^1O_2$ generation for cyclic free-base porphyrin dimer **CPD** and its inclusion complex **C_{60}⊂CPD** with C_{60} have been evaluated. It was found that the $\Phi_\triangle$ value of **C_{60}⊂CPD** is lower than that of **CPD**. The lower $\Phi_\triangle$ value of the C_{60} inclusion complex would be attributed to the formation of charge-separated state **$C_{60}^{\cdot -}$-CPD$^{\cdot +}$**, leading to low intersystem crossing (ISC) efficiency for the formation of triplet excited state **^{3}(CPD)***, although it was expected that the formation of **$C_{60}^{\cdot -}$-CPD$^{\cdot +}$** is favorable for $^1O_2$ generation. In Chapter 3, it is demonstrated that the cyclic free-base porphyrin dimer and its supramolecular complex with C_{60} possess the ability to generate $^1O_2$ under visible light irradiation.

Acknowledgements

Chapter 3 is reproduced from "Singlet oxygen generation properties of an inclusion complex of cyclic free-base porphyrin dimer and fullerene C_{60}; Y. Ooyama, T. Enoki, J. Ohshita, T. Kamimura, S. Ozako, T. Koide and F. Tani, *RSC Adv.*, **2017**, *7*, 18690-18695." with permission from The Royal Society of Chemistry.

Reference

1. (*a*) L. Delanaye, M. A. Bahri, F. Tfibel, M.-P. Fontaine-Aupart, A. Mouithys-Mickalad, B. Heine, J. Piette and M. Hoebeke, *Photochem. Photobiol. Sci*., **2006**, *5*, 317; (*b*) M. Khurana, H. A. Collins, A. Karotki, H. L. Anderson, D. T. Cramb and B. C. Wilson, *Photochem. Photobiol.*, **2007**, *84*, 1441; (*c*) A. P. Thomas, P. S. S. Babu, S. A. Nair, S. Ramakrishnan, D. Ramaiah, T. K. Chandrashekar, A. Srinivasan and M. R. Pillai, *J. Med. Chem*., **2012**, *55*, 5110; (*d*) K. Hirakawa, Y. Nishimura, T. Arai and S. Okazaki, *J. Phys. Chem. B*, **2013**, *117*, 13490; (*e*) H. Horiuchi, M. Hosaka, H. Mashio, M. Terata, S. Ishida, S. Kyushin, T. Okutsu, T. Takeuchi and H. Hiratsuka, *Chem.-Eur. J*., **2014**, *20*, 6054.

2. M. E. Milanesio, M. G. Alvarez, V. Rivarola, J. J. Silber and E. N. Durantini, *Photochem. Photobiol*., **2005**, *81*, 891.

3. (*a*) L. Huang, X. Yu, W. Wu and J. Zhao, *Org. Lett*., **2012**, *14*, 2594; (*b*) A. Kamkaew, S. H. Lim, H. B. Lee, L. V. Kiew, L. Y. Chung and K. Burgess, *Chem. Soc. Rev*., **2013**, *42*, 77; (*c*) L. Huang, X. Cui, B. Therrien and J. Zhao, *Chem.-Eur. J*., **2013**, *19*, 17472; (*d*) S. Guo, L. Xu, K. Xu, J. Zhao, B. Küçtenüköz, A. Karatay, H. G. Yaglioglu, M. Hayvalid and A. Elmali, *Chem. Sci*., **2015**, *6*, 3724.

4. (*a*) H. Nobukuni, Y. Shimazaki, H. Uno, Y. Naruta, K. Okubo, T. Kojima, S. Fukuzumi, S. Seki, H. Sakai, T. Hasobe and F. Tani, *Chem. -Eur. J*., **2010**, *16*, 11611; (*b*) H.

Nobukuni, T. Kamimura, H. Uno, Y. Shimazaki, Y. Naruta and F. Tani, *Bull. Chem. Soc. Jpn*., **2012**, *85*, 862; (*c*) K. Sakaguchi, T. Kamimura, H. Uno, S. Mori, S. Ozako, H. Nobukuni, M. Ishida and F. Tani, *J. Org. Chem*., **2014**, *79*, 2980; (*d*) T. Kamimura, K. Ohkubo, Y. Kawashima, H. Nobukuni, Y. Naruta, F. Tani and S. Fukuzumi, *Chem. Sci*., **2013**, *4*, 1451; (*e*) T. Kamimura, K. Ohkubo, Y. Kawashima, S. Ozako, K. Sakaguchi, S. Fukuzumi and F. Tani, *J. Phys. Chem. C*, **2015**, 119, 25634; (*f*) Y. Ooyama, K. Uenaka, T. Kamimura, S. Ozako, M. Kanda, T. Koide and F. Tani, *RSC Adv*., **2016**, *6*, 16150.

Chapter 4

Synthesis and optical and electrochemical properties of julolidine-structured pyrido[3,4-*b*]indole dye

Introduction

The D-A (D-π-A) dyes attracted considerable attention in both fundamental and applied chemistry due to their intense photoabsorption and fluorescence properties originating from ICT excitation from electron-donating to electron-accepting component. For the D-A dyes used as sensors for detecting cations, anions and neutral organic species, the electronic structure of the D-A dye is changed by the intermolecular interaction (electrostatic interaction) between the dye and the analyte, resulting in changes in the photoabsorption, fluorescence (intensity and wavelength) and electrochemical properties (oxidation and reduction potentials).[1-4] In particular, 9H-pyrido[3,4-*b*]indole (*β*-carboline) (Figure 1), which contains a pyridine ring as a hydrogen bond acceptor, is one of the most promising colorimetric and fluorescent sensor skeletons for hydrogen bond donor species such as Brønsted acids, water, alcohols and nucleotides.[5,6] However, there are a few reports on the development of *β*-carboline derivatives with a strong electron-donating substituent such as an amino group. Thus, in this work, to develop *β*-carboline derivatives with a strong electron-donating group and to investigate the photophysical and electrochemical properties, the julolidine-structured *β*-carboline dye **ET-1** has been developed as a small D-A fluorescent dye (Figure 1). **ET-1** showed bathochromic shifts of the fluorescence band upon changing from aprotic solvents to protic solvents, as well as positive fluorescence solvatochromism. Moreover, it was found

that the D-A dye **ET-1** can form a 1 : 1 Py(N)–B complex with boron trifluoride (BF_3) and a Py(N)–hydrogen-bonded proton transfer (Py(N)–H) complex with trifluoroacetic acid (CF_3COOH), which exhibit photoabsorption and fluorescence bands at a longer wavelength region than those of the pristine **ET-1**. Herein, the author report that **ET-1** is a small D-A-type colorimetric and fluorescent sensor for Brønsted and Lewis acids.

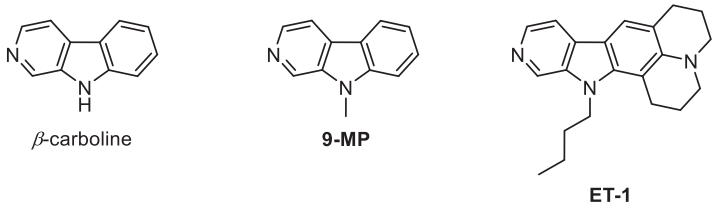

Figure 1. Chemical structures of *β*-carboline (9H-pyrido[3,4-*b*]indole), **9-MP** and **ET-1**.

Experimental

General

Melting points were measured using a Yanaco micro melting point apparatus MP model. IR spectra were recorded on a SHIMADZU IRAffinity-1 spectrometer using the ATR method. High-resolution mass spectral data were acquired using a Thermo Fisher Scientific LTQ Orbitrap XL. ^{1}H NMR and ^{13}C NMR spectra were recorded using a Varian-400 (400 MHz) or a Varian-400 (500 MHz) FT NMR spectrometer. Absorption spectra were recorded using a HITACH U-2910 spectrophotometer and fluorescence spectra were recorded using a HORIBA FluoroMax-4 spectrofluorometer. The fluorescence quantum yields were determined using a HORIBA FluoroMax-4 spectrofluorometer with a calibrated integrating sphere system. Cyclic voltammetry (CV) were recorded in acetonitrile/Bu_4NClO_4 (0.1 M) solution with a three-electrode system consisting of Ag/Ag^+ as the reference electrode, a Pt plate as the working electrode, and a Pt wire as the counter electrode using an Electrochemical Measurement System HZ-7000 (HOKUTO DENKO).

Synthesis

9-(Trimethylstannyl)julolidine (1). To an Et_2O/THF solution (160 mL/60 mL) of 9-bromojulolidine (8.7 g, 0.035 mol) under argon atmosphere a 1.6 M hexane solution of *n*BuLi (34 mL, 0.055 mol) was added at −80°C and stirred for 4h. Me_3SnCl (11 g, 0.055 mol) was added to the solution, and then the solution was stirred for 12 h at room temperature. The reaction was quenched with water, and then the solution was extracted with ether. The ether extracts were evaporated under reduced pressure to give **1** (9.6 g, yield 82%) as a yellow oil; IR (ATR): $\tilde{\nu}$ = 1583, 1491, 1460, 1308 cm^{-1}; ^{1}H NMR (400 MHz, $CDCl_3$) δ = 0.11 (s, 9H), 1.84-1.89 (m, 4H), 2.65 (t, J = 5.1 Hz, 4H), 3.03 (t, J =

4.6 Hz, 4H), 6.78 (s, 2H) ppm; ^{13}C NMR (125 MHz, $CDCl_3$) δ = –9.38, 22.19, 27.71, 50.09, 121.61, 125.89, 134.61, 143.47 ppm; HRMS (ESI): m/z (%): [M + H+] calcd for $C_{15}H_{24}NSn$, 338.09252; found 338.09320.

9-(3-Nitropyridin-4-yl)-julolidine (2). A solution of **1** (0.3 g, 0.89 mmol), 4-chloro-3-nitropyridine (0.14 g, 0.89 mmol) and $Pd(PPh_3)_4$ (0.052 g, 0.045 mmol) in toluene (5 mL) was stirred for 16 h at 110°C under argon atmosphere. The reaction mixture was diluted with water and then the solution was extracted with dichloromethane. The dichloromethane extracts were evaporated under reduced pressure. The residue was chromatographed on silica gel (dichloromethane as the eluent) to give **2** (0.081 g, yield 31%) as a red solid; m.p. 93–95 °C; IR (ATR): $\tilde{\nu}$ = 1589, 1520, 1307 cm^{-1}; ^{1}H NMR (400 MHz, $CDCl_3$) δ = 1.95-2.01 (m, 4H), 2.76 (t, J = 6.4 Hz, 4H), 3.23 (t, J = 5.7 Hz, 4H), 6.80 (s, 2H), 7.36 (d, J = 5.2 Hz, 1H), 8.62 (d, J = 5.2 Hz, 1H), 8.87 (s, 1H) ppm; ^{13}C NMR (125 MHz, $CDCl_3$) δ = 21.64, 27.82, 49.95, 119.68, 121.73, 125.03, 126.59, 143.87, 144.44, 145.21, 145.60, 152.04 ppm; HRMS (APCI): m/z (%): [M + H+] calcd for $C_{17}H_{18}N_3O_2$, 296.13935; found 296.13940.

2,3,5,6,7,13-Hexahydro-1H-pyrido[3,2,1-*ij*]pyrido[4',3':4,5]-pyrrolo[2,3-*f*]quinoline (3). A solution of **2** (0.26 g, 0.88 mmol) and PPh_3 (0.9 g, 3.4 mmol) in *o*-dichlorobenzene (5 mL) was stirred for 5 days at 150°C under argon atmosphere. After concentrating under reduced pressure, the resulting residue was dissolved in dichloromethane. The dichloromethane extract was evaporated under reduced pressure. The residue was chromatographed on silica gel (ethyl acetate and then ethanol as the eluent) and then reverse-phase silica gel (methanol as the eluent) to give **3** (0.058 g, yield 25%) as a yellow powder; m.p. 232–234°C; IR (ATR): $\tilde{\nu}$ = 3144, 1624, 1439 cm^{-1}; ^{1}H NMR (500MHz, CD_2Cl_2) δ = 1.99-2.04 (m, 2H), 2.09-2.14 (m, 2H), 2.87 (t, J = 6.5 Hz, 2H), 2.92 (t, J =

6.5 Hz, 2H), 3.22-3.26 (m, 4H), 7.49 (s, 1H), 7.68 (d, J = 5.2 Hz, 1H), 8.87 (br s, N-H), 8.25 (d, J = 5.2 Hz, 1H), 8.69 (s, 1H) ppm; ^{13}C NMR (125 MHz, CD_2Cl_2) δ = 21.82, 22.68, 22.80, 28.79, 50.25, 50.89, 101.98, 110.08, 113.32, 117.44, 119.22, 130.37, 132.73, 136.35, 139.44, 140.21, 144.27 ppm; HRMS (ESI): m/z (%): [M + H+] calcd for $C_{17}H_{18}N_3$, 264.14952; found 264.14951.

13-butyl-2,3,5,6,7,13-Hexahydro-1H-pyrido[3,2,1-*ij*]pyrido[4',3':4,5]-pyrrolo[2,3-*f*]quinoline (ET-1). A solution of **3** (0.05 g, 0.19 mmol) in DMF (4 mL) was treated with sodium hydride (4.6 mg, 0.19 mmol) and stirred for 1 h at room temperature. 1-Iodobutane (0.035 g, 0.19 mmol) in DMF (8 mL) was added dropwise and the solution was stirred at room temperature for 3 h. The reaction was quenched with water, and then the solution was extracted with dichloromethane. The dichloromethane extracts were evaporated under reduced pressure. The residue was chromatographed on reverse-phase silica gel (methanol as the eluent) to give **ET-1** (0.021 g, yield 35%) as a yellow powder; m.p. 108-109°C; IR (ATR): $\tilde{\nu}$ = 1618, 1445, 1327 cm^{-1}; ^{1}H NMR (500 MHz, CD_2Cl_2) δ = 0.95 (t, J = 7.4 Hz, 3H), 1.35-1.42 (m, 2H), 1.74-1.80 (m, 2H), 1.96-2.01 (m, 2H), 2.04-2.09 (m, 2H), 2.89 (t, J = 6.5 Hz, 2H), 3.21 (t, J = 6.5 Hz, 2H), 3.25 (t, J = 5.8 Hz, 2H), 4.43 (t, J = 7.8 Hz, 2H), 7.49 (s, 1H), 7.65 (d, J = 5.2 Hz, 1H), 8.21 (d, J = 5.2 Hz, 1H), 8.62 (s, 1H) ppm; ^{13}C NMR (125 MHz, CD_2Cl_2) δ = 14.03, 20.57, 22.33, 22.78, 24.46, 29.02, 33.17, 45.92, 50.12, 51.46, 103.42, 112.10, 112.57, 117.68, 119.39, 129.78, 131.34, 138.15, 138.97, 140.60, 144.99 ppm; HRMS (ESI): m/z (%): [M + H+] calcd for $C_{21}H_{26}N_3$, 320.21212; found 320.21262.

Results and discussion

The julolidine-structured pyrido[3,4-*b*]indole derivative **ET-1** studied in this work was synthesized according to a stepwise synthetic protocol (Scheme 1). The starting material, 4-bromojulolidine, was converted to stannyl compound **1** through treatment with *n*BuLi and then Me_3SnCl. Compound **2** was prepared through the Stille coupling of **1** with 4-chloro-3-nitropyridine. Cadogan reductive cyclization of **2** gave the julolidine-structured 9*H*-pyrido[3,4-*b*]indole **3**. Then, **ET-1** was obtained via the reaction of **3** with 1-iodobutane using sodium hydride.

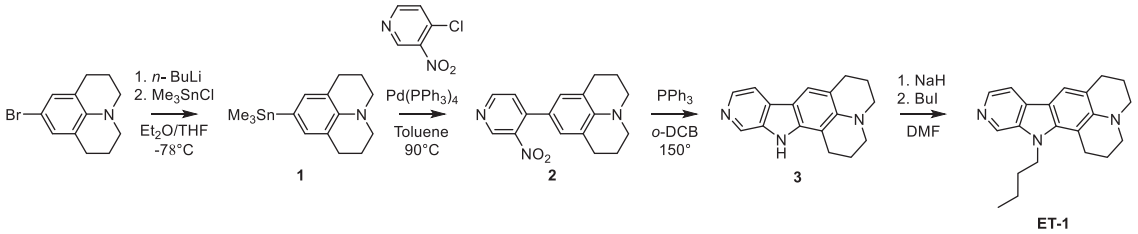

Scheme 1. Synthesis of **ET-1**

The photoabsorption and fluorescence spectra of **ET-1** and 9-methyl pyrido[3,4-*b*]indole (**9-MP**) as a reference in various solvents are shown in Figure 2, and their optical data are summarized in Table 1. In all of the solvents, **9-MP** exhibits a vibronic-structured absorption band at around 350 nm, while for **ET-1** the absorption band at around 350 nm is broadened and shows a slight red-shift with increase in solvent polarity from toluene to DMSO, which could be originating from the ICT excitation. The absorption band of **ET-1** exhibits at a little longer wavelength (ca. 5 nm) than that of **9-MP**. Interestingly, for **ET-1**, a very weak and broad absorption band appeared at 400-450 nm was specifically observed in methanol. Moreover, it is worth noting here that the molar extinction coefficient (ε) for the ICT band of **ET-1** is ca. 20 000 M^{-1} cm^{-1}, which is much higher than that of **9-MP** (ca. 5000 M^{-1} cm^{-1}). It is seen clearly from Figure 2a and 2c

that the absorption properties of both **ET-1** and **9-MP** in aprotic solvents are nearly independent of the solvent polarity. This fact indicates that the electronic and structural characteristics of the ground and Franck-Condon (FC) excited states do not differ much with a change in solvent polarity. The corresponding fluorescence spectra in aprotic solvents show that **9-MP** exhibits a vibronic-structured fluorescence band (λ_{em} = ca. 370 nm), which is almost independent of solvent polarity, as with the absorption spectra of **9-MP**. On the other hand, **ET-1** in aprotic solvents exhibits a fluorescence band without vibronic structures at around 380–420 nm (Figure 2b and d). In contrast to the absorption spectra of **ET-1**, the fluorescence spectra in aprotic solvents are dependent on solvent polarity. The fluorescence maxima of **ET-1** show a bathochromic shift upon increasing the solvent polarity from toluene to DMSO. However, for both **ET-1** and **9-MP** the fluorescence quantum yield (Φ_f) is nearly independent of solvent polarity, but **ET-1** exhibits a higher Φ_f (ca. 0.4-0.6) value than **9-MP** (Φ_f = ca. 0.05-0.10). Moreover, for **9-MP** in methanol, a new fluorescence band that appeared at 450 nm arising from the excited state of the cationic exciplex (CL), which is attributed to the formation of the hydrogen-bonded proton transfer complex (PTC) between the pyridinic nitrogen atom of **9-MP** and the hydroxyl group of the alcohol molecules as a proton donor, has been already reported.[5] Interestingly, for **ET-1** in ethanol a new fluorescence band appeared at around 490 nm, that is, **ET-1** in ethanol shows a bimodal fluorescence band with peaks at around 420 nm and 490 nm. In addition, in methanol the fluorescence band at around 400 nm disappeared and thus the fluorescence band from only the CL excited state was observed at around 500 nm. Thus, these results suggest that the difference in the absorption and fluorescence properties of **ET-1** between methanol and ethanol is attributed to the degree of the formation of the hydrogen-bonded complex (in the ground

state) and PTC (in the excited state) in protic solvents. This may be explained by the fact that there is a difference in the static dielectronic constant (ε) between methanol (ε = 32.66) and ethanol (ε = 24.55). Solvent-dependent shifts in the fluorescence maxima of some fluorescent dyes can be mainly attributed to the dipole–dipole interactions between the fluorescent dye and solvent molecules.20 Thus, in order to get an insight into the fluorescence solvatochromisms of **ET-1** and **9-MP**, the relationships between the solvent polarity dependent fluorescence wavelength at around 380–420 nm for **ET-1** and 370 nm for **9-MP** (for all of the solvents, except methanol for **ET-1**) and the dipole moments of the dye molecules were investigated on the basis of the Lippert–Mataga equation (eq 1):

$$\Delta\nu = \frac{1}{4\pi\varepsilon_0} \cdot \frac{2\Delta\mu^2}{hca^3} \Delta f \qquad (1)$$

where $\Delta\nu$ is the SS value in wavenumber, ε_0 is vacuum permittivity, h is Planck's constant, c is velocity of light, a is the Onsager radius of the dye molecule estimated by DFT calculation (5.68 Å and 4.82 Å for **ET-1** and **9-MP**, respectively) and $\Delta\mu$ is the difference in the dipole moment of the dyes between the ground (μ_g) and the excited (μ_e) state, respectively. Δf is the orientation polarizability calculated as following equation (eq 2)

$$\Delta f = \frac{\varepsilon - 1}{2\varepsilon + 1} - \frac{n^2 - 1}{2n^2 + 1} \qquad (2)$$

Where ε and n are the static dielectronic constant and the refractive index of the solvent, respectively. Therefore, based on eq (1), the change in dipole moment, $\Delta\mu = \mu_e - \mu_g$, can simply be estimated from the slope of a plot of $\Delta\nu$ against Δf. The Lippert–Mataga plots for **ET-1** and **9-MP** are shown in Figure 3. The plot for **ET-1** shows reasonably linear relationship, suggesting that dipole–dipole interactions between the dye and solvent molecule are mainly responsible for the solvent-dependent fluorescence shift. On the other hand, the plot for **9-MP** shows very shallow slope, that is, the slope for **ET-1** (m_s =

6260 cm^{-1}) is much steeper than that for **9-MP** (993 cm^{-1}). The $\Delta\mu$ values for **ET-1** and **9-MP** is 10.67 D and 3.33 D, respectively. Consequently, the Lippert–Mataga plots for **ET-1** and **9-MP** indicate that the $\Delta\mu$ value of **ET-1** is significantly larger than that of **9-MP**, that is, for the D-A dye **ET-1** the me value in the excited state is significantly larger than the mg value in the ground state, which explains our finding that **ET-1** shows large red-shifts in their fluorescence maxima at around 400 nm in polar solvents and that the Stokes shift values for **ET-1** in polar solvents are much larger than those in nonpolar solvents (Table 1).

Table 1. Optical data of **ET-1** and **9-MP** in various solvent

Dye	Solvent	λ_{abs} / nm	ε / M^{-1} cm^{-1}	λ_{em} / nm	Φ_f[a]	Stokes shift / cm^{-1}
ET-1	Toluene	363	21100	381	0.47	1301
	1,4-dioxane	361	19800	386	0.61	1794
	THF	361	21400	389	0.40	1993
	Acetone	360	22500	402	0.57	2902
	Acetonitrile	361	19900	411	0.38	3370
	DMSO	363	19100	416	0.44	3510
	Ethanol	368	19400	419, 489	0.54	3308, 6724
	Methanol	367	16900	501	0.44	7288
9-MP	Toluene	358	5700	368	0.05	759
	1,4-dioxane	357	5700	364	0.07	539
	THF	357	5400	366	0.05	689
	Acetone	356	5500	369	0.03	990
	Acetonitrile	358	5400	368	0.04	759
	DMSO	360	5300	371	0.08	824
	Ethanol	360	5000	372	0.06	896
	Methanol	360	4300	375, 450	0.09	1111, 5556

[a] Fluorescence quantum yields

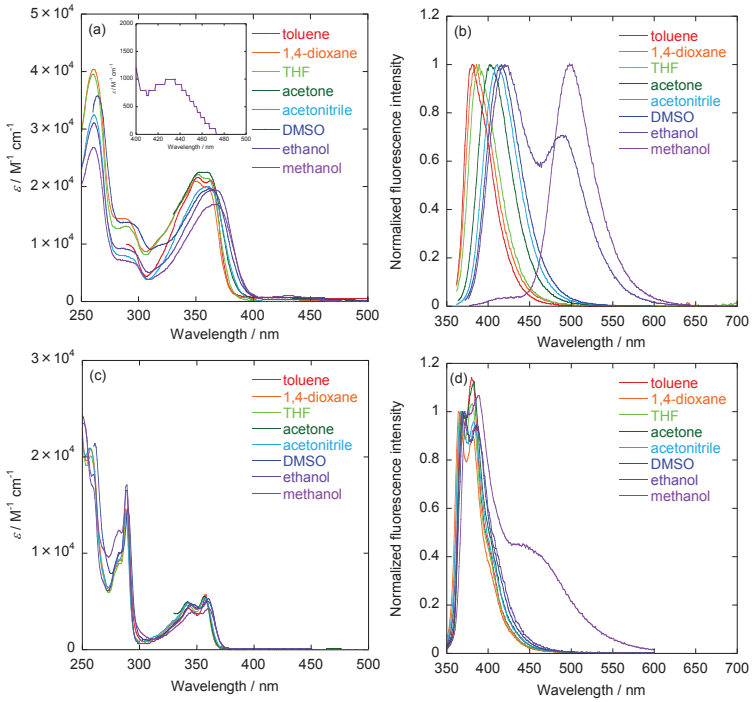

Figure 2. (a) Photoabsorption and (b) fluorescence spectra of **ET-1**. (c) Photoabsorption and (d) fluorescence spectra of **9-MP**.

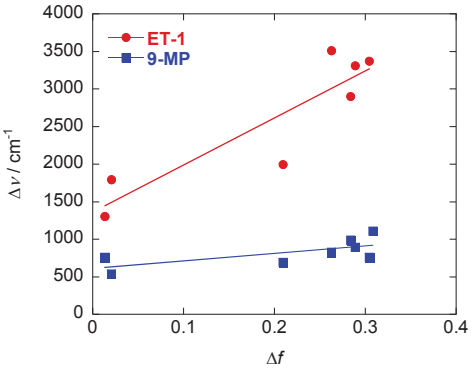

Figure 3. Lippert-Mataga plots for **ET-1** and **9-MP**

More interestingly, upon the addition of boron trifluoride diethyl etherate (BF_3-OEt_2) as a Lewis acid or CF_3COOH as a Brønsted acid to **ET-1** and **9-MP** in acetonitrile, new photoabsorption and fluorescence bands appeared at a longer wavelength region, with simultaneous decrease compared to those of the pristine **ET-1** and **9-MP**. Moreover, it was found that the new photoabsorption and fluorescence bands of **ET-1** appear at a

longer wavelength region than in **9-MP**. Thus, as shown in Figure 4, upon the addition of BF_3-OEt_2 to **ET-1** and **9-MP** in acetonitrile, the photoabsorption band at around 350 nm for both **ET-1** and **9-MP** decreases with the simultaneous appearance of a new photoabsorption band at around 440 nm with an isosbestic point at 380 nm for **ET-1** and at around 390 nm with an isosbestic point at 362 nm for **9-MP**, which suggests the formation of the complex with BF_3. The absorbance of the new photoabsorption band for **ET-1** levels off when 1.0 equivalent of BF_3-OEt_2 is added. On the other hand, the new photoabsorption band for **9-MP** levels off with the addition of 2.0 equivalents of BF_3-OEt_2. As with the addition of BF_3-OEt_2, the addition of CF_3COOH to **ET-1** and **9-MP** in acetonitrile caused a decrease in the absorption band at around 350 nm with an isosbestic point (382 nm for **ET-1** and 362 nm for **9-MP**) and the simultaneous appearance of a new photoabsorption band in the longer wavelength region, which also suggests the formation of a complex with CF_3COOH (Figure 5). The absorbance of the new photoabsorption band for **ET-1** and **9-MP** levels off upon the addition of 1.5 equivalents and 2.5 equivalents of CF_3COOH, respectively. Thus, this result strongly indicates the formation of the 1 : 1 Py(N)–B complex with BF_3 and the Py(N)–hydrogen-bonded proton transfer (Py(N)–H) complex for **ET-1**. As with the absorption spectra for **ET-1**, upon increasing the BF_3-OEt_2 or CF_3COOH concentration the fluorescence intensity at 410 nm is significantly reduced, with the accompanying appearance of a new fluorescence band at 510 nm with an isoemissive point at 474 nm for BF_3-OEt_2 and 472 nm for CF_3COOH. The intensity of the new fluorescence band levels off with the addition of 1.0 equivalent of BF_3-OEt_2 and 1.5 equivalents of CF_3COOH. On the other hand, for **9-MP**, upon the addition of BF_3-OEt_2 or CF_3COOH, the fluorescence band at around 370 nm decreases gradually with the simultaneous appearance of a new fluorescence band at around 460

nm with an isoemissive point at 415 nm for BF_3-OEt_2 and 417 nm for CF_3COOH. The intensity of the new fluorescence band levels off with the addition of 2.0 equivalents of BF_3-OEt_2 and 2.5 equivalents of CF_3COOH. The Φ_f values for **ET-1** and **9-MP** with the addition of BF_3-OEt_2 or CF_3COOH are higher than those for the pristine **ET-1** and **9-MP** in acetonitrile ($\Phi_f = 0.6$ with the addition of BF_3-OEt_2 and CF_3COOH for ET-1, $\Phi_f = 0.52$ and 0.32 with the addition of BF_3-OEt_2 and CF_3COOH, respectively, for **9-MP**). As shown in the insets of Figure 4 and 5, the colors of both **ET-1** and **9-MP** in acetonitrile are colorless. Upon the addition of BF_3-OEt_2 or CF_3COOH, for **ET-1** the color changed from colorless to yellow and the fluorescence colors changed from blue to green, but for **9-MP** blue fluorescence appears. Consequently, these results demonstrate that the 1 : 1 Py(N)–B complex with BF_3 and the Py(N)–H complex for **ET-1** are effectively formed and are stable in solution due to the strong Py(N)–B interaction or Py(N)– hydrogen-bond, which can be attributed to the enhanced basicity or the accumulated electron density on the nitrogen atom of the pyridine ring caused by the introduction of the julolidine (quinolizidine) moiety as a strong electron-donating group, compared to **9-MP**, and thus indicating that the D-A-type dye **ET-1** possesses the ability to act as a colorimetric and fluorescent sensor for Brønsted and Lewis acids.

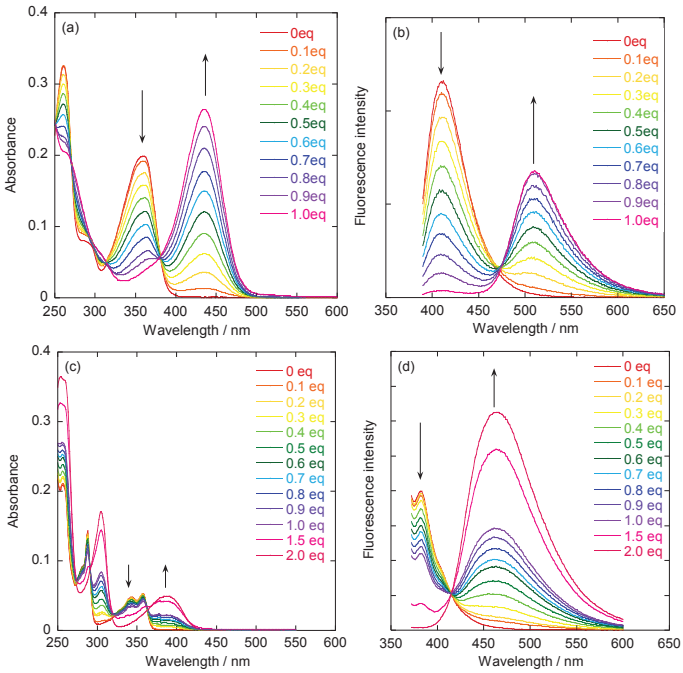

Figure 4. (a) Photoabsorption and (b) fluorescence spectral change of **ET-1** upon the addition of BF_3-OEt_2 (0-1.0 equiv.). (c) Photoabsorption and (d) fluorescence spectral change of **9-MP** upon the addition of BF_3-OEt_2 (0-2.0 equiv.).

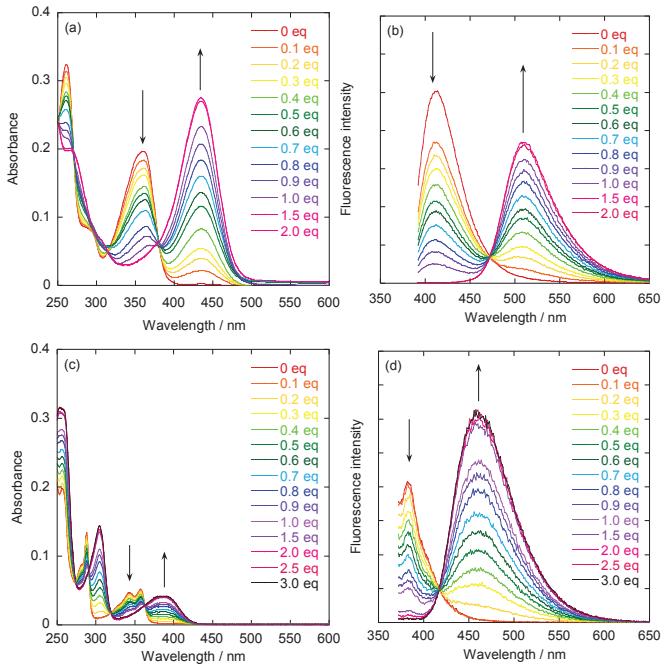

Figure 5. (a) Photoabsorption and (b) fluorescence spectral change of **ET-1** upon the addition of CF_3COOH (0-2.0 equiv.). (c) Photoabsorption and (d) fluorescence spectral change of **9-MP** upon the addition of CF_3COOH (0-3.0 equiv.).

To confirm the formation of the Py(N)–B complex with BF_3 and the Py(N)–H complex with CF_3COOH for both **ET-1** and **9-MP**, ^1H NMR spectral measurement of **ET-1** and **9-MP** with and without the addition of BF_3-OEt_2 or CF_3COOH in acetonitrile-d_3 were performed (Figure 6 and 7). For the ^1H NMR spectra without the addition of BF_3-OEt_2 or CF_3COOH, it is worth mentioning here that the chemical shifts of the aromatic protons on the pyrido[3,4-*b*]indole skeleton for **ET-1** show an upfield shift compared to those for **9-MP**. This fact also indicates that for **ET-1** the electron density on the nitrogen atom of the pyridine ring is enhanced by the introduction of the julolidine (quinolizidine) moiety as a strong electron-donating group. Interestingly, remarkable differences were observed between **ET-1** and **9-MP** when 1.0 equivalent of BF_3-OEt_2 or 1.5 equivalents of CF_3COOH were added: for **ET-1** the chemical shifts of H_a–H_d on the pyrido[3,4-*b*]indole skeleton show an upfield shift for H_a and H_b and a downfield shift for H_c and H_d, but for **9-MP** the chemical shifts of all of the H_a–H_g on the pyrido[3,4-*b*]indole skeleton show downfield shifts. Based on the ^1H NMR spectral measurement, it is suggested that the addition of BF_3 or CF_3COOH to **9-MP** can lead to formation of the Py(N)–B complex (**BF_3–9-MP**) or the Py(N)–H complex (**CF_3COOH–9-MP**) with the benzenoid structure, as shown in Figure 8, resulting in the downfield shift of the aromatic protons on the pyrido[3,4-*b*]indole. On the other hand, **ET-1** exists as the resonance hybrid of the benzenoid structure **ET-1(B)** and the quinonoid structure **ET-1(Q)** due to the strong electron-donating property of the julolidine (quinolizidine) moiety leading to the upfield shift of the aromatic protons on the pyrido[3,4-*b*]indole. Therefore, for **ET-1** the addition of BF_3 or CF_3COOH to the resonance state can lead to the formation of the resonance hybrid of the Py(N)–B complex (**BF_3–ET-1(B)** and **BF_3–ET-1(Q)**) or the Py(N)–H complex (**CF_3COOH–ET-1(B)** and **CF_3COOH–ET-1(Q)**) with the benzenoid structure

and the quinonoid structure, resulting in the downfield and upfield shifts of the aromatic protons on the pyrido[3,4-*b*]indole.

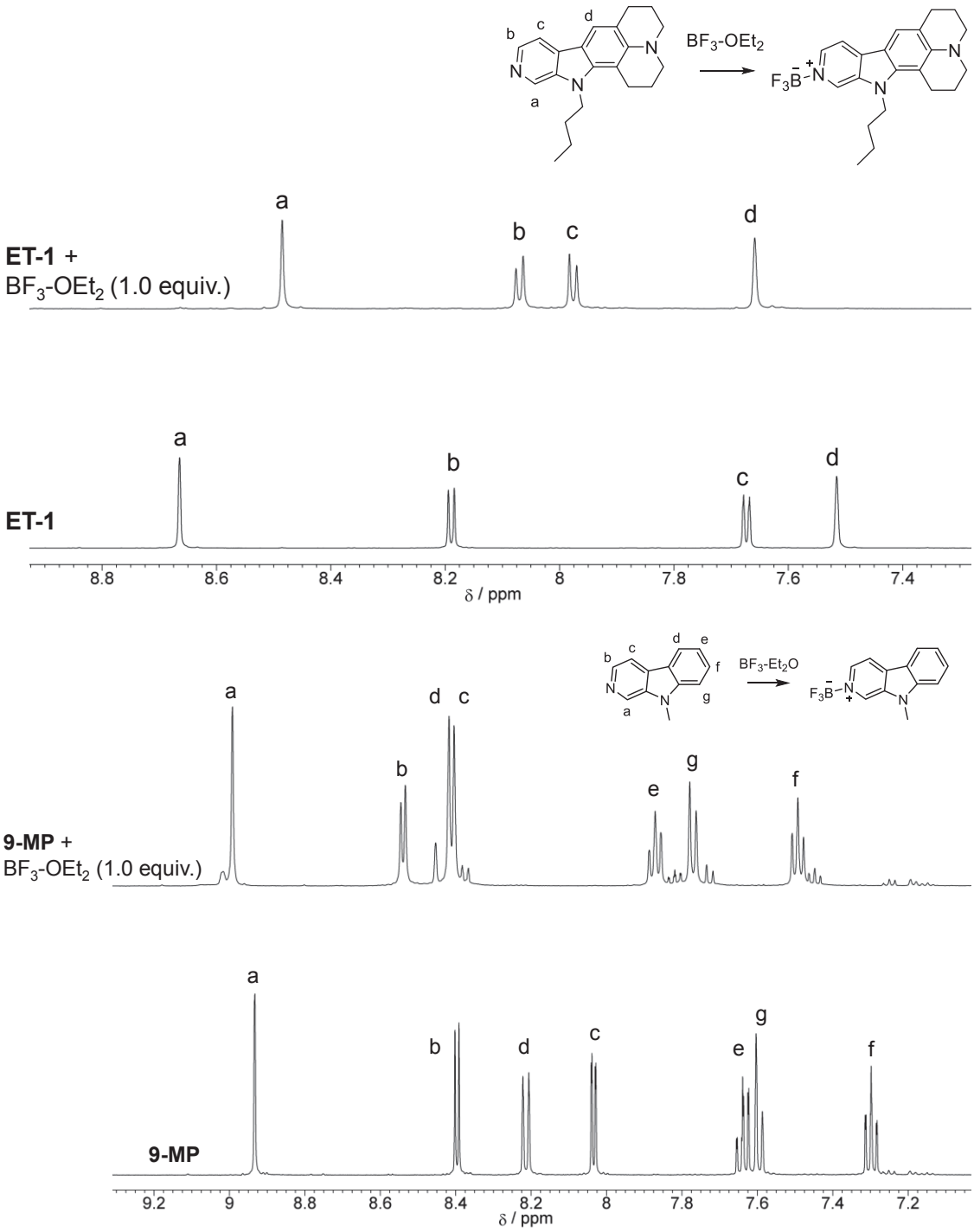

Figure 6. ^{1}H NMR spectra of (a) **ET-1** and (b) **9-MP** with and without addition of 1.0 equivalent of BF_3-OEt_2.

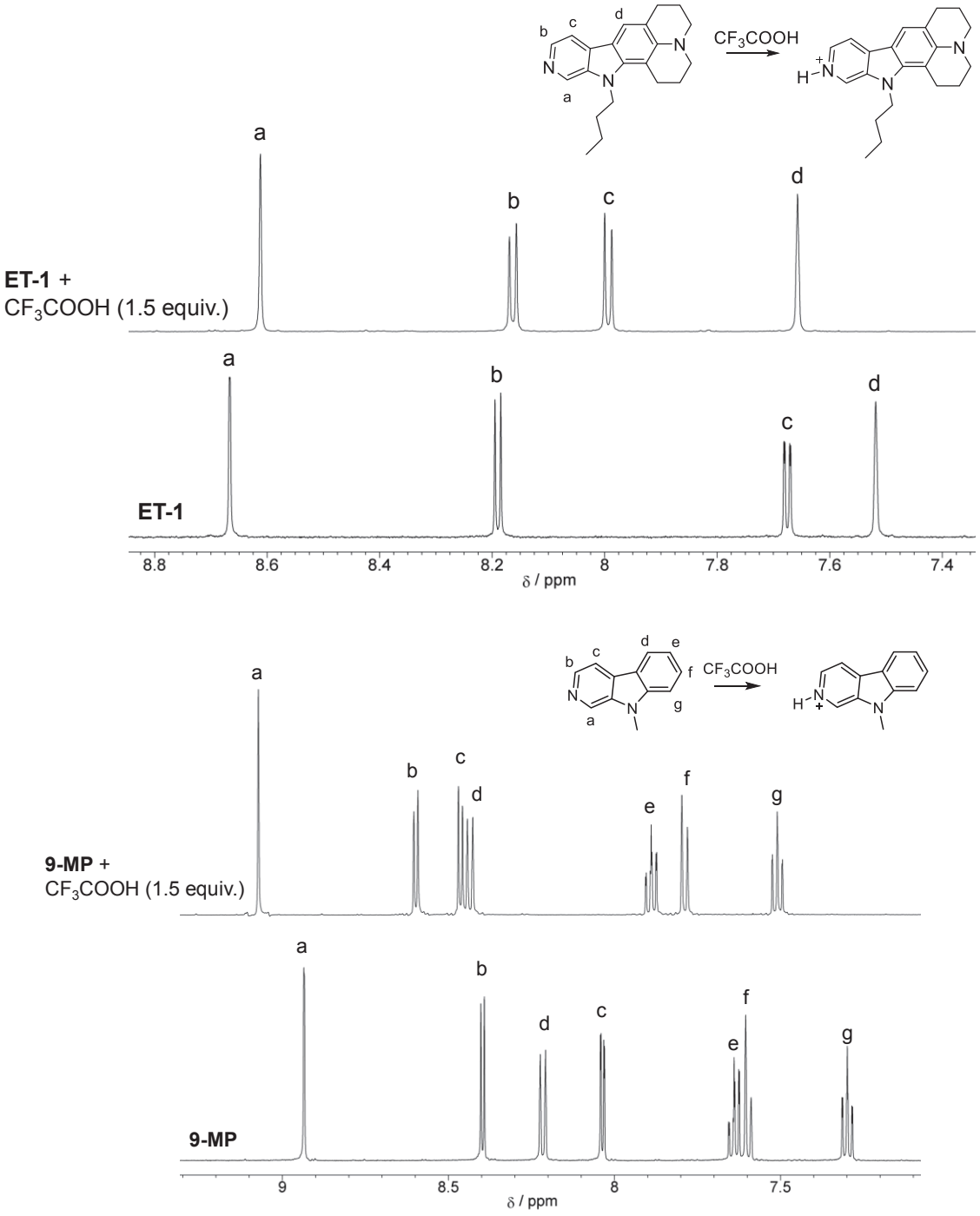

Figure 7. ^{1}H NMR spectra of (a) **ET-1** and (b) **9-MP** with and without addition of 1.0 equivalent of CF_3COOH

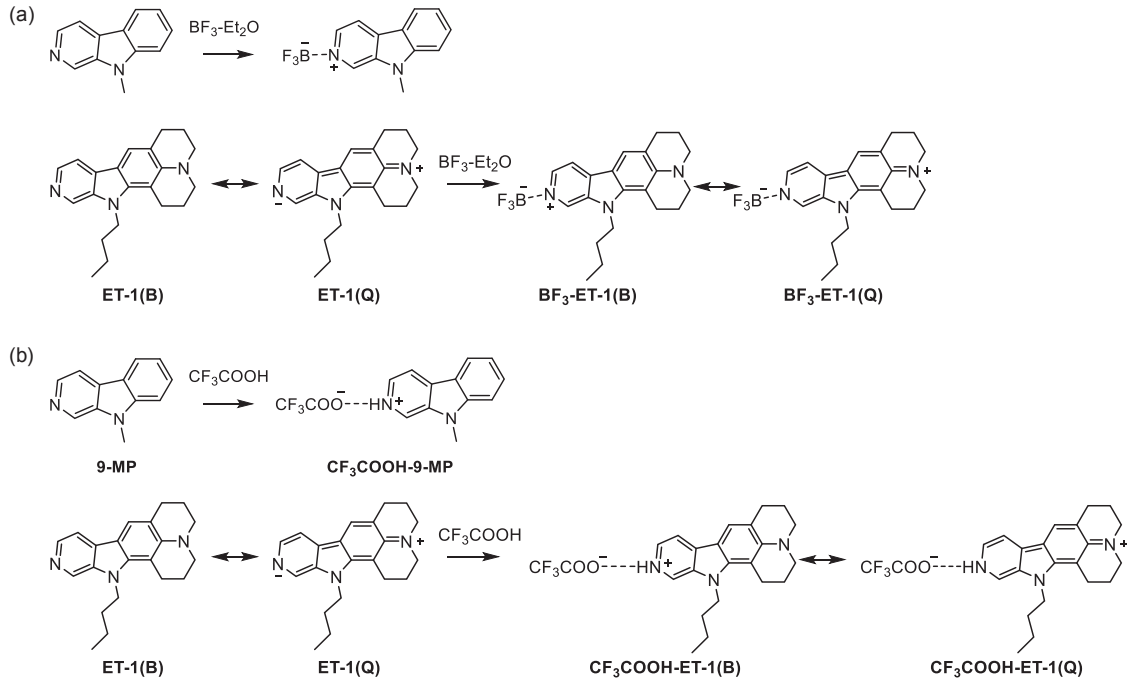

Figure 8. Proposed mechanisms for formation of (a) the Py(N)-B complex and (b) the Py(N)-H complex of **9-MP** and **ET-1** with BF_3 or CF_3COOH

To investigate the electrochemical properties of **ET-1** and **9-MP**, cyclic voltammetry measurements were performed in acetonitrile containing 0.1 M tetrabutylammonium perchlorate (Bu_4NClO_4) (Figure 9). For **ET-1** two reversible oxidation waves were observed at 0.16 and 0.42 V versus ferrocene/ferrocenium (Fc/Fc^+). The corresponding reduction waves were also observed at 0.12 V for the first oxidation wave and 0.37 V for the second oxidation wave. Thus, the julolidine-structured *β*-carboline dye **ET-1** undergoes electrochemically stable oxidation-reduction process. On the other hand, for **9-MP** one irreversible oxidation wave was observed at around 0.9 V. Therefore, this result shows that the first and second oxidation waves for **ET-1** correspond to the oxidations of the julolidine (quinolizidine) moiety and the pyrido[3,4-*b*]indole skeleton, respectively, which is revealed by DFT calculation at the B3LYP/6-31G(d,p) level[22] (Figure 10). It is worth mentioning here that the second oxidation wave for **ET-1** is

cathodically shifted by ca. 0.5 V compared with the corresponding oxidation wave of **9-MP**, indicating that the introduction of a strong electron-donating group onto the pyrido[3,4-*b*]indole skeleton can lead to a lowered oxidation potential. The HOMO energy levels were estimated from the half-wave potential ($E^{OX}_{1/2}$ = 0.18 V) of the first oxidation for **ET-1** and the onset (E^{ox}_{onset} = 0.80 V) of the oxidation potential for **9-MP**. The HOMO energy level (–[$E^{ox}_{1/2}$ + 4.8] eV = –4.98 eV) of **ET-1** is higher than that of **9-MP** (5.60 eV), which is attributed to the introduction of the electron-donating julolidine (quinolizidine) moiety. The LUMO energy levels of **ET-1** and **9-MP** were estimated from the $E^{ox}_{1/2}$ or the E^{ox}_{onset} and an intersection of the photoabsorption and fluorescence spectra in acetonitrile (383 nm, 3.24 eV for **ET-1** and 362 nm, 3.43 eV for **9-MP**). The LUMO energy level of **ET-1** (–1.74 eV) is also higher than that of **9-MP** (–2.17 eV). Thus, the HOMO and the LUMO energy levels of **ET-1** are higher than those of **9-MP**, but from **9-MP** to **ET-1** the rise of the HOMO energy level is larger than that of the LUMO energy level. Consequently, it was revealed that the red-shift of the photoabsorption band for **ET-1** relative to **9-MP** is attributed to destabilization of the HOMO level through the introduction of the julolidine (quinolizidine) moiety with a strong electron-donating ability, resulting in a decrease in the HOMO-LUMO band gap.

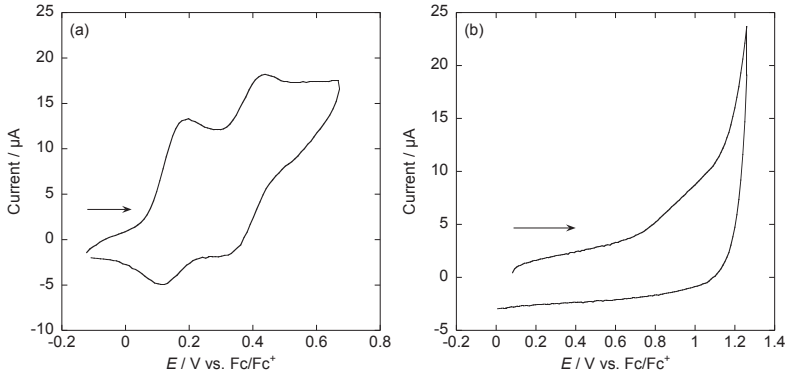

Figure 9. Cyclic voltammograms of (a) **ET-1** and (b) **9-MP** in acetonitrile cantaining 0.1 M of Bu_4NClO_4. The arrow denotes the direction of the potential scan.

To examine the electronic structure of julolidine-structured pyrido[3,4-*b*]indole, the molecular orbitals of **ET-1**, **9-MP** and the Py(N)–B complexes (**BF_3-ET-1** and **BF_3-9-MP**) were calculated using density functional theory (DFT) at the B3LYP/ 6-31G(d,p) level (Figure. 10). The DFT calculations indicate that for **9-MP** the HOMO and the LUMO are delocalized over the whole molecule. On the other hand, for **ET-1** the HOMO−1 is delocalized over the whole molecule, but the HOMO and the LUMO are mostly localized on the pyrido[3,4-*b*]indole skeleton containing the julolidine moiety and the pyrido[3,4-*b*]indole skeleton, respectively. Accordingly, the DFT calculations reveal that for the D-A dye **ET-1** the dye excitations upon light irradiation induce an ICT from the julolidine moiety to the pyridine moiety. Moreover, the DFT calculations demonstrate that the HOMO and the LUMO energy levels of **ET-1** are higher than those of **9-MP**, but from **9-MP** to **ET-1** the rise of the HOMO energy level is larger than that of the LUMO energy level, which is in good agreement with the experimental results from the CV (Figure 9) and the photoabsorption and fluorescence spectral analyses (Figure 2). For both **BF_3-ET-1** and **BF_3-9-MP**, the HOMO and the LUMO are mostly localized on almost the same moiety as those of **ET-1** and **9-MP**. The HOMO and the LUMO energy levels of **BF_3-ET-1** and **BF_3-9-MP** are lower than those of **ET-1** and **9-MP**, but from **BF_3–ET-1** and **BF_3-9-MP** to **ET-1** and **9-MP** the lowering of the LUMO energy level is greater than that of the HOMO energy level. Accordingly, the DFT calculations reveal that the large red-shifts of the photoabsorption band for the Py(N)–B complex as well as the Py(N)–H complex relative to the pristine **ET-1** and **9-MP** are attributed to the stabilization of the LUMO energy level through the coordination of BF_3 and the hydrogen-bonded proton transfer of CF_3COOH to the pyridine moiety, resulting in a decrease in the HOMO–LUMO band gap.

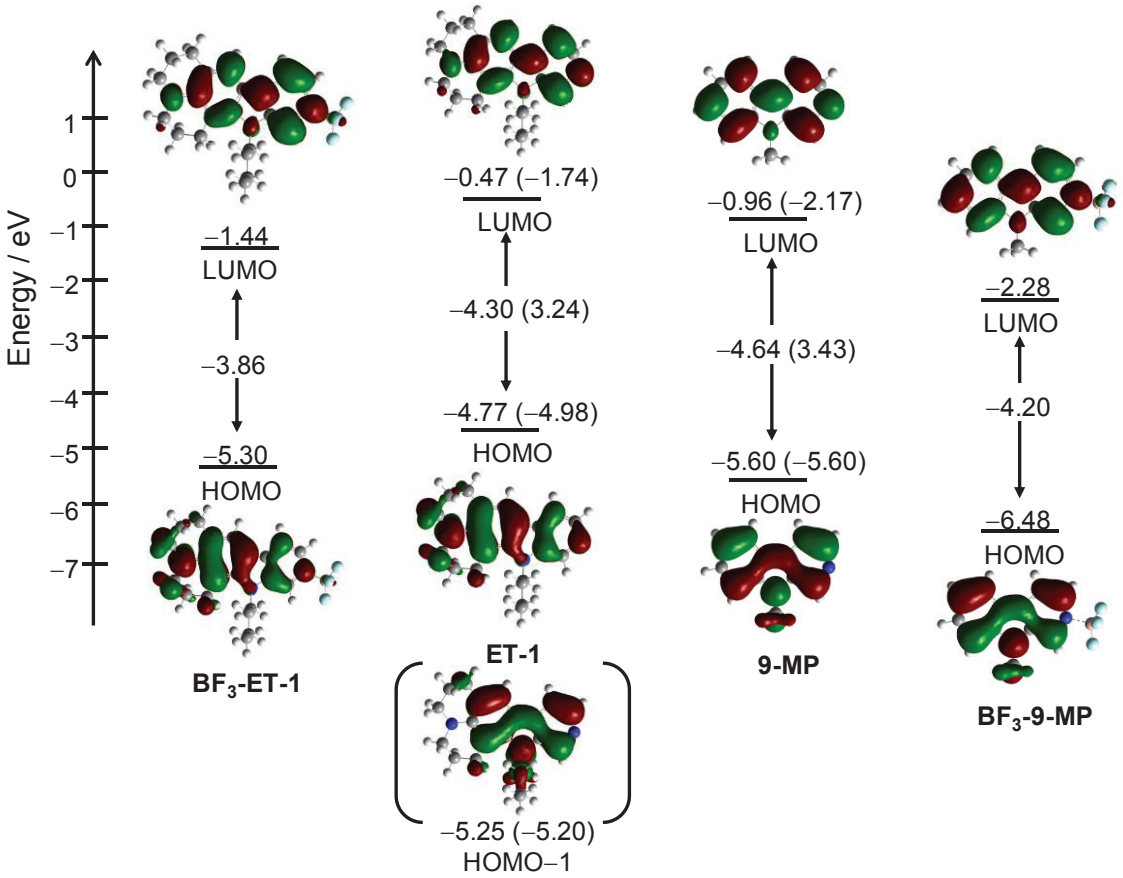

Figure 10. Energy level diagram, HOMO and LUMO of **ET-1** and **9-MP** and their Py(N)–B complexes with BF_3 (**BF_3-ET-1** and **BF_3-9-MP**), derived from DFT calculations. The numbers in parentheses are the experimental values.

Conclusion

As a new type of small D-A fluorescent dye, the julolidine-structured pyrido[3,4-*b*]indole dye **ET-1** has been developed. **ET-1** showed positive fluorescence solvatochromism, and the specific bathochromic shift of the fluorescence band was observed in the protic solvents such as ethanol and methanol. It was found that the D-A dye **ET-1** can form a 1 : 1 Py(N)‑B complex with BF_3 as a Lewis acid and a Py(N)‑H complex with CF_3COOH as a Brønsted acid, which exhibit photoabsorption and fluorescence bands at a longer wavelength region than the pristine **ET-1**. It was also demonstrate that for **ET-1** the Py(N)‑B complex or the Py(N)‑H complex is effectively formed due to the strong Py(N)‑B interaction or Py(N)-hydrogen-bond, which can be attributed to the enhanced basicity of the pyridinic nitrogen atom on the *β*-carboline skeleton due to the introduction of the julolidine moiety as a strong electron-donating group. Thus, this work proposes that the D‑A-type dye **ET-1** based on julolidinestructured pyrido[3,4-*b*]indole possesses the ability to act as a colorimetric and fluorescent sensor for Bronsted and Lewis acids.

Acknowledgements

Chapter 4 is reproduced from "Synthesis and optical and electrochemical properties of julolidine-structured pyrido[3,4-*b*]indole dye; T. Enoki, K. Matsuo, J. Ohshita and Y. Ooyama, *Phys. Chem. Chem. Phys.*, **2017**, *19*, 3565-3574." with permission from the PCCP Owner Societies.

Reference

1. (*a*) R. Guliyev, A. Coskun and E. U. Akkaya, *J. Am. Chem. Soc*., **2009**, *131*, 9007; (*b*) M. H. Kim, H. H. Jang, S. Yi, S.-K. Chang and M. S. Han, *Chem. Commun.*, **2009**, 4838; (*c*) F. Qian, C. Zhang, Y. Zhang, W. He, X. Gao, P. Hu and Z. Guo, *J. Am. Chem. Soc*., **2009**, *131*, 1460; (*d*) R. Yoshii, A. Hirose, K. Tanaka and Y. Chujo, *J. Am. Chem. Soc*., **2014**, *136*, 18131; (*e*) Y. Hu, Z. Zhao, X. Bai, X. Yuan, X. Zhangaand and T. Masuda, *RSC Adv*., **2014**, *4*, 55179; (*f*) Y. I. Park, O. Postupna, A. Zhugayevych, H. Shin, Y.-S. Park, B. Kim, H.-J. Yen, P. Cheruku, J. S. Martinez, J. W. Park, S. Tretiak and H.-L. Wang, *Chem. Sci*., **2015**, *6*, 789; (*g*) C. R. Woodford, E. P. Frady, R. S. Smith, B. Morey, G. Canzi, S. F. Palida, R. C. Araneda, W. B. Kristan, Jr., C. P. Kubiak, E. W. Miller and R. Y. Tsien, *J. Am. Chem. Soc*., **2015**, *137*, 1817.

2. (*a*) J. Yao, Y. Fu, W. Xu, T. Fan, Y. Gao, Q. He, D. Zhu, H. Cao and J. Cheng, *Anal. Chem*., **2016**, *88*, 2497; (*b*) D. Escudero, *Acc. Chem. Res.*, **2016**, *49*, 1816; (*c*) M. L. Saha, X. Yan and P. J. Stang, *Acc. Chem. Res*., **2016**, *49*, 2527; (*d*) H. Liu, X. Xu, Z. Shi, K. Liu and Y. Fang, *Anal. Chem*., **2016**, *88*, 10167; (*e*) V. Mahendran, K. Pasumpon, S. Thimmarayaperumal, P. Thilagar and S. Shanmugam, *J. Org. Chem*., **2016**, *81*, 3597; (*f*) K. Gu, Y. Liu, Z. Guo, C. Lian, C. Yan, P. Shi, H. Tian and W.-H. Zhu, *ACS Appl. Mater. Interfaces*, **2016**, *8*, 26622; (*g*) P. Kumar, R. Kaushik, A. Ghosh and D. A. Jose, *Anal.*

Chem., **2016**, *88*, 11314.

3. (*a*) Z. Yang, W. Qin, J. W. Y. Lam, S. Chen, H. H. Y. Sung, I. D. Williams and B. Z. Tang, *Chem. Sci.*, **2013**, *4*, 3725; (*b*) Y. I. Park, O. Postupna, A. Zhugayevych, H. Shin, Y.-S. Park, B. Kim, H.-J. Yen, P. Cheruku, J. S. Martinez, J. W. Park, S. Tretiak and H.-L. Wang, *Chem. Sci.*, **2015**, *6*, 789; (*c*) S. Shanmugaraju and P. S. Mukherjee, *Chem. Commun*., **2015**, *51*, 16014; (*d*) H. T. Black, I. Pelse, R. M. W. Wolfe and J. R. Reynolds, *Chem. Commun*., **2016**, *52*, 12877; (*e*) A. Sandeep, V. K. Praveen, K. K. Kartha, V. Karunakaran and A. Ajayaghosh, *Chem. Sci*., **2016**, *7*, 4460.

4. (a) K. S. Hettie and T. E. Glass, *Chem. -Eur. J*., **2014**, *20*, 17488; (b) T. A. Khattab, S. Abdelmoez and T. M. Klapctke, *Chem. -Eur. J*., **2016**, *22*, 4157; (c) B. Lee, B. G. Park, W. Cho, H. Y. Lee, A. Olasz, C.-H. Chen, S. B. Park and D. Lee, *Chem. -Eur. J*., **2016**, *22*, 17321; (d) Y. Xu, S. Yu, Q. Chen, X. Chen, Y. Li, X. Yu and L. Pu, *Chem. -Eur. J*., **2016**, *22*, 12061; (e) J. Zhou, V. K. Outlaw, C. A. Townsend and A. E. Bragg, *Chem. -Eur. J*., **2016**, *22*, 15212.

5. (*a*) A. Ruiz, P. Rocca, F. Marsais, A. Godard and Quéguiner, *Tetrahedron*, **1997**, *38*, 6205; (*b*) M. Balón, C. Carmona, P. Guardado and M. A. Muñoz, *Photochem. Photobiol.*, **1998**, *67*, 414; (*c*) C. Carmona, M, Galán, G. Angulo, M. Moñoz, P. Guardado and M. Balón, *Phys. Chem. Chem. Phys.*, **2000**, *2*, 5076; (*d*) L. Agüí, C. Peña-Farfal, P. Yáñez-Sedeño and M. Pingarrón, *Electroanalysis*, **2007**, *19*, 237; (*e*) O. A. F. Rasse-Suriani, F. S. Garcia-Einschlag, M. Rafti, T. Schmidt De Leon, P. M. David-Gara, R. Erra-Balsells and M. F. Cabrerizo, *Photochem. Photobiol*. **2018**, *94*, 36.

6. (*a*) T. J. Hagen, P. Skolnick and J. M. Cook, *J. Med. Chem*., **1978**, *30*, 750; (*b*) X. Yu, W. Lin, R. Pang and Ming Yang, *Eur. J. Med. Chem*., **2005**, *40*, 831; (*c*) I. X. Garcia-Zubiri, H. D. Burrows, J. S. Seixas de Melo, J. Pina, M. Monte-serin and M. J. Tapia,

Photochem. Photobiol. **2007**, *83*, 1455; (*d*) R. Ikeda, T. Kimura, T. Tsutsumi, S. Tamura, N. Sakai and T. Konakahara, *Bioorg. Med. Chem. Lett.*, **2012**, *22*, 3506; (*e*) N. A. Lunagariya, V. M. Gohil, V. Kushwah, S. Neelagiri, S. Jain, S. Singh and K. K. Bhutani, *Bioorg. Med. Chem. Lett.*, **2016**, *26*, 789.

Chapter 5

Development of the colorimetric and fluorescence sensors for water based on the *β*-carboline-boron trifluoride complex

Chapter 5-1

Colorimetric and ratiometric fluorescence sensing of water based on 9-methyl pyrido[3,4-*b*]indole-boron trifluoride complex

Introduction

Development of colorimetric and ratiometric fluorescent sensors for the detection and quantification of water in samples and products, for instance, solutions, solids, and gas or water on the surface of substrate have been of great importance because of not only fundamental study in analytical chemistry, photochemistry, and photophysics but also their potential applications to environmental and quality control monitoring systems and industry.[1-10] Among them, ICT (intramolecular charge transfer)-,[11, 12] PET (photo-induced electron transfer)-,[13, 14] or ESIP (excited state intramolecular proton transfer)-[15] type fluorescent sensors for water have been designed and synthesized so far, and the optical sensing properties of these fluorescent sensors for detection and quantification of water were investigated from the viewpoints of the relationship between the ICT, PET, or ESIP characteristics and the intermolecular interaction of the sensor with water molecules. In particular, the PET-type fluorescence sensor based on the fluorescence enhancement system is useful for the detection and quantification of a trace amount of water in organic solvents because the fluorescence intensity of the sensor increases as a function of water

content in organic solvents, which is attributed to the suppression of PET from the electron donor part to the photo-excited fluorophore due to the intermolecular interaction between the fluorescent sensors and water molecules. However, not only does the PET-type fluorescence sensor not allow the colorimetric and ratiometric fluorescent measurements, but it developed so far is also not suitable for the detection of water in solvents containing high water content. On the other hand, donor-π-acceptor (D-π-A) dyes have a large dipole moment and exhibit strong photoabsorption properties originating from the ICT excitation from the donor to acceptor moiety in the D-π-A structures. Moreover, there are also D-π-A dyes possessing the fluorescence properties, and thus it is well known that D-π-A dyes exhibits fluorescence solvatochromism due to the large dipole moment.[16, 17] As a noteworthy structural feature of D-π-A dyes, the HOMOs are delocalized over the π-conjugated systems, in many cases in configurations centering on electron-donating moiety, whereas the LUMOs are delocalized over electron-accepting moiety. Indeed, for the ICT-type sensors based on D-π-A structure for detecting cations, anions and neutral organic species, the dipole moment and electronic structure are changed by the intermolecular interaction (electrostatic interaction) between the electron-donating or the electron-accepting moiety of the sensor and the species accompanying the detection (recognition) of the species, resulting in changes in the photoabsorption, fluorescence (intensity and wavelength) and electrochemical properties (oxidation and reduction potentials).[18] Therefore, the ICT-type sensor allows the colorimetric and ratiometric fluorescent measurements which are preferable because the ratio of the absorption or fluorescence intensity at the two wavelengths is in fact independent of the total concentration of the sensor, photobleaching, fluctuations of light source intensity, sensitivity of the instrument, and so on. For this reason, the author

focused on *β*-carboline (9*H*-pyrido[3,4-*b*]indole) with D-A structure, which has a pyridine ring as a hydrogen bond acceptor, is one of the most promising colorimetric and ratiometric fluorescent sensor skeletons for hydrogen bond donor species such as Brønsted acids, water, alcohols and nucleotides.[19-21] For example, 9-methyl pyrido[3,4-*b*]indole (**9-MP**) in aprotic solvents exhibits a vibronic-structured fluorescence band at around 370 nm (Figure 1). Interestingly, for **9-MP** in alcohols or solvents containing water, a new fluorescence band that appeared at 450 nm arising from the photo-excited state of the cationic exciplex (CL), which is attributed to the formation of the hydrogen-bonded proton transfer complex (PTC) between the pyridinic nitrogen atom of **9-MP** and the hydroxyl group of the alcohol or water as a proton donor, has been already reported.[19, 20a-c] On the other hand, in Chapter 4, it was revealed that **9-MP** can form a Py(N)–B complex (**BF_3-9-MP**) with BF_3 as a Lewis acid in the solution, which exhibits photoabsorption and fluorescence bands at a longer wavelength region than the pristine **9-MP**. More recently, we have designed and developed a D-$(\pi$-A$)_2$-type pyridine-boron trifluoride complex **YNI-2-BF_3** composed of a carbazole skeleton as a donor moiety and two pyridine–boron trifluoride units as an acceptor moiety (Figure 1).[12] It was found that the blue-shift of photoabsorption and the enhancement of fluorescence intensity in the low water content region are attributed to the change in the ICT characteristics due to the dissociation of **YNI-2-BF_3** into the D-$(\pi$-A$)_2$-type pyridine dye **YNI-2** by water molecules. Furthermore, a red-shift of fluorescence bands with the decrease in fluorescence intensity in the high water content region was observed, and it is attributed to the formation of the hydrogen-bonded PTC (**YNI-2-H_2O**) with water molecules as well as the fluorescence solvatochromic properties of **YNI-2**. Consequently, it was demonstrated that the ICT-based pyridine–boron trifluoride complex can act as a

colorimetric and fluorescent sensor for the detection of water in the low and high water content regions in solvents.

Thus, in this chapter, to gain insight into a direction in molecular design toward creating a colorimetric and ratiometric fluorescent sensor for detection of water over a wide range of water content in solvents, the author have designed and developed a 9-methyl pyrido[3,4-*b*]indole-boron trifluoride complex **9-MP-BF$_3$** as a colorimetric and ratiometric fluorescent sensor for detection of water from the low to high water content region in solvents (Figure 1). Herein, based on the results by not only the photoabsorption and fluorescence spectral measurements of **9-MP-BF$_3$** in solvents that contained various concentrations of water, but also the ^{1}H NMR spectral measurements of **9-MP-BF$_3$** with and without the addition of water in the solution, the author report the mechanism of a colorimetric and ratiometric fluorescent sensor based on 9-methyl pyrido[3,4-*b*]indole-boron trifluoride complex **9-MP-BF$_3$** for detection of water over a wide range from low water content to high water content in solvents.

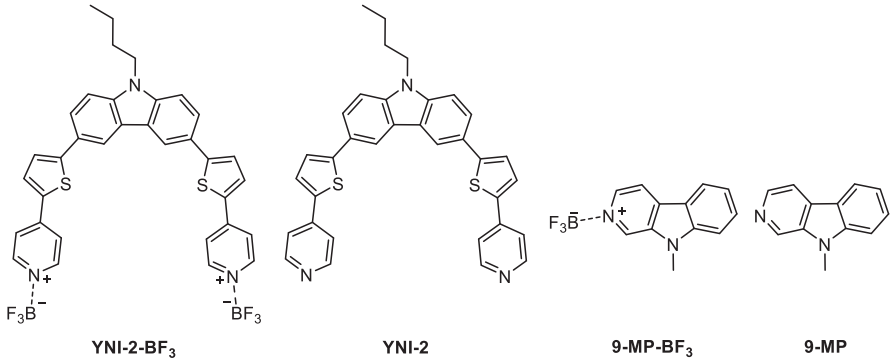

Figure 1. Chemical structures of 9-methyl pyrido[3,4-*b*]indole **9-MP**, the pyridine–boron trifluoride complex **9-MP-BF$_3$**, D-(π-A)$_2$ fluorescent dye **YNI-2** and the pyridine-boron trifluoride complex **YNI-2-BF$_3$**.

Experimental

General

IR spectra were recorded on a SHIMADZU IRAffinity-1 spectrometer using the ATR method. ^{1}H and ^{11}B NMR spectra were recorded on a Varian-500 FT NMR spectrometer. High-resolution mass spectral data by ESI were acquired on a Thermo Fisher Scientific LTQ Orbitrap XL. Photoabsorption spectra were observed with a SHIMADZU UV-3150 spectrophotometer. Fluorescence spectra were measured with a Hitachi F-4500 spectrophotometer. The fluorescence quantum yields were determined by a HORIBA FluoroMax-4 spectrofluorometer by using a calibrated integrating sphere system. The addition of water to organic solvents containing **9-MP** or **9-MP-BF$_3$** was made by weight percent (wt%). The determination of water in acetonitrile was done with a MKC-610 and MKA-610 Karl Fischer moisture titrator (Kyoto Electronics manufacturing Co., Ltd.) based on Karl Fischer coulometric titration for below 1.0 wt% and volumetric titration for 1.0-80 wt%, respectively.

Synthesis

9-Methyl-9*H*-pyrido[3,4-*b*]indole trifluoroborane complex (9-MP-BF$_3$).

To a solution of **9-MP** (0.05 g, 0.27 mmol) in dry ether (3 mL) under a nitrogen atmosphere was added dropwise 47% BF_3-OEt_2 (0.54 mmol) diluted with dry ether (2 mL), and then the solution was stirred for 0.5 h at room temperature. The resulting precipitate was filtered and was washed by dry ether to give **9-MP-BF$_3$** (0.066 g, yield 96 %) as a pale yellow solid; FT-IR (ATR): $\tilde{\nu}$ = 1641, 147, 1061 cm^{-1}; ^{1}H NMR (500 MHz, acetonitrile-d$_3$) δ = 4.07 (s, 3H), 7.50-7.55 (m, 1H), 7.80 (d, J = 8.5 Hz, 1H), 7.88-7.93 (m, 1H), 8.41 (d, J = 6.0 Hz, 1H), 8.45 (d, J = 8.0 Hz, 1H), 8.62 (d, J = 6.0 Hz, 1H), 8.99 Hz (s, 1H) ppm ppm; ^{13}C NMR (125 MHz, acetonitrile-d$_3$); δ = 31.11, 111.98, 120.42,

122.99, 124.60, 125.64, 130.01, 135.52, 135.13, 137.16, 146.26 ppm; ^{11}B-NMR (160 MHz, acetonitrile-d_3) δ = –0.245 ppm; HRMS (ESI): *m*/*z* (%):[M+H^+] calcd for $C_{12}H_{11}N_2$, 183.09167 ; found 183.09041.

Results and Discussion

The 9-methyl pyrido[3,4-*b*]indole-boron trifluoride complex **9-MP-BF$_3$** studied in this work was prepared by treating **9-MP** with BF_3-OEt_2 and fully characterized by ^{1}H NMR, ^{13}C NMR, ^{11}B NMR, FT-IR and high-resolution mass analysis.

The photoabsorption and fluorescence spectra of **9-MP** and **9-MP-BF$_3$** in acetonitrile are shown in Figure 2. **9-MP** and **9-MP-BF$_3$** show two photoabsorption bands at around 290 nm and 360 nm, and 305 nm and 390 nm, respectively. Thus, both the photoabsorption bands of **9-MP-BF$_3$** occur at longer wavelength by ca. 15 nm and ca. 30 nm, respectively, than those of **9-MP**. The molar extinction coefficient (ε_{max}) for the photoabsorption band (λ_{abs}^{max} = 388 nm) of **9-MP-BF$_3$** is 3300 M^{-1} cm^{-1}, which is slightly lower than that (5400 M^{-1} cm^{-1}) of the λ_{abs}^{max} (358 nm) of **9-MP**. For the corresponding fluorescence spectra, **9-MP-BF$_3$** exhibits a fluorescence maximum (λ_{fl}^{max}) at 458 nm, which occurs at a significantly longer wavelength (90 nm) than that (λ_{fl}^{max} = 368 nm) of **9-MP**. These results are attributed to the fact that the electron-withdrawing ability of the pyridyne-BF_3 unit is stronger than that of the pyridyl group.

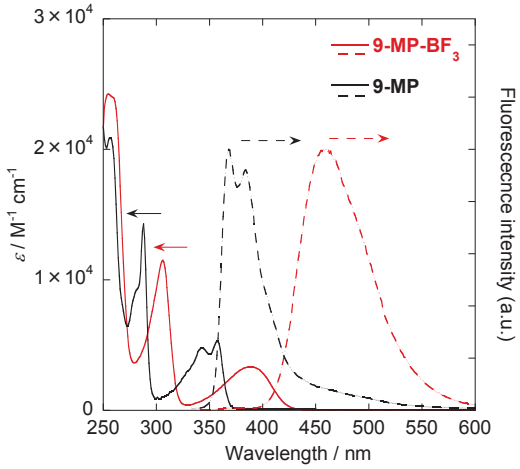

Figure 2. Photoabsorption and fluorescence (λ_{ex} = 323 nm for both **9-MP** and **9-MP-BF$_3$**) spectra of **9-MP** and **9-MP-BF$_3$** in acetonitrile.

In order to investigate the optical sensing ability of **9-MP-BF_3** for water in a solvent, the photoabsorption and fluorescence spectra of **9-MP-BF_3** were measured in acetonitrile that contained various concentrations of water (Figure 3 and 4). Interestingly, it was found that in acetonitrile (as absolute solvent) with 0.043 wt% water content the photoabsorption bands at around 305 nm and 390 nm and fluorescence band at around 460 nm of **9-MP-BF_3** which were measured in one day after the solution was prepared, decrease compared with those of **9-MP-BF_3** which were measured immediately (in 10 min) after the solution was prepared (Figure 3a and 4a). The fact strongly indicates that the time-dependent change of the photoabsorption and fluorescence spectra of **9-MP-BF_3** is due to the intermolecular interaction of **9-MP-BF_3** with water molecules, and the reaction rate is not so fast. Thus, in this chapter the author evaluated the optical sensing property of **9-MP-BF_3** for water by measuring the photoabsorption and fluorescence spectra of the solution containing water in one day after it was prepared. In the low water content range from 0.043 wt% to 2.1 wt%, the two photoabsorption bands at around 305 nm and 390 nm decrease with the simultaneous appearance of two new photoabsorption bands at around 290 nm and 360 nm with isosbestic points at 292 nm and 365 nm, respectively, with the increase in the water content in the acetonitrile solution (Figure 3b). Indeed, the two new photoabsorption bands at around 290 nm and 360 nm are assignable to the photoabsorption bands of **9-MP** due to the dissociation of **9-MP-BF_3** into **9-MP** by water molecules (Figure 2). In the moderate water content range from 2.1 wt% to 40 wt%, the photoabsorption band at around 360 nm gradually shifts to longer wavelength region (Figure 3c), can be ascribed to the formation of the hydrogen-bonded complex (**9-MP-H_2O**) between the pyridinic nitrogen atom of **9-MP** and the hydroxyl group of water molecules.[19, 20a-c] Furthermore, in the high water content range from 40 wt% to 80 wt%,

two photoabsorption bands at around 305 nm and 390 nm gradually reappear with a simultaneous decrease in the photoabsorption band at around 290 nm originating from **9-MP-H_2O**, and it is attributed to the formation of the hydrogen-bonded proton transfer (PTC) complex (**9-MP-H+**) with water molecules (Figure 3d).[19, 20a-c]

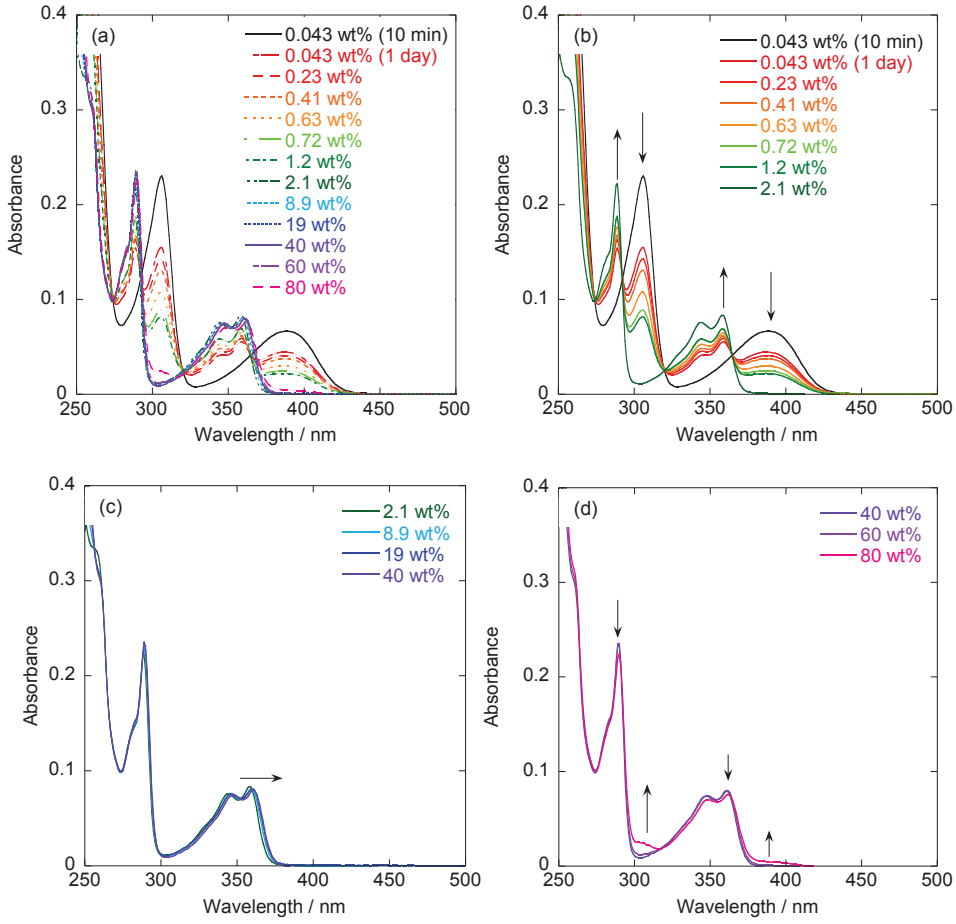

Figure 3. Photoabsorption spectra of **9-MP-BF_3** (c = 1.5×10^{-5} M) in acetonitrile containing water content of (a) 0.043–80 wt%, (b) 0.043–2.1 wt%, (c) 2.1–40 wt% and (d) 40–80 wt%.

On the other hand, for the corresponding fluorescence spectra of **9-MP-BF_3** in the low water content range from 0.043 wt% to 2.1 wt%, a new fluorescence band at around 370 nm with an isoemissive point at 422 nm due to the dissociation of **9-MP-BF_3** into **9-MP** by water molecules gradually appears with a simultaneous decrease in the fluorescence

band at around 460 nm originating from **9-MP-BF$_3$** (Figure 4b). In the moderate water content range from 2.1 wt% to 40 wt%, the fluorescence band at around 370 nm gradually shifts to longer wavelength region with the increase in the fluorescence intensity (Figure 4c), can be ascribed to the formation of **9-MP-H$_2$O**.[19, 20a-c] In the high water content range from 40 wt% to 80 wt%, a new fluorescence band at around 460 nm due to the formation of the PTC complex **9-MP-H+** in the excited state gradually reappears with a simultaneous decrease in the fluorescence band at around 370 nm originating from **9-MP-H$_2$O** (Figure 4d).[19, 20a-c]

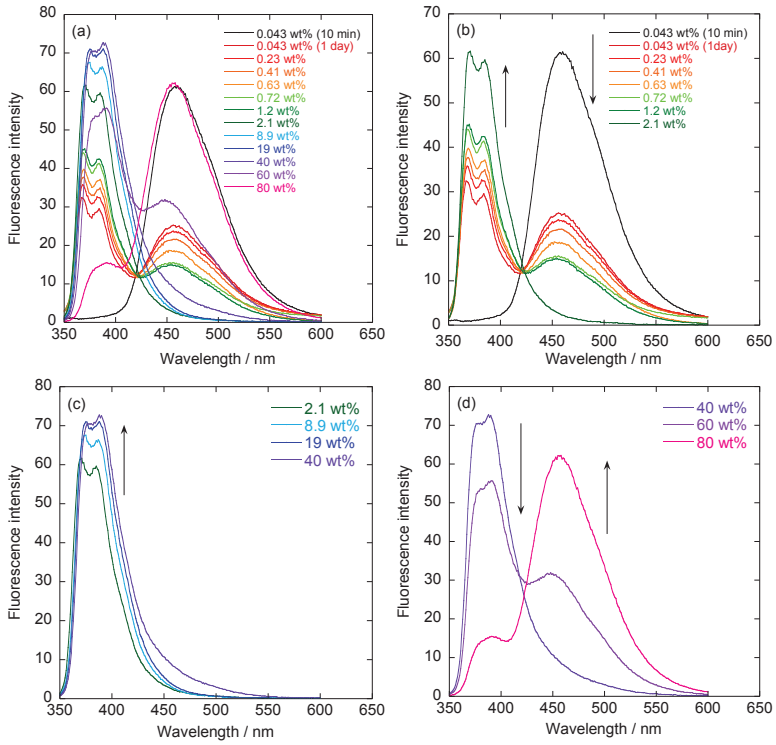

Figure 4. Fluorescence spectra of **9-MP-BF$_3$** (c = 1.5×10^{-5} M) by photoexcitation at 323 nm in acetonitrile containing water content of (a) 0.043–80 wt%, (b) 0.043–2.1 wt%, (c) 2.1–40 wt% and (d) 40–80 wt%.

In order to estimate the sensitivity and accuracy characteristics of **9-MP-BF_3** as a colorimetric and ratiometric fluorescent sensor for the detection of water in acetonitrile, the changes in absorbance and fluorescence intensity are plotted against the water fraction in acetonitrile (Figure 5 and 6). The plots of absorbance for the low water content region below 2.1 wt% demonstrated that the absorbance at around 305 nm and 390 nm decreased linearly as a function of the water content, but the absorbance at around 290 nm and 360 nm increased linearly as a function of the water content (Figure 5a). Indeed, the correlation coefficient (R^2) values for the calibration curve regarding the absorbance at around 290 nm, 305 nm, 360 nm and 390 nm are 0.97, 0.97, 0.95 and 0.97, respectively, which indicate the good linearity (Figure 5b). On the other hand, the plots of absorbance for the water content region over 2.1 wt% did not show appreciable decrease and increase in the absorbance as a function of the water content (Figure 5a). Moreover, the plot of fluorescence intensity for the low water content region below 2.1 wt% demonstrated that the fluorescence peak intensity at around 460 nm decreased linearly as a function of the water content, but the fluorescence peak intensity at around 370 nm increased linearly as a function of the water content (Figure 6a). For the calibration curves of the fluorescence peak intensity (Fl) at around 370 nm and 460 nm, the slope (m_s) and the R^2 values are 13 and 0.97 for the Fl_{370} and –11 and 0.97 for the Fl_{460}, respectively, which indicate the good linearity (Figure 6b). For the plot of the fluorescence intensity for the moderate water content range from 2.1 wt% to 40 wt%, both the fluorescence peak intensities at around 370 nm and 460 nm increased gradually as a function of the water content (Figure 6c), that is, the m_s values are 0.3 for the Fl_{370} and 0.2 for the Fl_{460}, respectively, which are much smaller than those in the low water content region below 2.1 wt%. Furthermore, the plot of the fluorescence intensity for the high water content range from 40 wt% to 80

wt% showed that the fluorescence peak intensity at around 460 nm increased linearly as a function of the water content, but the fluorescence peak intensity at around 370 nm decreased linearly as a function of the water content (Figure 6d). The calibration curves of the Fl at around 370 nm and 460 nm for the high water content region demonstrated that the m_s and the R^2 values are –1.4 and 0.95 for Fl_{370} and 1.3 and 0.99 for Fl_{460}, respectively, which are much smaller than those in the low water content region below 2.1 wt%. In order to further evaluate the radiometric fluorescence response of **9-MP-BF$_3$** to water, the ratio (Fl_{370}/Fl_{460}) of fluorescence intensities at around 370 nm and 460 nm is plotted against the water fraction below 2.1 wt% (Figure 7). The plot revealed the presence of two distinct linear regions in water content below and above 1.2 wt%, that is, the m_s value is 1.6 for the linear region below 1.2 wt% and 27 for the linear region above 1.2 wt%, respectively. The appearance of two distinct regions may be ascribed to the different local concentrations and reaction dynamics between **9-MP-BF$_3$** and water molecules in the water content region below and above 1.2 wt%. In the water content region above 1.2 wt%, water molecules can effectively react with **9-MP-BF$_3$** by the hydration, resulting in faster dissociation of **9-MP-BF$_3$** into **9-MP**, and thus leading to steeper slope than in the water content region below 1.2 wt%. Thus, the detection limit (DL = $3.3\sigma/m_s$, where σ is the standard deviation of the blank sample and m_s is the slope of the calibration curve) was determined from the plot of the fluorescence intensity at around 370 nm versus the water fraction in the low water content region below 2.1 wt% (Figure 6b, $m_s = 13$). The DL value is 0.25 wt%, which are inferior to those of the reported ICT-type fluorescence sensors[11, 12] and PET-type fluorescence sensors.[13, 14] However, for **9-MP-BF$_3$** the photoabsorption spectral change against the water fraction in the water content range from 0.0043 wt% to 80 wt% (Figure 5) and the linear relationship of the

plots for the fluorescence intensity at around 370 nm and 460 nm versus the water fraction in the water content region below 2.1 wt%, 2.1–40 wt%, and 40–80 wt% (Figure 6), as well as the radiometric fluorescence response of **9-MP-BF$_3$** to water (Figure 7), are clearly demonstrated that 9-methyl pyrido[3,4-*b*]indole-boron trifluoride complex **9-MP-BF$_3$** can act as a colorimetric and ratiometric fluorescent sensor for the detection of water over a wide range from low water content to high water content in solvents.

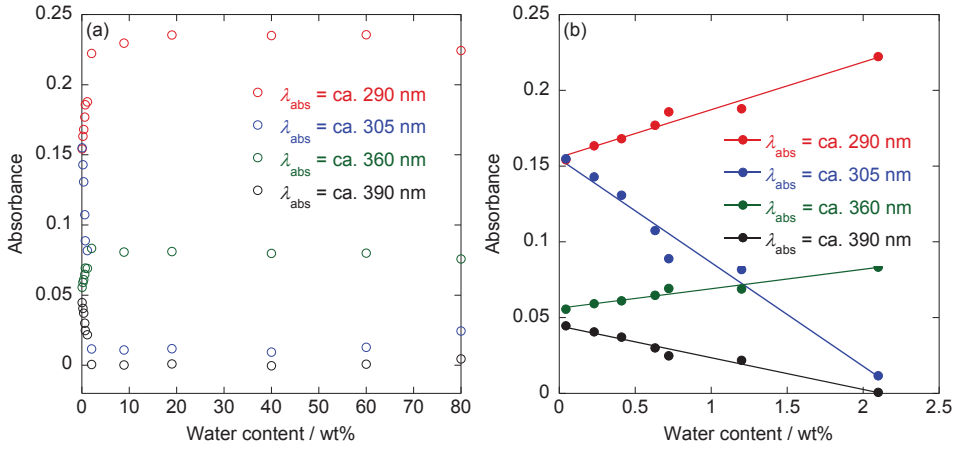

Figure 5. Absorbance at 290 nm, 305 nm, 360 nm and 390 nm of **9-MP-BF$_3$** as a function of water content (a) from 0.043 wt% to 80 wt% and (b) below 2.1 wt% in acetonitrile.

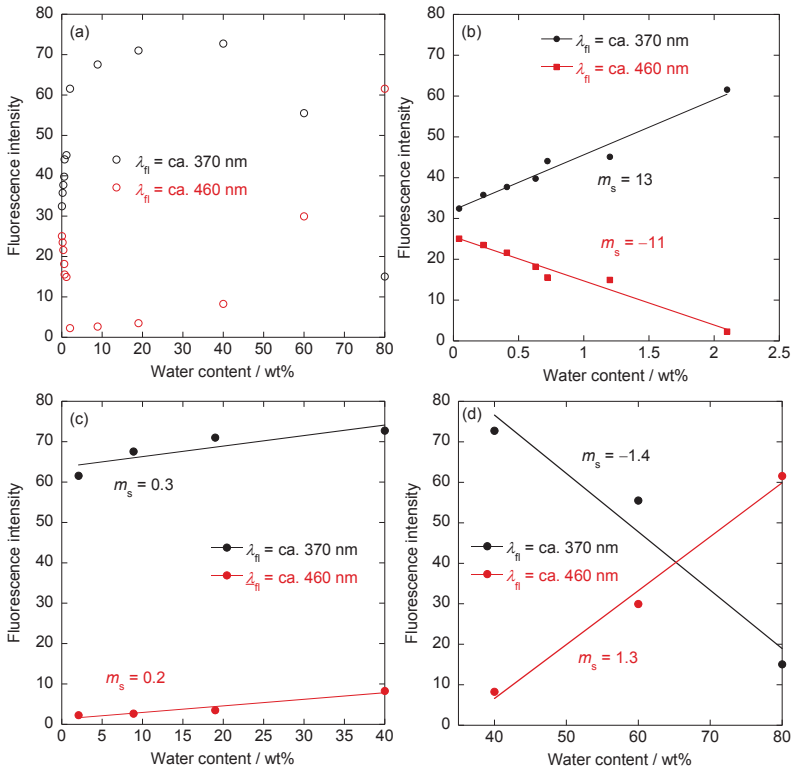

Figure 6. Fluorescence peak intensity at 370 nm and 460 nm of **9-MP-BF$_3$** by photoexcitation at 323 nm as a function of water content (a) from 0.043 wt% to 80 wt%, (b) below 2.1 wt%, (c) form 2.1 wt% to 40 wt% and (d) from 40 wt% to 80 wt% in acetonitrile.

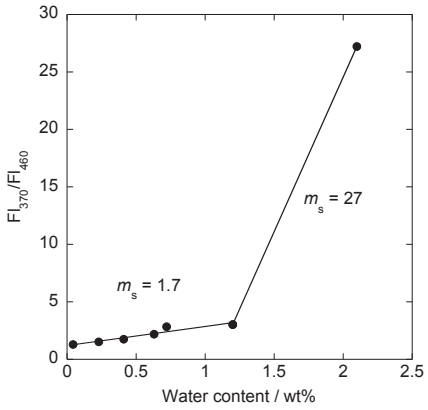

Figure 7. Ratio (Fl_{370}/Fl_{460}) of fluorescence peak intensity at 370 nm and 460 nm of **9-MP-BF$_3$** by photoexcitation at 323 nm as a function of water content below 2.1 wt% in acetonitrile.

In order to elucidate the mechanism for the detection of water over a wide range from low water content to high water content in solvents based on 9-methyl pyrido[3,4-*b*]indole-boron trifluoride complex, ^{1}H NMR spectral measurements of **9-MP-BF$_3$** with and without the addition of water in acetonitrile-d_3 were performed (Figure 8). For the ^{1}H NMR spectrum of **9-MP-BF$_3$** without the addition of water, it is worth noting here that the chemical shifts of all of the aromatic protons (H_a-H_g) on the pyrido[3,4-*b*]indole skeleton show a downfield shift compared to those for **9-MP** (Figure 8a and c). This fact indicates the preparation of 9-methyl pyrido[3,4-*b*]indole-boron trifluoride complex **9-MP-BF$_3$**. On the other hand, the ^{1}H NMR spectrum of **9-MP-BF$_3$** in acetonitrile-d_3 with a water content of 10 wt% (Figure 8b), which corresponds to the maximum absorbance in the absorbance enhancement process of photoabsorption band at around 360 nm and the maximum fluorescence intensity in the fluorescence enhancement process of fluorescence band at around 370 nm, as well as the complete disappearances of photoabsorption band at around 390 nm and fluorescence band at around 460 nm upon addition of water, is similar to that of **9-MP**. Consequently, this result demonstrates the dissociation of **9-MP-BF$_3$** into **9-MP** by water molecules. Thus, as shown in Figure 9, this work revealed that in the low water content region not only an appearance of new photoabsorption band at around 360 nm and a decrease in the photoabsorption band at around 390 nm with an isosbestic point at 365 nm, but also an appearance of new fluorescence band at around 370 nm and a decrease in the fluorescence band at around 460 nm with an isoemissive point at 422 nm are attributed to the dissociation of **9-MP-BF$_3$** into **9-MP** by water molecules. In the moderate water content region the photoabsorption band at around 360 nm and the fluorescence band at around 370 nm gradually shift to longer wavelength region with the increase in the fluorescence intensity,

can be ascribed to the formation of the hydrogen-bonded complex (**9-MP-H_2O**) with water molecules.[19b, 20a-c] Furthermore, in the high water content region two photoabsorption bands at around 305 nm and 390 nm and a fluorescence band at around 460 nm gradually reappear with a simultaneous decrease in the photoabsorption band at around 290 nm and the fluorescence band at around 370 nm, and it is attributed to the formation of the hydrogen-bonded proton transfer complex (**9-MP-H+**) with water molecules.[19, 20a-c]

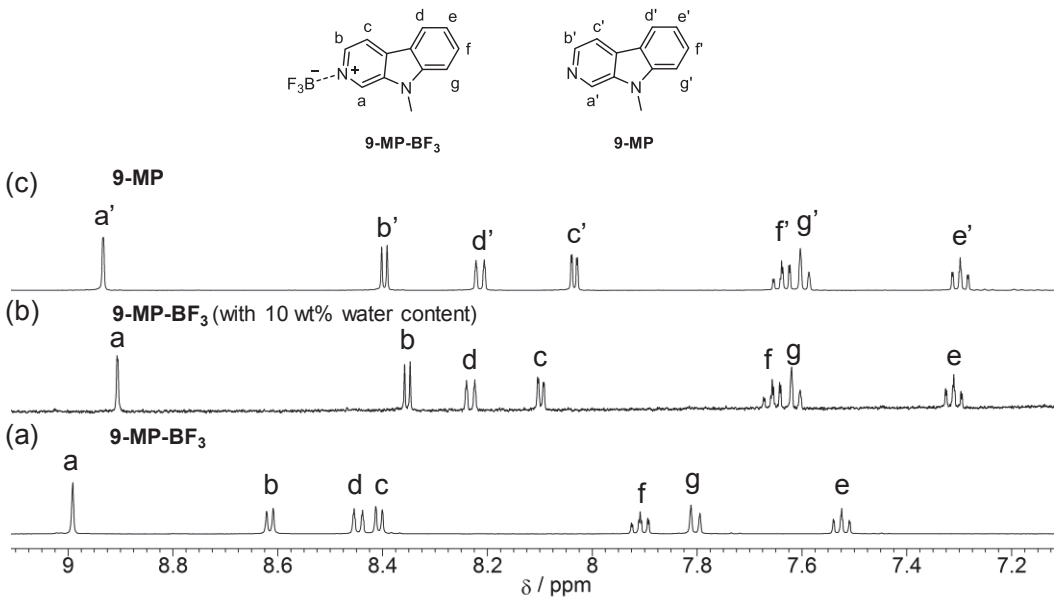

Figure 8. ^{1}H NMR spectra of (a) **9-MP-BF_3** in acetonitrile-d_3, (b) **9-MP-2-BF_3** in acetonitrile-d_3 with 10 wt% water content and (c) **9-MP** in acetonitrile-d_3.

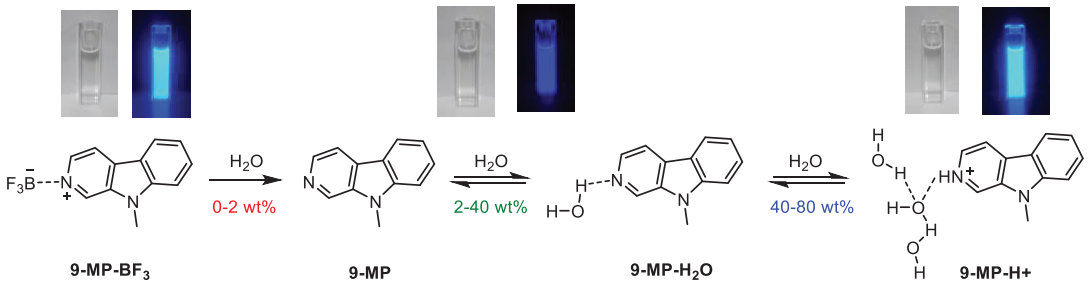

Figure 9. Proposed mechanisms of colorimetric and ratiometric fluorescent sensor **9-MP-BF_3** for the detection of water in solvent; inset: color (left) and fluorescence color (right) images.

Conclusion

As a colorimetric and ratiometric fluorescent sensor for detection of water in solvents, 9-methyl pyrido[3,4-*b*]indole-boron trifluoride complex **9-MP-BF$_3$** have been developed. It was found that in the low water content region the blue-shifts of photoabsorption band with an isosbestic point and fluorescence band with an isoemissive point are attributed to the dissociation of **9-MP-BF$_3$** into 9-methyl pyrido[3,4-*b*]indole (**9-MP**) by water molecules. In the moderate water content region the photoabsorption and the fluorescence band of **9-MP** gradually shift to longer wavelength region with the increase in the fluorescence intensity, can be ascribed to the formation of the hydrogen-bonded complex (**9-MP-H$_2$O**) with water molecules. Furthermore, in the high water content region two photoabsorption bands and the fluorescence band at longer wavelength region gradually reappear with a simultaneous decrease in the photoabsorption and the fluorescence band of **9-MP-H$_2$O**, which is attributed to the formation of the hydrogen-bonded proton transfer complex (**9-MP-H+**) with water molecules. Thus, this work demonstrates that pyrido[3,4-*b*]indole-boron trifluoride complex can act as a colorimetric and ratiometric fluorescent sensor for the detection of water over a wide range from low water content to high water content in solvents.

Acknowledgements

Chapter 5-1 is reproduced from "Colorimetric and ratiometric fluorescence sensing of water based on 9-methyl pyrido[3,4-*b*]indole-boron trifluoride complex; T. Enoki and Y. Ooyama, *Dalton Trans.*, **2019**, DOI: 10.1039/C8DT04527E, in press." with permission from The Royal Society of Chemistry.

Chapter 5-2

Development of the julolidine-structured pyrido[3,4-*b*]indole-boron trifluoride complex as a intramolecular charge transfer-type colorimetric and fluorescence sensor for water

Introduction

In Chapter 5-1, the author demonstrated that the *β*-carboline-boron trifluoride complex **9-MP-BF_3** can act as the ICT-type colorimetric and fluorescence sensors for water. **9-MP-BF_3** showed photoabsorption and fluorescence spectral change which is attributed to the dissociation of the **9-MP-BF_3** into **9-MP** by water molecule, formation of the hydrogen-bonded complex **9-MP-H_2O** and formation of the hydrogen-bonded proton transfer complex **9-MP-H+** in low (0-2 wt%), moderate (2-40 wt%) and high (40-80 wt%) water content region, respectively (Figure 1a). This result indicated that the *β*-carboline-boron trifluoride complexes are promising candidate of the optical sensor skeleton for water in wide range from low to high water content region. However, the detection limit (DL) of **9-MP-BF_3** in inferior to those of the reported ICT-type and PET-type fluorescence sensors. In this chapter, to gain further insight into the optical sensing properties of *β*-carboline-boron trifluoride complex for water in solvent, the author have newly designed and developed julolidine-structured pyrido[3,4-*b*]indole-boron trifluoride complex **ET-1-BF_3** as a colorimetric and fluorescence sensor for water (Figure 1b). In Chapter 4, the author demonstrated that the julolidine-structured *β*-carboline derivative **ET-1** can form the Py(N)-B complex with boron trifluoride, and the Py(N)-B complex possess strong photoabsorption and fluorescence properties in visible light region (Figure 1b). Thus, it was expected that **ET-1-BF_3** can act as a sensitive colorimetric and fluorescence sensor for water. Based on not only the photoabsorption and fluorescence

spectral measurements of **ET-1-BF$_3$** in solvents that contained various concentrations of water, but also the ^{1}H NMR spectral measurements of **ET-1-BF$_3$** with and without the addition of water in the solution, the author has investigated the optical sensing ability and sensing mechanisms of **ET-1-BF$_3$** for detection of water over a wide range from low water content to high water content in solvents.

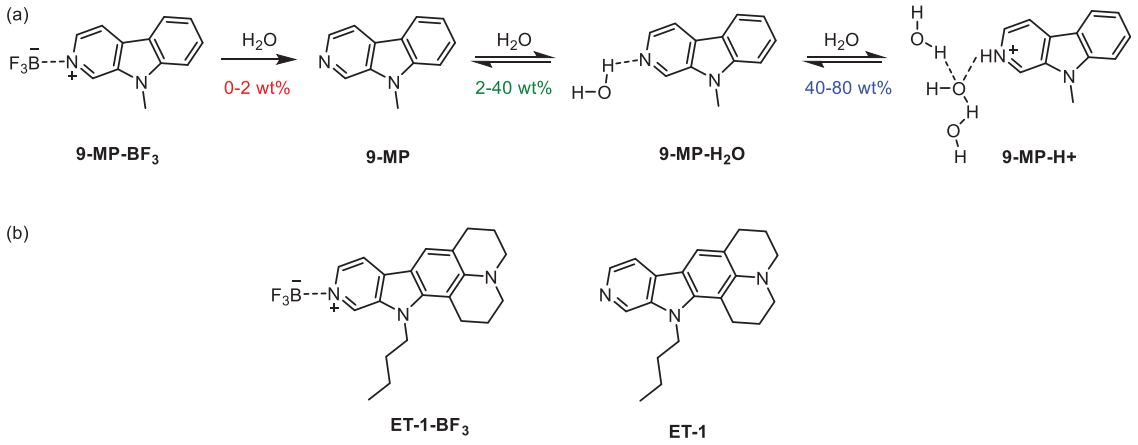

Figure 1. (a) Proposed mechanisms of colorimetric and ratiometric fluorescent sensor **9-MP-BF$_3$** for the detection of water in solvent. (b) Chemical structures of **ET-1-BF$_3$** and **ET-1**.

Experimental

General

Melting points were measured using a Yanaco micro melting point apparatus MP model. IR spectra were recorded on a SHIMADZU IRAffinity-1 spectrometer using the ATR method. High-resolution mass spectral data were acquired using a Thermo Fisher Scientific LTQ Orbitrap XL. ^{1}H NMR and ^{13}C NMR and ^{11}B NMR spectra were recorded using Varian-400 (400 MHz) and Varian-500 (500 MHz) FT NMR spectrometer. Absorption spectra were recorded using a Shimadzu UV-3150 spectrophotometer and fluorescence spectra were recorded using a HITACHI f-4500 fluorescence spectrometer. The determination of water in acetonitrile solution was done with a MKC-610 and MKA-610 Karl Fischer moisture titrator (Kyoto Electronics manufacturing Co., Ltd.) based on Karl Fischer coulometric titration (relative standard deviation is below 0.3% in a measurement of propylene carbonate containing 1 mg water) for below 1.0 wt% and volumetric titration for above 1.0 wt%, respectively.

Synthesis

13-Butyl-2,3,5,6,7,13-hexahydro-1*H*-pyrido[3,2,1*ij*]pyrido[4',3':4,5]pyrrolo[2,3-*f*]quinoline-boron trifluoride complex (ET-1-BF$_3$). To a solution of **ET-1** (0.03 g, 0.09 mmol) in 6 mL of Et_2O was added dropwise 47% BF_3-OEt_2 (0.09 mmol) diluted with ether (2 ml) for 30 min, and then the solution was stirred for 4h at room temperature. The resulting precipitate was filtered and was washed by Et_2O to give **ET-1-BF$_3$** (0.03 g, yield 43 %) as a yellow solid; mp: 157-158°C; IR (ATR): $\tilde{\nu}$ = 1611, 1437, 1030 cm^{-1}; ^{1}H NMR (400 MHz, CD_3CN): δ = 0.98 (t, J = 7.4 Hz, 3H), 1.38-1.42 (m, 2H), 1.72-1.82 (m, 2H), 2.00-2.04 (m, 4H, overlapping peak of residual proton in CD_3OD) 2.88 (t, J = 6.2 Hz, 2H), 3.20 (t, J = 6.4 Hz, 2H), 3.31-3.38 (m, 4H), 4.48 (t, J = 7.8 Hz), 7.66 (s, 1H), 7.95

(d, J = 6.2 Hz, 1H), 8.08 (d, J = 6.2 Hz, 1H), 8.51 (s, 1H) ppm (one aliphatic proton signal was not observed owing to overlapping resonances); ^{13}C NMR (125 MHz, CD_3CN): δ = 13.96, 20.57, 21.68, 22.22, 23.99, 46.85, 50.36, 51.77, 102.23, 110.82, 113.29, 121.40, 121.41, 121.83, 129.62, 135.69, 137.28, 145.37, 148.99 ppm, ^{11}B MNR (160 MHz, CD_3CN): δ = –1.13 ppm, HRMS (ESI): m/z (%): [M + H^+] calcd for $C_{22}H_{25}N_3$, 320.21212 ; found 320.21240.

Results and Discussion

The β-carboline-boron trifluoride complex **ET-1-BF$_3$** ware effectively prepared by treating corresponding β-carboline derivative with BF_3-OEt_2 and characterized by ^{1}H NMR, ^{13}C NMR, ^{11}B NMR, FT-IR and high-resolution mass analysis.

The photoabsorption and fluorescence spectra of **ET-1** and **ET-1-BF$_3$** in acetonitrile are shown in Figure 2. The photoabsorption maxima of **ET-1** and **ET-1-BF$_3$** were observed at 365 nm and 436 nm respectively, which are attributed to the ICT excitation from the electron-donating (julolidine) moiety to the electron-withdrawing (pyridine and pyridine-boron trifluoride unit for **ET-1** and **ET-1-BF$_3$**, respectively) moiety. Thus, photoabsorption maxima of **ET-1-BF$_3$** was observed at longer wavelength region by 71 nm than that of **ET-1** because of the strong electron-withdrawing ability of the pyridine-boron trifluoride unit of **ET-1-BF$_3$**. The molar excitation coefficient value (ε) of **ET-1-BF$_3$** (25900 M^{-1} cm^{-1}) is higher than that of **ET-1** (19900 M^{-1} cm^{-1}). In addition, the corresponding fluorescence band of **ET-1** and **ET-1-BF$_3$** appears at 411 nm and 507 nm, respectively, and the fluorescence quantum yield (Φ_f) of **ET-1-BF$_3$** (0.65) is higher than that of **ET-1** (0.38). Thus, the complexation between the pyridyl moiety of **ET-1** and boron trifluoride can lead to not only the red-shift of the photoabsorption and fluorescence band but also the increase in ε and Φ_f values.

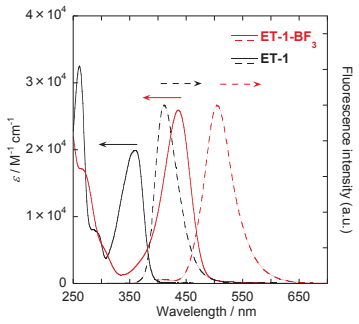

Figure 2. Photoabsorption and fluorescence spectra of **ET-1** and **ET-1-BF$_3$** in acetonitrile (λ_{ex} = 310 and 382 nm for **ET-1** and **ET-1-BF$_3$**, respectively)

In order to investigate the optical sensing ability of **ET-1** and **ET-1-BF_3** for water in solvent, the photoabsorption and fluorescence spectral measurements in acetonitrile with various concentration of water were carried out (Figure 3 and 4). For **ET-1**, photoabsorption band at around 360 nm gradually increased with a slight red-shift with increase in water content from 2.9 to 11 wt%, and the isosbestic point was observed at 298 and 354 nm (Figure 3b). This spectral change can be ascribed to the formation of the hydrogen-bonded complex (**ET-1-H_2O**) between the nitrogen atom on pyridine ring and hydroxy group of water molecule. In addition, in the water content region above 11 wt%, photoabsorption band at around 360 nm showed a decrease and red-shift with simultaneous increase in a new photoabsorption band at around 430 nm (Figure 3c). The new absorption band at around 430 nm is assignable to the ICT band of the hydrogen-bonded PTC (**ET-1-H**+) formed by the proton transfer from water molecule to the pyridinic nitrogen atom on *β*-carboline skeleton. Moreover, red-shift of photoabsorption band at around 360 nm were observed in water content region below water content of 40 wt%. This spectral change indicated that the formation of the hydrogen-bonded complex and subsequent formation of the hydrogen-bonded PTC were proceeded in the water content range from 11 to 40 wt%. On the other hand, the fluorescence band of **ET-1** at around 420 nm showed a red-shift and gradually increased by addition of water in water content range from 1.0 to 11 wt% (Figure 3e). It is ascribed to formation of the **ET-1-H_2O**. In the high water content region above 11 wt%, the fluorescence band at around 420 nm decreased with simultaneous appearance and increase of a fluorescence band at around 510 nm with isoemissive point at 475 nm (Figure 3f). This result strongly indicated that the hydrogen-bonded PTC was generated in the excited state in water content region above 11 wt%. Consequently, as is the case with **9-MP**, the julolidine-

structured *β*-carboline derivative **ET-1** change its photoabsorption and fluorescence properties through the formation of the hydrogen-bonded complex and the hydrogen-bonded PTC in low (from 2.9 to 40 wt% in the ground state and from 1.0 to 11 wt% in the excited state) and high (above 11 wt% in both the ground state and the excited state) water content region, respectively. However, it is noteworthy that **ET-1** can form the hydrogen-bonded PTC in lower water content region compared to **9-MP**[9] (above water content of 40 wt%) because the electron-donating characteristics of the julolidine moiety enhance the basicity of pyridinic nitrogen atom on the *β*-carboline skeleton of **ET-1**, which promotes the formation of the hydrogen-bonded PTC between **ET-1** and water molecules.

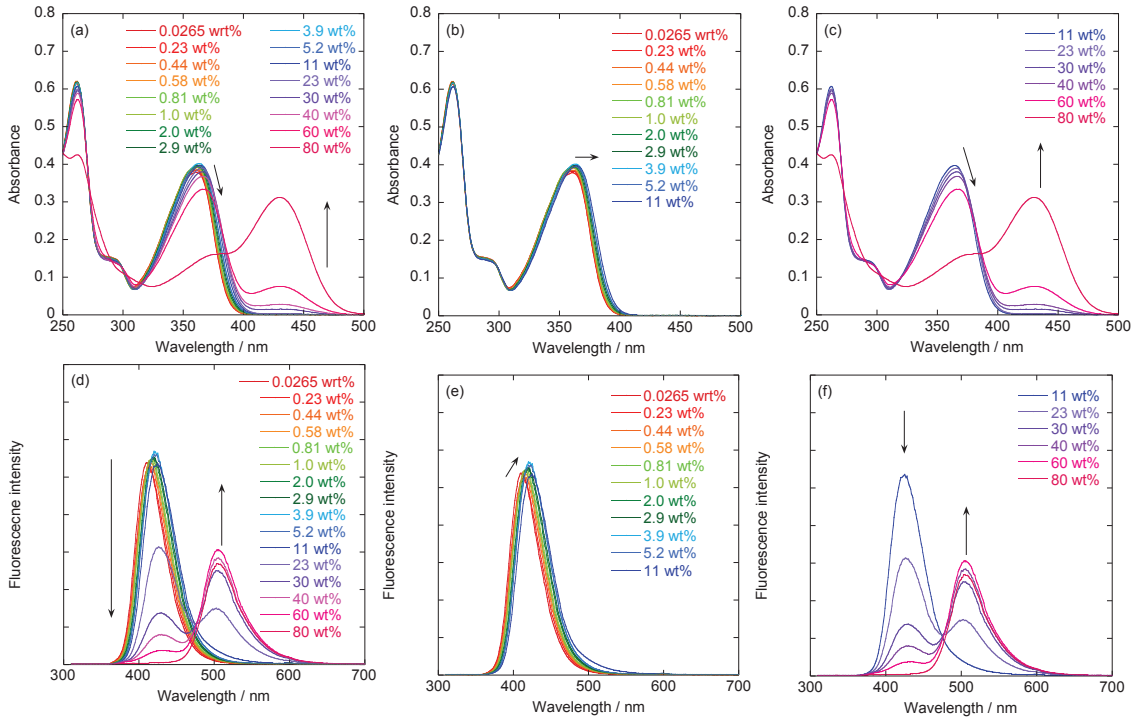

Figure 3. Photoabsorption spectra of **ET-1** ($c = 2.0 \times 10^{-5}$ M) in acetonitrile containing water (a) 0.0265–80 wt%, (b) 0.0265-11 wt% (c) 11-80 wt%. Fluorescence spectra of **ET-1** in acetonitrile containing water (d) 0.0265–80 wt% (e) 0.0265-11 wt% (f) 11-80 wt% ($c = 2.0 \times 10^{-5}$, $\lambda_{ex} = 302$ nm).

On the other hand, the photoabsorption and fluorescence spectral change for **ET-1-BF_3** upon the addition of water was more complicated compared with **ET-1**. In acetonitrile with water content of 0.0201 wt%, there are big difference in photoabsorption and fluorescence spectra between the two solutions which are stored in dark for 10 min and 1 day after the solutions were prepared (Figure 4a and 4e). For the solution stored in dark for 1 day, photoabsorption band at around 430 nm and fluorescence band at around 510 nm decreased, and photoabsorption band at around 360 nm and fluorescence band at around 430 nm increased compared to the solution stored in dark for 10 minutes. This fact indicated that the time-dependent spectral change is attributed to the dissociation of **ET-1-BF_3** into **ET-1** by water molecule and the reaction rate is not so fast. Thus, we have evaluated the optical sensing ability of **ET-1-BF_3** for water by measuring the photoabsorption and fluorescence spectra for **ET-1-BF_3** solution with various concentrations of water which is stored in dark 1 day after they were prepared. In the low water content range from 0.0201 to 4.2 wt%, photoabsorption band at around 430 nm drastically decreased with simultaneous increase of a new photoabsorption band at around 360 nm, which is originating from **ET-1** (Figure 4b). This result indicated that **ET-1** was produced as a result of the dissociation of **ET-1-BF_3** into **ET-1** by water with increase in water content. In high water content region above 11 wt%, the photoabsorption band at around 360 nm was decreased with reappearance of the photoabsorption band at around 430 nm, which is attributed to formation of **ET-1-H+** (Figure 4c). Moreover, in water content range from 2.4 to 40 wt%, the photoabsorption band at around 360 nm gradually shifts to longer wavelength region with increase in water content. Thus, the hydrogen-bonded complex **ET-1-H_2O** was formed in the water content range from 2.4 to 40 wt%. The isosbestic points were observed at 272 and 293 nm, and 272, 305 and 386 nm in the

water content range from 0.0201 to 2.4 wt% and from 40 to 80 wt%, respectively. For the corresponding fluorescence spectra (Figure 4d-4f), the fluorescence band of **ET-1-BF$_3$** at around 510 nm was decreased with increase in the fluorescence band originating from **ET-1** at around 420 nm in the low water content region below 11 wt% (Figure 4e). In addition, the fluorescence band at around 420 nm gradually shifted to longer wavelength region with increase in water content in the water content range from 1.1 to 11 wt%. It is obviously showed the formation of **ET-1-H$_2$O**. In high water content region above 11 wt%, the fluorescence band at around 420 nm was decreased with reappearance of the fluorescence band at around 510 nm with the isoemissive point at 475 nm, which can be assignable to the fluorescence band of **ET-1-H+** (Figure 4f).

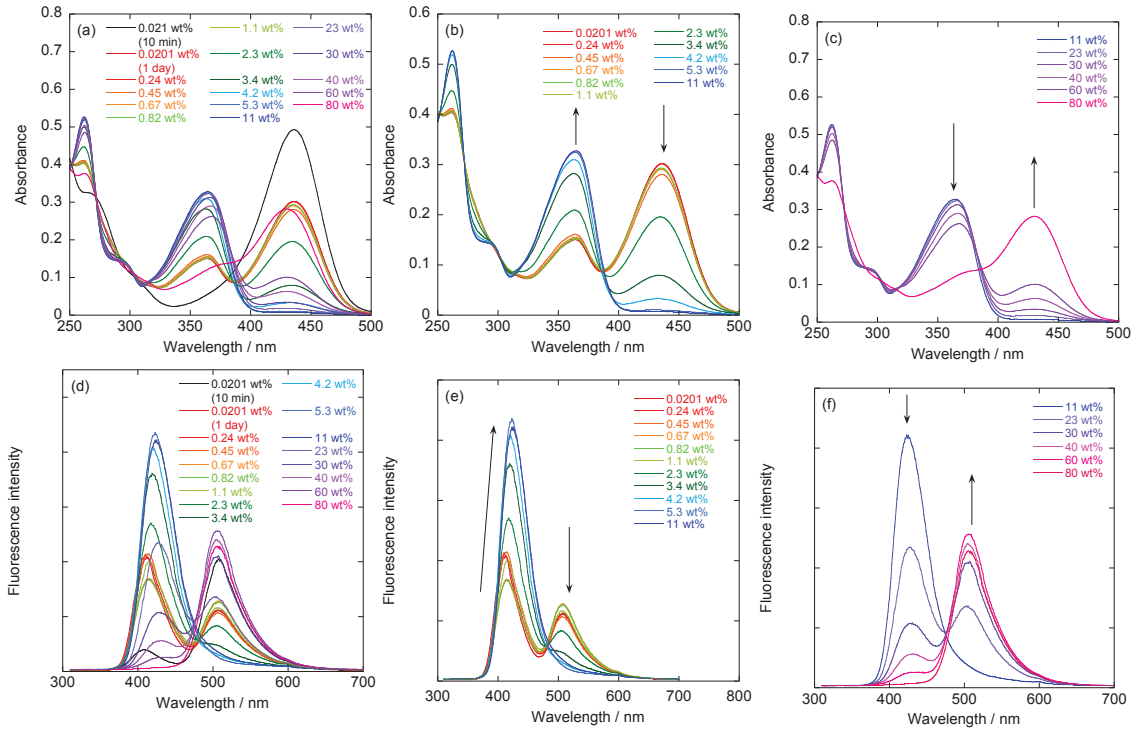

Figure 4. Photoabsorption spectra of ET-1-BF$_3$ (c = 2.0 × 10^{-5} M) in acetonitrile containing water (a) 0.0265-80 wt%, (b) 0.0265-11 wt%, and (c) 11-80 wt%. Fluorescence spectra of ET-1-BF$_3$ in acetonitrile containing water (d) 0.0265-80 wt%, (e) 0.0265-11 wt% and (f) 11-80 wt% (c = 2.0×10^{-5}, λ_{ex} = 302 nm).

To estimate the optical sensing ability of the two dyes, the absorbance and fluorescence intensity were plotted against the water content for **ET-1** (Figure 5) and **ET-1-BF$_3$** (Figure 6). For **ET-1**, the plot for the low water content region below 11 wt% showed that there is little change in the absorbance intensity at around 360 (A_{360}) and 430 (A_{430}) nm with increase in water content (Figure 5b). In high water content region above 11 wt% A_{360} decreased linearly as a function of the water content, but A_{430} increased linearly as a function of water content (Figure 5c). The slope of the plot (m_s) and correlation coefficient (R^2) values for the calibration curve are –0.001 and 0.97 for A_{360}, and 0.002 and 0.91 for A_{430}, respectively. In addition, the fluorescence peak intensity at around 420 (Fl_{420}) and 510 (Fl_{510}) nm gradually increased with increase in the water content due to the enhancement and red-shift of the fluorescence band at around 420 nm by formation of **ET-1-H$_2$O** (Figure 5e). The m_s and R^2 values for Fl_{510} are 2.3 and 0.99, respectively, which shows good linearity. Moreover, the plots of fluorescence intensity for the high water content region above 11 wt% demonstrated that Fl_{510} increased with decrease in Fl_{420} (Figure 5h). The linear relationship was observed between the fluorescence intensity and the water content in the water content range from 11 wt% to 40 wt%. The m_s and R^2 are –16 and 0.95 for Fl_{420} and 9.0 and 0.95 for Fl_{510}, respectively. In addition, we have estimated the detection-limit (DL = $3.3s/m_s$ where s is the standard deviation of the blank sample and m_s is the slope of the calibration curve) for **ET-1** to 1.4 wt% from the m_s value for Fl_{510} (2.3) in the water content region below 11 wt%. This DL value is inferior to those of the reported ICT-type and PET-type fluorescence sensors. However, the photoabsorption and fluorescence spectral measurements revealed that the julolidine-structured β-carboline derivative **ET-1** can act as a colorimetric and fluorescence sensor for water over wide range from low to high water concentration because the plots of the

absorbance and fluorescence intensity against the water content showed good linearity over wide range of water concentration (ca. 10-60 wt% for absorbance and ca. 0-10 wt% and 10-40 wt% for fluorescence intensity) (Figure 5).

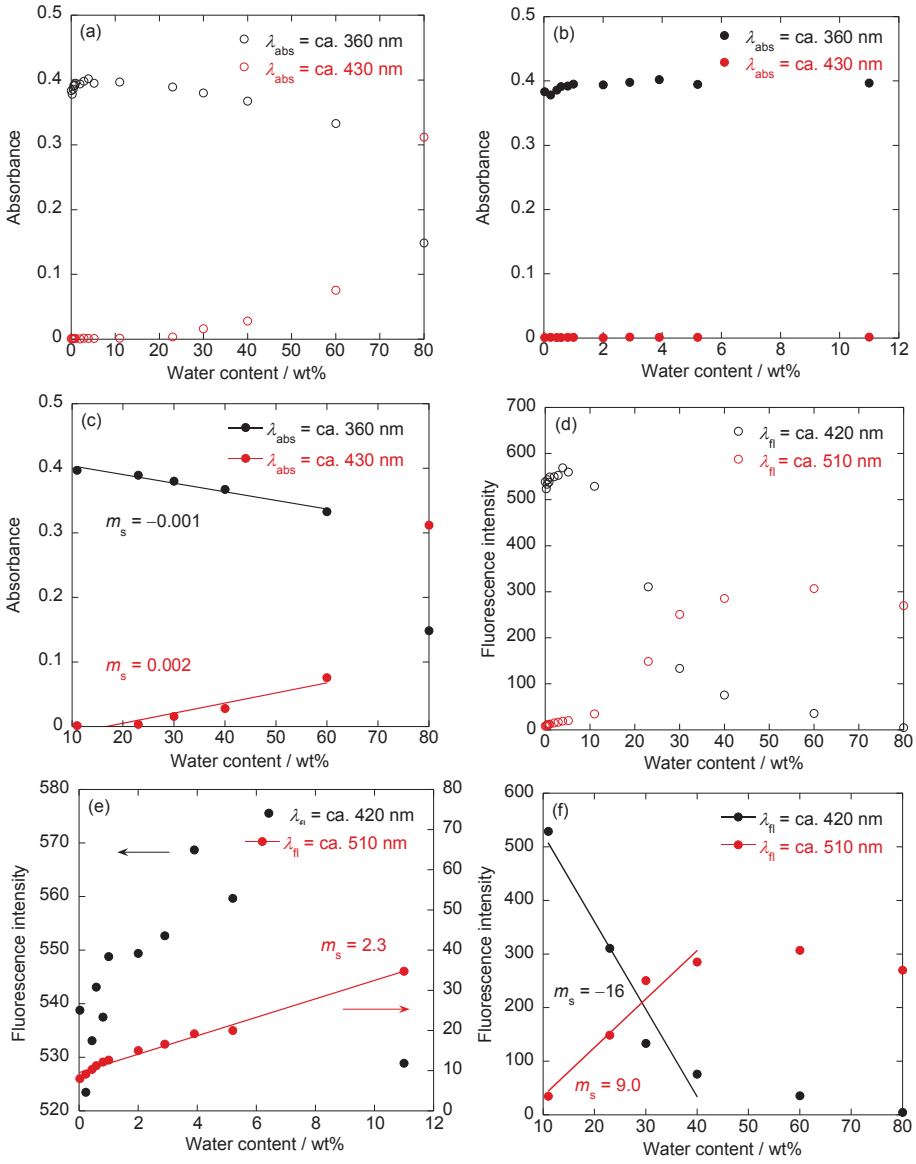

Figure 5. Absorbance of **ET-1** at around 360 and 430 nm as a function of water content from (a) 0.0201-80 wt%, (b) 0.0201-11 wt% and (c) 11-80 wt%. Fluorescence peak intensity of **ET-1** at around 420 and 510 nm by photoexcitation at 302 nm as a function of water content from (d) 0.0201-80 wt%, (e) 0.0201-11 wt% (f) 11-80 wt%

For **ET-1-BF$_3$**, there are big difference in absorbance and fluorescence intensity against the water content in low water content region below ca. 10 wt% (Figure 6a and 6e). Moreover, it is worth mentioning here that the threshold of photoabsorption (fluorescence) enhancement (decline) was observed in the water content at ca. 1 wt% (Figure 6b and 6f) because the dissociation of **ET-1-BF$_3$** by water undergoes slowly so that the reaction had not completely proceeded. Indeed, the threshold was not observed for the solution which is stored in dark for two days (Figure 7). The plots of absorbance for the water content range from 1.1 wt% to 4.2 wt% revealed that A_{360} increased linearly with increase in water content, but A_{430} decreased linearly as a function of the water content. The m_s and R^2 values are 0.05 and 0.99, and –0.09 and 0.99 for A_{360} and A_{430}, respectively (Figure 6b). In the moderate water content range from 4.2 to 11 wt%, appreciable change was not observed in absorbance (Figure 6c). However, in high water content region above 11 wt%, it was found that A_{360} was decreased with simultaneous increase in A_{430} (Figure 6d). The plots showed good linearity in the water content range from 11 to 60 wt% (R^2 = 0.96 and 0.98 for A_{360} and A_{430}, respectively), and the m_s values for A_{360} and A_{430} were –0.002 and 0.002, respectively, which is similar to those of **ET-1** (Figure 5c). Moreover, the plots of the fluorescence intensity in the water content range from 1.1 wt% to 4.2 wt% demonstrated that Fl_{420} linearly increased with simultaneous decrease in Fl_{510} as a function of water content. The m_s values for Fl_{420} and Fl_{510} is 68 and –28, which are much larger than those of **ET-1**, and the plots showed good linearity (R^2 = 0.99 for Fl_{420} and Fl_{510}) (Figure 6f). Thus, **ET-1-BF$_3$** is expected to be a more sensitive fluorescence sensor for water compared to **ET-1**. However, it is difficult for **ET-1-BF$_3$** to estimate the DL value due to the presence of the threshold. In moderate water content range from 4.2 to 11 wt%, small increase in Fl_{420} was observed (Figure 6g). Moreover, as

is the case with **ET-1**, Fl_{510} increased linearly as a function of the water content with simultaneous decrease of Fl_{420} in the water content range from 11 wt% to 40 wt% (R^2 = 0.95 and 0.96 for Fl_{420} and Fl_{510}, respectively) (Figure 6h). The m_s values for Fl_{420} and Fl_{510} are −13 and 7.3, respectively, which shows good agreement with those of **ET-1** (Figure 5f).

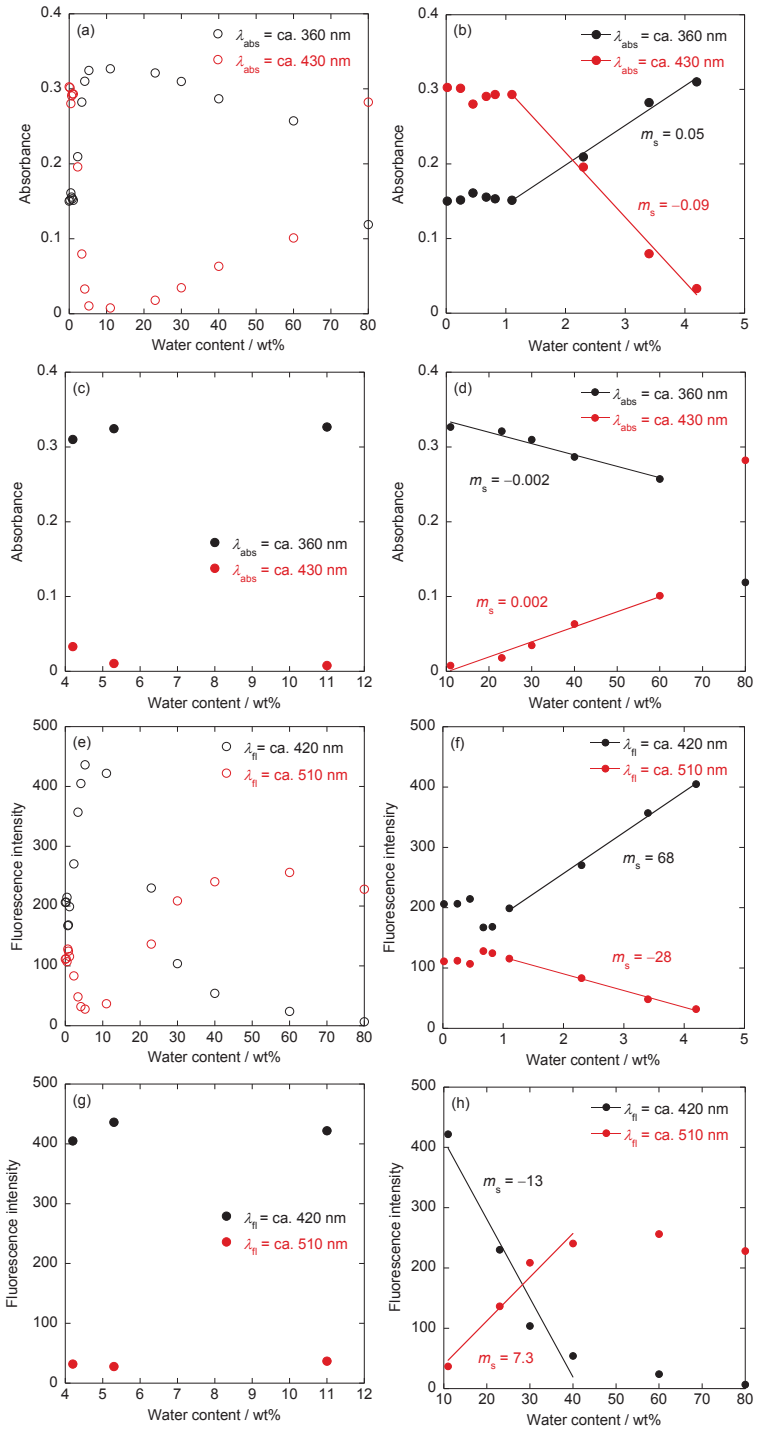

Figure 6. Absorbance of **ET-1-BF$_3$** at around 360 and 430 nm as a function of water content from (a) 0.0201-80 wt%, (b) 0.0201-4.2 wt%, (c) 4.2-11 wt% and (d) 11-80 wt%. Fluorescence peak intensity of **ET-1-BF$_3$** at around 420 and 510 nm by photoexcitation at 302 nm as a function of water content from (e) 0.0201-80 wt%, (f) 0.0201-4.2 wt% (g) 4.2-11 wt% and (h) 11-80 wt%

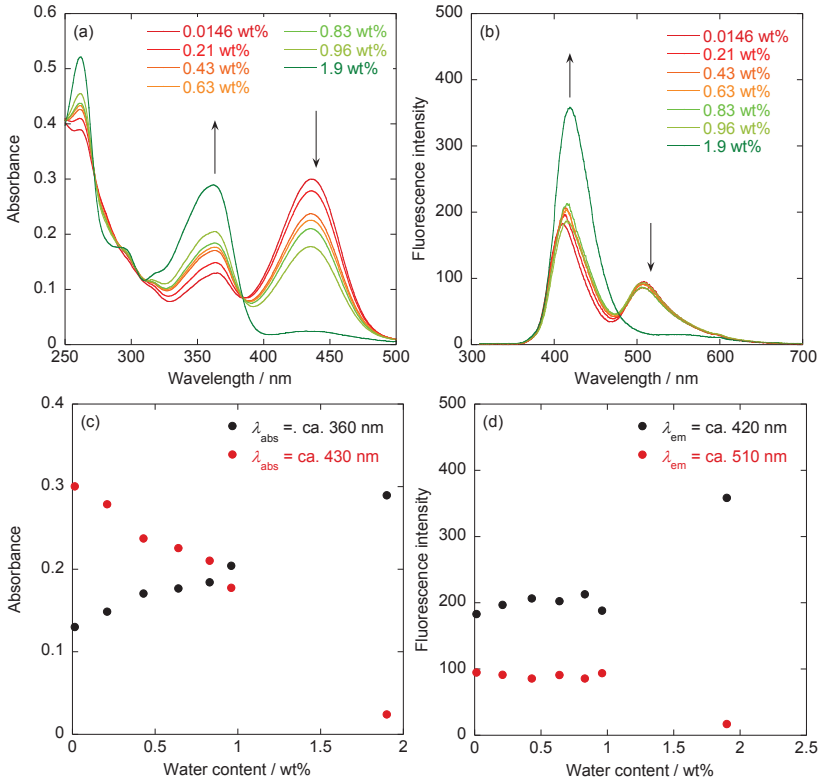

Figure 7. (a) Photoabsorption and (b) fluorescence spectra of **ET-1-BF$_3$** in in acetonitrile containing water (0.0146–1.9 wt%). (c) Absorbance at around 365 nm and 435 nm, and (d) fluorescence intensity at around 415 and 510 nm for **ET-1-BF$_3$** as a function of water content in acetonitrile in a water content range from 0.0146 to 1.9 wt%.

To elucidate the mechanism for the detection of water in the solvent, ^{1}H NMR spectral measurement were performed for the **ET-1** and **ET-1-BF$_3$** in CD_3CN with and without addition of 10 wt% of water (Figure 8). For the ^{1}H NMR spectra of **ET-1** and **ET-1-BF$_3$** without addition of water, the chemical shift of the aromatic protons for **ET-1-BF$_3$** (H_a-H_d) shows upfield shift for H_a and H_b, and downfield shift for H_c and H_d compared to those of **ET-1**, although there is little change for the aliphatic protons between the two dyes (Figure 8a and 8b). This ^{1}H NMR spectral change shows good agreement with the spectrum that BF_3-OEt_2 was added to **ET-1** solution. Thus, this result indicated that the preparation of the *β*-carboline-boron trifluoride complex **ET-1-BF$_3$**. Furthermore, ^{1}H

NMR spectrum of **ET-1** with a water content of 10 wt%, which corresponds to the maximum absorbance in the absorbance enhancement process of photoabsorption band at around 360 nm and the minimum absorbance in the absorbance decline process of photoabsorption band at around 420 nm were shown in Figure 8c. This spectrum is close to that of **ET-1** with water content of 10 wt% (Figure 8d), which is on the process of gradual red-shift of photoabsorption spectra at around 360 nm due to the formation of **ET-1-H_2O**. Thus, the blue-shift of the photoabsorption band in the water content region below ca. 10 wt% for **ET-1-BF_3** is attributed to the dissociation of the **ET-1-BF_3** into **ET-1** and subsequent formation of **ET-1-H_2O**. From the photoabsorption, fluorescence and ^{1}H NMR spectral measurements, the expected mechanisms of **ET-1-BF_3** for detection of water in solvent were shown in Figure 9. In the water content region below ca. 10 wt%, drastic decrease in the photoabsorption band at around 420 nm and fluorescence band at around 510 nm with simultaneous increase in the new photoabsorption band at around 360 nm and fluorescence band at around 420 nm were attributed to the dissociation of **ET-1-BF_3** into **ET-1** by water. In the moderate water content region, the gradual red-shift of photoabsorption band at around 360 nm (from ca. 2 wt% to ca. 40 wt%) and fluorescence band at around 420 nm (from ca. 1 wt% to ca. 10 wt%) can be assignable to the formation of hydrogen-bonded complex (**ET-1-H_2O**). In high water content region above ca. 10 wt%, decrease in photoabsoption band at around 360 nm and fluorescence band at around 430 nm occurred with simultaneous increase in photoabsorption band at around 420 nm and fluorescence band at around 510 nm, which is ascribed to formation of hydrogen bonded PTC (**ET-1-H+)**. Thus, this work demonstrated that the julolidine-structured β-carboline-boron trifluoride complex can work as a colorimetric and fluorescence water sensor based on the changing of ICT characteristics for both low and

high water content region. Indeed, as shown in Figure 8, the color of **ET-1-BF$_3$** solution turned from yellow to colorless due to the dissociation of **ET-1-BF$_3$** into **ET-1** and subsequent formation of **ET-1-H$_2$O.** Then, turned yellow again as a result of the formation of **ET-1-H+**. In addition, the fluorescence color also changed in the order of light blue, blue and green with increase in the water content.

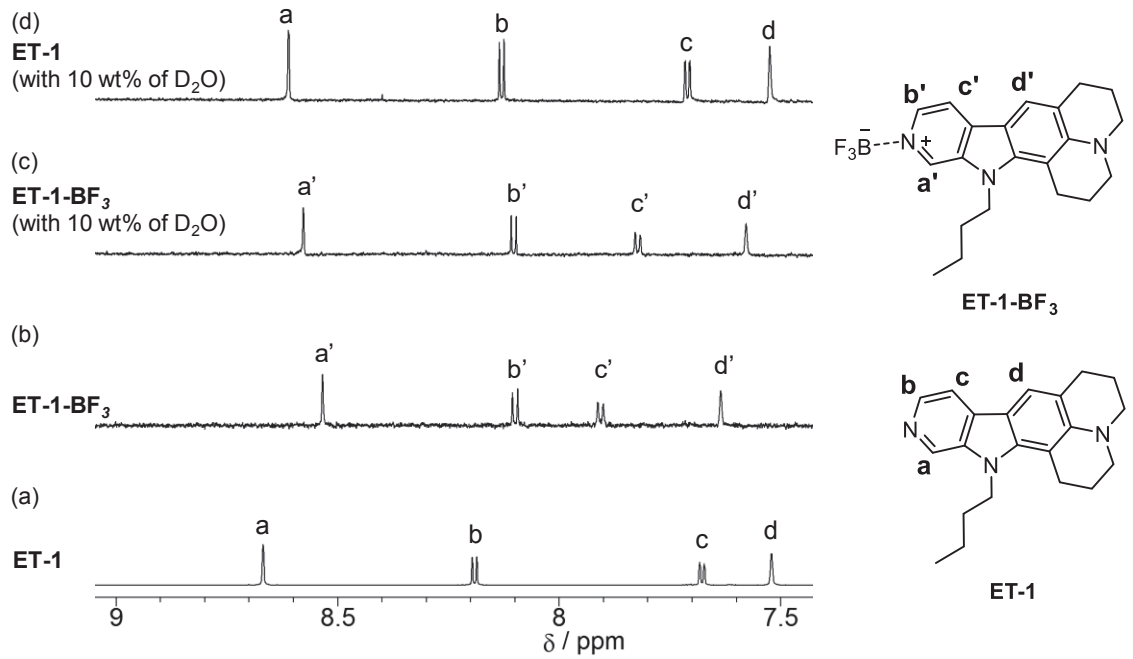

Figure 8. ^{1}H NMR spectra of (a) **ET-1** and (b) **ET-1-BF$_3$** in CD_3CN. ^{1}H NMR of (c) **ET-1** and (d) **ET-1-BF$_3$** in CD_3CN with 10 wt% of D_2O (c = 1.0 × 10^{-4} M).

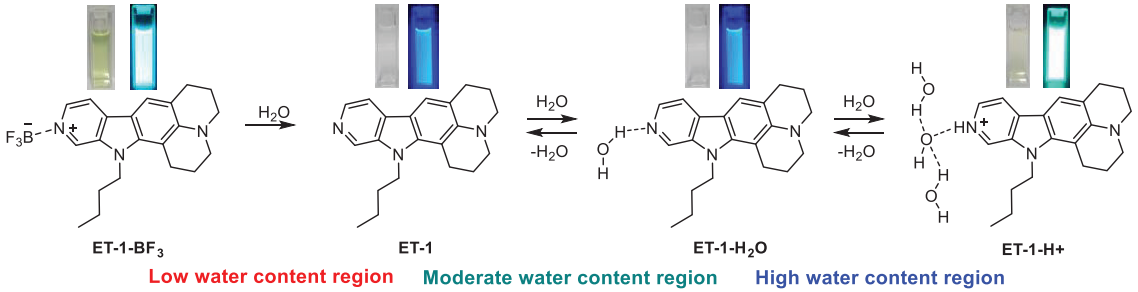

Figure 9. Proposed mechanisms of the colorimetric and fluorescent sensor **ET-1-BF$_3$** for the detection of water in solvents; inset: color (left) and fluorescence color (right) images.

Conclusion

The julolidine-structured *β*-carboline-boron trifluoride complex **ET-1-BF_3** have been developed as a colorimetric and fluorescence sensor for water in acetonitrile. **ET-1-BF_3** showed red-shift in photoabsorption and fluorescence spectra compared to julolidine-structured *β*-carboline derivative **ET-1** in absolute acetonitrile. In addition, it was found that **ET-1-BF_3** showed blue-shift in the photoabsorption and fluorescence spectra due to the dissociation of **ET-1-BF_3** into **ET-1** by addition of water in the water content region below ca. 4 wt%. In the moderate water content range from ca. 4 wt% to 10 wt%, dissociation of **ET-1-BF3** into **ET-1** and formation of the hydrogen-bonded complex (**ET-1-H_2O**) between **ET-1** and water molecule were subsequently proceeded. Thus, gradual red-shift and increase in fluorescence band at around 430 nm were observed. In high water content region above ca. 10 wt%, reappearance of the photoabsorption and fluorescence band in longer wavelength region were observed as a result of formation of the hydrogen-bonded PTC **ET-1-H+**. Moreover, **ET-1** form the hydrogen-bonded PTC with water molecule in lower water content region (above ca. 10 wt%) compared to 9-methyl-pyrido[3,4,*b*]indole (**9-MP**) (above ca. 40 wt%) because the electron-donating characteristics of the julolidine moiety enhance the basicity of pyridinic nitrogen atom on the *β*-carboline skeleton of **ET-1**, leading to the promotion of the formation of the hydrogen-bonded PTC between **ET-1** and water molecule. Consequently, this work demonstrated that the julolidine-structured *β*-carboline-boron trifluoride complexes possess potential application as a colorimetric and fluorescence water sensor for water over wide range of water content.

Reference

1. H. S. Jung, P. Verwilst, W. Y. Kim and J. S. Kim, *Chem. Soc. Rev.*, **2016**, *45*, 1242.

2. J. Lee, M. Pyo, S. Lee, J. Kim, M. Ra, W.-Y. Kim, B. J. Park, C. W. Lee and J.-M. Kim, *Nat*. *Commun*., **2014**, *5*, 3736.

3. A. Douvali, A. C. Tsipis, S. V. Eliseeva, S. Petoud, G. S. Papaefstathiou, C. D. Malliakas, I. Papadas, G. S. Armatas, I. Margiolaki, M. G. Kanatzidis, T. lazarides and M. J. Manos, *Angew*. *Chem*. *Int*. *Ed*., **2015**, *54*, 1651.

4.W.-E. Lee, Y.-J. Jin, L.-S. Park and G. Kwak, *Adv*. *Mater*., **2012**, *24*, 5604.

5. (*a*) Q. Deng, Y. Li, J. Wu, Y. Liu, G. Fang, S. Wang and Y. Zhang, *Chem*. *Commun*., **2012**, *48*, 3009; (*b*) L. Ding, Z. Zhang, X. Li and J. Su, *Chem*. *Commun*., **2013**, *49*, 7319; (*c*) M. Tanioka, S. Kamino, A. Muranaka, Y. Shirasaki, Y. Ooyama, M. Ueda, M. Uchiyama, S. Enomoto and D. Sawada, *Phys. Chem. Phys. Chem.*, **2017**, *19*, 1209; (*d*) D. Wang, H. Zhao, H. Li, S. Sun and Y. Xu, *J. Mater*. *Chem. C*, **2016**, *4*, 11050; (*e*) S. Guo, Y. Ma, S. Li, Q. Yu, A. Xu, J. Han, L. Wei, Q. Zhao and W. Huang, *J. Mater. Chem. C*, **2016**, *4*, 6110; (*f*) Y. Dong, J. Cai, Q. Fang, X. You and Y. Chi, *Anal. Chem*., **2016**, *88*, 1748; (*g*) Y. Huang, W. Liu, H. Feng, Y. Ye, C. Tang, H. Ao, M. Zhao, G. Chen, J. Chen and Z. Qian, *Anal. Chem*., **2016**, *88*, 7429; (h) P. Kumar, R. Kaushik, A. Ghosh and A. Jose, *Anal. Chem*., **2016**, *88*, 11314.

6. Y. Zhang, C. Liarg and S. Jiang, *New J. Chem*., **2017**, *41*, 8644.

7. (*a*) A. Wang, R. Fan, Y. Dong, Y. Song, Y. Zhou, J. Zheng, X. Du, K. Xing and Y. Yang, *ACS Appl*. *Mater*. *Interfaces*, 2017, **9**, 15744; (*b*) A. Wang, R. Fan, Y. Dong, W. Chen, Y. Song, P. Wang, S. Hao, Z. Liu and Y. Yang, *Dalton Trans*., **2017**, *46*, 71; (*c*) A. Wang, R. Fan, P. Wang, R. Fang, S. Hao, X. Zhou, X. Zheng and Y. Yang, *Inorg*. *Chem*., **2017**, *56*, 12881.

8. H.-L. Qian, C. Dai, C.-X. Yang and X.-P. Yan, *ACS Appl*. *Mater*. *Interfaces*, **2017**, *9*, 24999.

9. (*a*) P. Kumar, R. Sakla, A. Ghosh and D. A. Jose, *ACS Appl. Mater. Interfaces*, **2017**, *9*, 25600; (*b*) S. Song, Y. Zhang, Y. Yang, C. Wang, Y. Zhou, C. Zhang, Y. Zhao, M. Yang and Q. Lin, *Analyst*, **2018**, *143*, 3068; (*c*) E. Poonia, P. K. Mishra, V. Kiran, J. Sangwan, R. Kumar, P. K. Rai and V. K. Tomer, *Dalton Trans*., **2018**, *47*, 6293; (*d*) H. Yan, S. Guo, F. Wu, P. Yu, H. Liu, Y. Li and L. Mao, *Angew*. *Chem*. *Int*. *Ed*., **2018**, *57*, 3922.

10. (*a*) Y. Zhou, G. Baryshnikov, X. Li, M. Zhu, H. Ågren, and L. Zhu, *Chem*. *Mater*., **2018**, *30*, 8008; (*b*) J. Wei, H. Li, Y. Yuan, C. Sun, D. Hao, G. Zheng and R. Wang, *RSC Adv*., **2018**, *8*, 37028; (*c*) S. Song, Y. Zhang, Y. Yang, C. Wang, Y. Zhou, C. Zhang, Y. Zhao, M. Yang and Q. Lin, *Analyst*, **2018**, *143*, 3068.

11. (*a*) D. Citterio, K. Minamihashi, Y. Kuniyoshi, H. Hisamoto, S. Sasaki and K. Suzuki, *Anal. Chem*., **2001**, *73*, 5339; (*b*) C.-G. Niu, A.-L. Guan, G.-M. Zeng, Y.-G. Liu, Z.-W. Li, *Anal. Chim*. *Acta*, **2006**, *577*, 264; (*c*) C.-G. Niu, P.-Z. Qin, G.-M. Zeng, X.-Q. Gui, A.-L. Guan, *Anal. Bioanal. Chem*., **2007**, *387*, 1067; (*d*) Z.-Z. Li, C.-G. Niu, G.-M. Zeng and P.-Z. Qin, *Chem*. *Lett*., **2009**, *38*, 698; (*e*) Z. Li, Q. Yang, R. Chang, G. Ma, M. Chen and W. Zhang, *Dyes. Pigm*., **2011**, *88*, 307; (*f*) Y. Zhang, D. Li, Y. Li and J. Yu, *Chem. Sci.*, **2014**, *5*, 2710; (*g*) W. Chen, Z. Zhang, X. Li, H. Ågren and J. Su, *RSC Adv*., **2015**, *5*, 12191.

12. S. Tsumura, T. Enoki and Y. Ooyama, *Chem*. *Commun*., **2018**, *54*, 10144.

13. (*a*) Y. Ooyama, M. Sumomogi, T. Nagano, K. Kushimoto, K. Komaguchi, I. Imae and Y. Harima, *Org. Biomol. Chem.*, **2011**, *9*, 1314; (*b*) Y. Ooyama, A. Matsugasako, T.

Nagano, K. Oka, K. Kushimoto, K. Komaguchi, I. Imae and Y. Harima, *J. Photochem. Photobiol. A*: Chemistry, **2011**, *222*, 52.

14. (*a*) Y. Ooyama, A. Matsugasako, K. Oka, T. Nagano, M. Sumomogi, K. Komaguchi, I. Imae and Y. Harima, *Chem. Commun.*, **2011**, *47*, 4448; (*b*) Y. Ooyama, A. Matsugasako, Y. Hagiwara, J. Ohshita and Y. Harima, *RSC Adv.*, **2012**, *2*, 7666; (*c*) Y. Ooyama, K. Uenaka, A. Matsugasako, Y. Harima and J. Ohshita, *RSC Adv.*, **2013**, *3*, 23255; (*d*) Y. Ooyama, K. Furue, K. Uenaka and J. Ohshita, *RSC Adv.*, **2014**, *4*, 25330; (*e*) Y. Ooyama, S. Aoyama, K. Furue, K. Uenaka and J. Ohshita, *Dyes Pigm.*, **2015**, *123*, 248; (*f*) Y. Ooyama, M. Hato, T. Enoki, S. Aoyama, K. Furue, N. Tsunoji and J. Ohshita, *New J. Chem.*, **2016**, 40, 7278; (*g*) Y. Ooyama, R. Nomura, T. Enoki, R. Sagisaka, N. Tsunoji and J. Ohshita, *ChemistrySelect*, **2017**, *2*, 7765; (*h*) Y. Ooyama, R. Sagisaka, T. Enoki, N. Tsunoji and J. Ohshita, *New J. Chem.*, **2018**, *42*, 13339.

15. (*a*) W. Liu, Y. Wang, W. Jin, G. Shen and R. Yu, *Anal. Chim. Acta*, **1999**, *383*, 299; (*b*) H. Mishra, V. Misra, M. S. Mehata, T. C. Pant and H. B. Tripathi, *J. Phys. Chem. A*, **2004**, *108*, 2346; (*c*) A. C. Kumar and A. K. Mishra, *Talanta*, **2007**, *71*, 2003.

16. C. Reichardt, *Solvents and Solvent Effects in Organic Chemistry*, VCH, Weinheim, 2003.

17. (*a*) R. S. Butler, P. Cohn, P. Tenzel, K. A. Abboud and R. K. Castellano, *J. Am. Chem. Soc.,* **2009**, *131*, 623; (*b*) Y. Ooyama, G. Ito, K. Kushimoto, K. Komaguchi, I. Imae and Y. Harima, *Org. Biomol. Chem.*, **2010**, *8*, 2756.

18. B. Valeur, *Molecular Fluorescence*, VCH, Weinheim, 2002.

19. (*a*) C. Carmona, M. Galán, G. Angulo, M. A. Muñoz, P. Guardado and M. Balón, *Phys. Chem. Chem. Phys.*, **2000**, *2*, 5076; (*b*) C. Carmona, M. Balón, M. Galán, G. Angulo, P. Guardado and M. A. Muñoz, *J. Phys. Chem. A,* **2001**, *105*, 10334; (*c*) P.-T. Chou, Y.-

L. Liu, G.-R. Wu, M.-Y. Shia and W.-S. Yu, *J. Phys. Chem. B,* **2001**, *105*, 10674; (*d*) C. Carmona, M. Balón, A. S. Coronilla and M. A. Muñoz, *J. Phys. Chem. A,* **2004**, *108*, 1910.

20. (*a*) J. Hidalgo, A. Sánchez-Coronilla, M. Balón, M. A. Muñoz and C. Carmona, *Photochem. Photobiol. Sci*., **2009**, *8*, 414; (*b*) A. S. Coronilla, C. Carmona, M. A. Muñoz and M. Balón, *J. Fluores*., **2009**, *19*, 1025; (*c*) A. S. Coronilla, C. Carmona, M. A. Muñoz and M. Balón, *J. Fluores*., **2010**, *20*, 163; (*d*) M. M. Gonzalez, M. Vignoni, M. Pellon-Maison, M. A. Ales-Gandolfo, M. R. Gonzalez-Baro, R. Erra-Balsells, B. Epe and F. M. Cabrerizo, *Org. Biomol. Chem*., **2013**, *10*, 1807; (*e*) M. Vignoni, F. A. O. Rasse-Suriani, K. Butzbach, R. Erra-Balsells, B. Epe and F. M. Cabrerizo, *Org. Biomol. Chem*., **2013**, *11*, 5300; (*f*) M. M. Gonzalez, M. P. Denofrio, F. S. G. Einschlag, C. A. Franca, R. P. Diez, R. Erra-Balsells and F. M. Cabrerizo, *Phys. Chem. Chem. Phys*., **2014**, *16*, 16547; (*g*) C. Domonkos, F. Zsila, I. Fitos, J. Visy, R. Kassai, B. Bálint and A. Kotschy, *RSC. Adv*., **2015**, *5*, 53809; (*h*) F. A. O. Rasse-Suriani, M. P. Denofrio, J. G. Yañuk, M. M. Gonzales, E. Wolcan, M. Seifermann, R. Erra-Balsells and F. M. Cabrerizo, *Phys. Chem. Chem. Phys*., **2016**, *18*, 886.

21. (*a*) T. J. Hagen, P. Skolnick and J. M. Cook, *J. Med. Chem*., **1987**, *30*, 750; (*b*) M. Muñoz, M. Balón, J. Hidalgo, C. Carmona, R. R. Pappalardo and E. S. Marcos, *J. Chem. Soc. Perkin Trans. 2,* **1991**, 1729; (*c*) M. Balón, J. Hidalgo, P. Guardado, M. A. Muñoz and C. Carmona, *J. Chem. Soc. Perkin Trans. 2,* **1993**, 99; (*d*) R. Ikeda, T. Kimura, T. Tsutsumi, S. Tamura, N. Sakai and T. Konakahara, *Bioorg. Med. Chem. Lett.,* **2012**, *22*, 3506; (*e*) N. A. Lunagariya, V. M. Gohil, V. Kushwah, S. Neelagiri, S. Jain, S. Singh and K. K. Bhutani, *Bioorg. Med. Chem. Lett.,* **2016**, *26*, 789.

Summary

In summary, the author studied the synthesis and investigation of the photophysical and electrochemical properties for the azin- and azinium-based functional dyes. The study of the structural isomers of pyrazine-based D-π-A-π-D dyes (**2,5-PD** and **2,6-PD**) demonstrated that the introduction of D-π component on the 2,5-position of the pyrazine ring as an electron-accepting unit leads to bathochromic-shift in photoabsorption and fluorescence spectra due to the stabilization of the LUMO energy level. On the other hand, introduction of the D-π component on the 2,6-position of the pyrazine ring leads to the expression of the strong solvatofluorochromic properties because of the large $\Delta\mu$ value of the dye (Chapter 1). The 2,6-substituted pyrazine dye can effectively convert into pyrazinium dye by treating of the pyrazine dye with *n*-butyl bromide or iodide (**PD-Br** and **PD-I**). **PD-Br** and **PD-I** possess the ability for $^1O_2$ generation upon visible light irradiation, and the efficiency for the $^1O_2$ generation of **PD-I** is higher than that of **PD-Br** due to the superior heavy atom effect of the I^- as a counter anion (Chapter 2). The pyridine-substituted cyclic porphyrin dimer **CPD** and its inclusion complex **C_{60}⊂CPD** also possess the $^1O_2$ generation ability under visible light irradiation, and the ability for $^1O_2$ generation of **C_{60}⊂CPD** is lower than that of **CPD**. The lower ability for $^1O_2$ generation of **C_{60}⊂CPD** would be attributed to formation of charge-separated state **$C_{60}^{\bullet -}$-CPD$^{\bullet +}$**, leading to low intersystem crossing (ISC) efficiency for the formation of triplet excited state ^{3}(**CPD**) (Chapter 3). In Chapter 4, synthesis and investigation of the photophysical and electrochemical properties of julolidine-structured pyrido[3,4-*b*] indole dye (**ET-1**) were described. **ET-1** showed positive fluorescence solvatochromism, and the specific bathochromic shift of the fluorescence band was observed in the protic solvents such as ethanol and methanol. In addition, **ET-1** can form the 1 : 1 Py(N)-B

complex with BF_3 as a Lewis acid and a Py(N)‑H complex with CF_3COOH as a Brønsted acid, which exhibit photoabsorption and fluorescence bands at a longer wavelength region than the pristine **ET-1**. Thus, it was found that possesses the ability to act as a colorimetric and fluorescent sensor for Brønsted and Lewis acids. In Chapter 5, β-carboline-boron trifluoride complexes were prepared as a colorimetric and fluorescence sensor for water in acetonitrile. It was found that the complexes can detects water in the solvent by changing its photoabsorption and fluorescence properties based on change in the ICT characteristics through the dissociation of the complex, formation of the hydrogen-bonded complex and formation of the hydrogen-bonded PTC in low, moderate and high water content region, respectively. Thus, ICT-type sensors based on pyridine-boron trifluoride complex are promising candidates for colorimetric and fluorescence sensor for water over wide range from low to high water content region.

As described in this thesis, the author demonstrated the synthetic route and properties of the azine- and azinium-based functional dyes. In addition, it was found that some of the azine dyes express specific photophysical properties such as $^1O_2$ generation under visible light irradiation. Moreover, it was found that the azine-based complexes with BF_3 can act as the colorimetric and fluorescence sensors for water over wide range from low to high water content region.

List of Publications

Chapter 1. Synthesis and Photophysical and Electrochemical Properties of Structural Isomers of Pyrazine-Based D-π-A-π-D Fluorescent Dyes

T. Enoki, J. Ohshita and Y. Ooyama, *Bull. Chem. Soc. Jpn.*, **2018**, 91, 1704-1709.

Chapter 2. Development of a D-π-A pyrazinium photosensitizer possessing singlet oxygen generation

Y. Ooyama, T. Enoki and J. Ohshita, *RSC Adv.*, **2016**, 6, 5428-5435.

Chapter 3. Singlet oxygen generation properties of an inclusion complex of cyclic free-base porphyrin dimer and fullerene C_{60}

Y. Ooyama, T. Enoki, J. Ohshita, T. Kamimura, S. Ozako, T. Koide and F. Tani, *RSC Adv.*, **2017**, 7, 18690-18695.

Chapter 4. Synthesis and optical and electrochemical properties of julolidine-structured pyrido[3,4-*b*]indole dye

T. Enoki, K. Matsuo, J. Ohshita and Y. Ooyama, *Phys. Chem. Chem. Phys.*, **2017**, 19, 3565-3574.

Chapter 5-1. Colorimetric and ratiometric fluorescence sensing of water based on 9-methyl pyrido[3,4-*b*]indole-boron trifluoride complex

T. Enoki, Y. Ooyama, *Dalton Trans*., **2019**, DOI: 10.1039/C8DT04527E, in press.

Chapter 5-2. Development of the julolidine-structured pyrido[3,4-*b*]indole-boron trifluoride complex as a intramolecular charge transfer-type colorimetric and fluorescence sensor for water

T. Enoki, Y. Ooyama, to be submitted

Other publications not included in this thesis

1. A colorimetric and fluorescent sensor for water in acetonitrile based on intramolecular charge transfer: D-(π-A)$_2$-type pyridine-boron trifluoride complex

S. Tsumura, T. Enoki and Y. Ooyama, *Chem. Commun*., **2018**, 54, 10144-10147.

2. Tetraphenylethene- and diphenyldibenzofulvene-anthracene-based fluorescence sensors possessing photo-induced electron transfer and aggregation-induced emission enhancement characteristics for detection of water

Y. Ooyama, R. Sagisaka, T. Enoki, N. Tsunoji and J. Ohshita, *New J. Chem.*, **2018**, 42, 13339-13350.

3. Optical and Photosensitizing Properties of Spiro(dipyridinogermole)(dithienogermole)s with Eletron-Donating Amino and Electron-Withdrawing Pyridinothiadiazole Substituents

J. Ohshita, Y. Hayashi, Y. Adachi, T. Enoki, K. Yamaji, and Y. Ooyama, *ChemistrySelect*. **2018**, 3, 8604-8609.

4. Mitochondria-Targeting Polyamine-Protoporphyrin Conjugates for Photodynamic Therapy

F. Taba, A. Onoda, U. Hasegawa, T. Enoki, Y. Ooyama, J. Ohshita and T. Hayashi, *ChemMedChem*, **2018**, 13, 15-19.

5. Preparation of branched molecules by regioselective hydrosilation of tetrakis(ethynyldimethylsilyl)silanes and some of their properties

A. Naka, A. Okamoto, M. Noguchi, T. Enoki, J. Ohshita, Y. Ooyama and M. Ishikawa, *J. Organomet. Chem.*, **2017**, 846, 360-366.

6. Development of a Dual-Fluorescence Emission Sensor Based on Photo-Induced Electron Transfer and Aggregation-Induced Emission Enhancement for Detection of Water

Y. Ooyama, R. Nomura, T. Enoki, R. Sagisaka, N. Tsunoji, and J. Ohshita, *ChemistrySelect*, **2017**, 2, 7765- 7770.

7. Aggregation-induced emission (AIE) characteristic of water-soluble tetraphenylethene (TPE) bearing four sulfonate salts

Y. Ooyama, M. Sugino, T. Enoki, K. Yamamoto, N. Tsunoji and J. Ohshita; *New J. Chem.*, **2017**, 41, 4747-4749.

8. Synthesis and optical and electrochemical properties of a phenanthrodithiophene (fused-bibenzo[*c*]thiophene) derivative

Y. Ooyama, T. Enoki, S. Aoyama and J. Ohshita, *Org. Biomol. Chem.*, **2017**, 15, 7302-7307.

9. Synthesis, optical and electrochemical properties, and photovoltaic performance of a panchromatic and near-infrared $(D)_2$-π-A type BODIPY dye with pyridyl group or cyanoacrylic acid

Y. Ooyama, M. Kanda, T. Enoki, Y. Adachi and J. Ohshita, *RSC Adv.*, **2017**, 7, 13072-13081.

10. Single oxygen generation sensitized by spiro(dipyridinogermole)(dithienogermole)s

J. Ohshita, Y. Hayashi, K. Murakami, T. Enoki and Y. Ooyama, *Dalton Trans.*, **2016**, 45, 15679-15683.

11. Development of type-I/type-II hybrid dye sensitizer with both pyridyl group and catechol unit as anchoring group for type-I/type-II dye-sensitized solar cell

Y. Ooyama, K. Furue, T. Enoki, M. Kanda, Y. Adachi and J. Ohshita, *Phys. Chem. Chem. Phys.*, **2016**, 18, 30662-30676.

12. A BODIPY sensor for water based on a photo-induced electron transfer method with fluorescence enhancement and attenuation systems

Y. Ooyama, M. Hato, T. Enoki, S. Aoyama, K. Furue, N. Tsunoji and J. Ohshita, *New J. Chem.*, **2016**, 40, 7278-7281.

13. Development of D-π-A dye with (pyridiniumyl)alkanesulfonate as electron-withdrawing anchoring group for dye-sensitized solar cell

Y. Ooyama, T. Sato, T. Enoki and J. Ohshita, *Dyes Pigm.*, **2015**, 123, 349-354.

14. Preparation of imidazolium-type ionic liquids containing silsesquioxane frameworks and their thermal and ion-conductive properties

T. Ishii, T. Enoki, T. Mizumo, J. Ohshita and Y. Kaneko, *RSC Adv.*, **2015**, 5, 15226-15232.

Acknowledgements

This thesis is a summary of my studies from 2014 to 2019 under the direction of Professor Yousuke Ooyama at Hiroshima University.

I would like to express the deepest appreciation to Professor Yousuke Ooyama for his enthusiastic direction and careful suggestion. I am also grateful to Professor Joji Ohshita who provide the great research environment and give the helpful and careful advises. Furthermore, I would like to express my gratitude to Associated Professor Fumit Tani at Kyushu University who provide the porphyrin dyes in Chapter 3.

Also, I would like to say thank you to Assoc. prof. Ichiro Imae, Assoc. prof. Kenji Komaguchi, Dr. Kazuki Yamamoto, Dr. Makoto Nakashima, Dr. Kazuya Murakami, Mr. Koji Uenaka, Mr. Takafumi Sato, Mr. Kazuaki Yamamoto, Ms. Haruna Muragishi, Dr. Yohei Adachi, Dr. Masashi Nakamura, Mr. Kensuke Furue, Mr. Keishi Matsuo, Mr. Toshiyuki Tsuchida, Ms. Sayako Koge, Mr. Satoshi Aoyama, Mr. Masahiro Kanda, Mr. Junki Hara, Mr. Sota Nishimura, Keiichi Taniguchi, Ms. Haruna Kadowaki, Mr. Yuki Tanaka, Mr. Takashi Kai, Mr. Rizumu Sagisaka, Mr. Yuya Hayashi, Mr. Yuki Tomiyama, Ms. Marin Hato, Mr. Michitaka Sugino, Mr. Kosuke Yamaji, Mr. Taishi Nabeya, Mr. Kenta Shigeoka, Mr. Kenji Sasahara, Mr. Hiroki Takemoto, Mr. Hiroki Kataoka, Mr. Koki Hashiguchi, Mr. Daiki Fujimoto, Mr. Shun Matsuura, Mr. Masataka Yasui, Mr. Kohei Yukinaga, Mr. Masakuni Yamaguchi, Mr. Takahiro Manda, Mr. Kensei Tanaka, Mr. Daisuke Jimbo, Mr. Shuhei Tsumura, Mr. Toru Takaki, Mr. Tsuyoshi Wakita, Mr. Takuya Yamashita, Ms. Jeong Dayeon, Mr. Kotarou Obayashi, Mr. Kosuke Hashimoto, Mr. Yuta Mise, Mr. Nao Ueki, Ms. Haruka Yamane and Ms. Ayane Sasaki for their kindness and collaborations.